Stockholm
University

Topology Meets Frustration

Exact Solutions for Topological Surface States on Geometrically Frustrated Lattices

Licentiate Thesis in Theoretical Physics

Flore Kiki Kunst

Akademisk avhandling för avläggande av licentiatexamen vid Stockholms universitet, Fysikum

December 12, 2017

Abstract

One of the main features of topological phases is the presence of robust boundary states that are protected by a topological invariant. Famous examples of such states are the chiral edge states of a Chern insulator, the helical edge states of a two-dimensional $\mathbb{Z}_2$ insulator, and the Fermi arcs of Weyl semimetals. Despite their omnipresence, these topological boundary states can typically only be theoretically investigated through numerical studies due to the lack of analytical solutions for their wave functions. In the rare cases that wave-function solutions are available, they only exist for simple fine-tuned systems or for semi-infinite systems. Exact solutions are, however, common in the field of flat bands physics, where they lead to an understanding of the bulk bands rather than the boundary physics. It is well known that fully-periodic lattices with a frustrated geometry host localized modes that have a constant energy throughout the Brillouin zone. These localized modes appear due to a mechanism referred to as destructive interference, which leads to the disappearance of the wave-function amplitude on certain lattice sites. Making use of this mechanism, it is shown in this licentiate thesis that exact wave-function solutions can also be found on d-dimensional geometrically frustrated lattices that feature $(d-1)$-dimensional boundaries. These exact solutions localize to the boundaries when the frustrated lattice hosts a topological phase and correspond to the robust, topological boundary states.

This licentiate thesis revolves around the publication, which describes the method to finding these exact, analytical solutions for the topological boundary states on geometrically frustrated lattices, which was authored by the author of this licentiate thesis together with Maximilian Trescher and Emil J. Bergholtz and published in Physical Review B on August 30, 2017 with the title *Anatomy of topological surface states: Exact solutions from destructive interference on frustrated lattices* [1]. An introduction is given on topological phases in condensed matter systems focussing on those models of which explicit examples are given in the paper: two-dimensional Chern insulators and three-dimensional Weyl semimetals. Moreover, by making use of the kagome lattice as an example the appearance of localized and semi-localized modes on geometrically frustrated lattices is elaborated upon. The chapters in this licentiate thesis thus endeavor to provide the reader with the proper background to comfortably read, understand, place into context and judge the relevance of the work in the accompanying publication. The licentiate thesis finishes with an outlook where it is discussed that the method presented in the paper can be generalized to an even larger class of lattices and can also be applied to find exact solutions for higher-order topological phases such as corner and hinge states.

Contents

1 Introduction **7**

2 Topological Systems **11**
- 2.1 Topology and Condensed Matter Physics 11
- 2.2 Gapped Topological Phases 12
  - 2.2.1 Integer Quantum Hall Effect 12
  - 2.2.2 Quantum Hall Effect Without a Magnetic Field 13
- 2.3 Gapless Topological Systems 18
  - 2.3.1 Dirac Theory 18
  - 2.3.2 Weyl Semimetal 19
- 2.4 Boundary States 21

3 Geometrical Frustration and Flat Bands **23**
- 3.1 Kagome Lattice 23
- 3.2 Localized Modes on Kagome Lattice with Boundaries 25
- 3.3 Semi-Localized Modes on Kagome Lattice with Boundaries 26
- 3.4 Generalized Hoppings on Kagome Lattice with Boundaries 27

4 Summary of Accompanying Paper **31**
- 4.1 General Framework 31
- 4.2 Topological Boundary States 33

5 Outlook **35**

Chapter 1

Introduction

Topology in the context of condensed matter physics entered the stage in 1980 with the experimental discovery of the integer quantum Hall effect [2], and has come to the center of attention over the last decade after the theoretical proposal of the quantum-spin-Hall phase in graphene in 2005 [3, 4]. One of the main attractions of topological phases of matter is the appearance of robust, boundary states, which are characterized by a topological bulk invariant. These types of phases occur in systems with gapped and gapless bulk spectra referred to as topological insulators and topological semimetals, respectively. Prominent examples in the first category are Chern [5–7] and $\mathbb{Z}_2$ insulators [3, 4, 8–10], where the first is a two-dimensional realization of the integer quantum Hall effect and features chiral edge states quantified by the value of the bulk topological invariant, the Chern number [11], and the latter consists of two time-reversed, Chern-insulator copies realizing the quantum spin Hall effect on a lattice and features helical edge states. Other types of topological insulators were also proposed, such as the prediction and observation of three-dimensional topological insulators in $\mathrm{Bi}_{1-x}\mathrm{Sb}_x$ [12–17], where the surface states are two-dimensional Dirac nodes, which are protected by time-reversal symmetry. The role of symmetries was further investigated and led to many classification schemes [18, 19], as well as the proposal and experimental observation of, amongst others, topological crystalline insulators [20–23], where the topological boundary states are protected by the crystalline symmetry of the lattice. Weyl semimetals are the prototypical example of a gapless topological phase in three dimensions, and were first theoretically predicted [24–27] before being experimentally observed in 2015 [28–30]. The low-energy approximation of the gap closing is described by the Weyl equation [31], and has a Chern number associated with it. The surface states of Weyl semimetals are open Fermi arcs living on opposite surfaces, which are connected via the Weyl nodes in the bulk and are remnants of the chiral, edge states of Chern insulators.

Despite the differences in bulk dispersion, the hallmark of all single-particle, topological systems is the appearance of robust, boundary states. Nevertheless, solutions for their wave functions have only been found in a number of cases relying either on approximations and fine-tuning [32–40] or the less-restrictive transfer matrix method [41–43]. Besides these efforts, boundary states have only been studied in a numerical context, and no analytical solutions are known, which exist independent of Hamiltonian details, in the entire surface Brillouin zone, at finite size, and can be generalized to any dimension. This absence of generic solutions for one of the most relevant features of topological phases provided a strong motivation to develop a general formalism for finding exact boundary-state solutions that are valid both in a topologically trivial and non-trivial regime, and go beyond any of the aforementioned approximations. By considering a large class of d-dimensional, geometrically frustrated lattices that consist of an alternating stacking of two different $(d-1)$-dimensional lattices, referred to as A and B lattices, and terminates with A lattices on either side, exact solutions are straightforwardly retrieved by making explicit use of the underlying lattice structure. The resulting formalism is presented in this licentiate thesis, which revolves around the work in the accompanying paper written by the author of this licentiate thesis together with Maximilian Trescher and Emil J. Bergholtz and was published in Physical Review B on August 30, 2017 with the title *Anatomy of topological surface states: Exact solutions from destructive interference on frustrated lattices* [1], and makes use of techniques from the fields of magnetism and flat-band physics where the search for exact solutions on geometrically frustrated lattices has been ongoing for several decades.

Geometrically frustrated lattices are typically studied in the context of magnetism due to the strong suspicion that they host spin-liquid phases [44]. Even though competing ground states on these types of lattices render them extremely complicated to study, it turns out that frustration greatly simplifies the retrieval of analytical wave-function solutions for topological boundary states because it yields disappearing wave-function amplitudes on the B lattices. This leads to exact solutions of the following form

$$|\Psi(\mathbf{k})\rangle = \mathcal{N}(\mathbf{k}) \bigoplus_{m=1}^{N} (r(\mathbf{k}))^m \, |\Phi(\mathbf{k})\rangle_m \, , \tag{1.1}$$

which only depend on the eigenfunctions of the A-lattice Hamiltonian $|\Phi(\mathbf{k})\rangle$ and the connectivity between the A and B lattices explicitly included in the function $r(\mathbf{k})$ where $\mathbf{k}$ is the $(d-1)$-dimensional quasi momentum parallel to the system boundaries, m labels the A lattices and a total of N of such lattices are stacked. The specific form of $r(\mathbf{k})$ is derived assuming the vanishing amplitudes on the B lattices, which together with the geometrical frustration amounts to a local constraint. This constraint is fulfilled by Eq. (1.1) but not by the other eigenstates in the system, and is essential to the retrieval of the wave-function solution. Frustration thus surprisingly aids instead of complicates the recovery of exact solutions. From the form of the solution it follows that the wave function localizes to either of the lattice boundaries when $|r(\mathbf{k})| \neq 1$ and is delocalized when $|r(\mathbf{k})| = 1$. The eigenvalues associated with this solution are simply the eigenvalues of the A-lattice Hamiltonian. This means that finding an analytical solution for Eq. (1.1) and its associated eigenvalue is a tractable problem because the exact form derives from solving the A-lattice Hamiltonian instead of the full Hamiltonian of the system. Moreover, the localization of the mode is fully controlled by adjusting the hopping parameters that govern the connectivity between the A and the B lattices and are explicitly included in the function $r(\mathbf{k})$. Combining this with the fact that one has full access to the surface dispersion, i.e. the eigenvalues of the A Hamiltonian, it is possible to engineer any desired topological phase. To showcase this formalism, explicit examples of Chern insulators, Weyl semimetals as well as topologically-trivial systems are discussed in the accompanying paper.

The technique used to find the generic wave-function solutions in Eq. (1.1) was inspired by the construction of flat bands in fully-periodic frustrated lattices. On these lattices, destructive interference leads to the vanishing of wave-function amplitudes on certain lattice sites by which a mode is trapped such that is localizes exactly. The existence of these modes is highly sensitive to fine tuning of the Hamiltonian, which is usually restricted to include real nearest-neighbor hopping terms only. The academic interest in flat bands originates from the fact that they provide the perfect platform to study interactions and strongly-correlated phases. In the early nineties, it was shown that both ferromagnetic Hubbard models on line graphs [45–47], where a line graph of a lattice is defined as the connection of the edges of adjacent vertices of the latter, e.g. a kagome lattice is the line graph of a honeycomb lattice, and antiferromagnetic Heisenberg models on frustrated lattices [48, 49] have a ground state that is formed by a flat band, where the band corresponds to localized magnons for the latter [50, 51]. These two models are related through a mapping onto a classical hard-core problem [52, 53], and the growing body of theoretical [54–58] and experimental [59, 60] contributions highlight the ongoing activity in the field. The developed formalism resulting in Eq. (1.1) thus successfully merges two of the major research fields in condensed matter, frustrated physics and topology.

This licentiate thesis aims at providing the reader with the necessary background on topological systems and localized modes on frustrated lattices to be able to understand, and properly assess the novelty and significance of the research presented in the accompanying paper. To that end, ch. 2 provides an introduction into topological systems focussing on Chern insulators and Weyl semimetals in particular, but also mentioning $\mathbb{Z}_2$ insulators and Dirac semimetals. In the subsequent chapter, the occurrence of localized modes in frustrated lattices is explained in more detail on both fully periodic and non-periodic systems by making use of the kagome lattice as an example. Ch. 4 provides an introduction into the accompanying paper by summarizing its contents and main results. Lastly, new directions and applications of the presented work are discussed in the outlook in ch. 5.

Chapter 2

Topological Systems

This chapter provides an introduction into topological systems, and starts by addressing the meaning of topology in physics, especially in the context of condensed matter, and then continues by introducing topological models with a gapped and gapless bulk spectrum in sections 2.2 and 2.3, respectively. In section 2.4, the importance of the boundary states in these single-particle, topological models is elaborated upon in two contexts. Firstly, it is emphasized that they provide experimental evidence for the identification of topological systems. Secondly, the advantages of having a theoretical understanding of these states is being addressed. By reviewing the previous theoretical effort towards finding a solution for these states and revealing the limits of this research, a strong argument is provided for the relevance of the work presented in the accompanying paper. This chapter provides the reader with the necessary information to comprehend the accompanying paper and is by no means exhaustive on the topic of topological matter. For more details on the topics that are discussed, the reader is directed to several review papers [61–65], which were of great help to the author.

2.1 Topology and Condensed Matter Physics

In mathematics, topology is the study of the shape of geometrical objects. These objects are topologically equivalent if they are related via continuous transformations, such as stretching, crumpling and bending. The topology of an orientable object for example is often quantified by the total number of its holes, called genera, and can only change under some violent transformation, such as tearing, gluing or cutting. By this definition, the famous example of the topological equivalence of a cup with an ear and a donut is straightforwardly understood because they both have genus one, which means they can be continuously deformed into each other.

In condensed matter physics, topology is related to the existence of topological phases in quantum systems in a similar fashion, and is treated in the scope of topological band theory [65,66]. The phases are described by a topological invariant, which characterizes the boundary physics and is extrapolated from the bulk of the material. Topological invariants can only change under extreme transformation, and are thus insensitive to small perturbations. As such, they are extremely robust and provide a reliable way to quantify the topological phase of a material. Quantum systems are said to be topologically equivalent if they have the same topological invariant, or, alternatively, topological equivalence dictates that the Hamiltonians associated with these quantum systems can be transformed into each other by making use of continuous transformations only. Concretely, this means that if one takes two bulk-insulating systems, they are topologically equivalent if they can be deformed into each other without closing the gap in the bulk spectrum, which ensures that the topological invariant does not change. In the following sections, several examples of different topological phases are discussed by way of introducing examples.

2.2 Gapped Topological Phases

This section focusses on topological phases in quantum systems that feature a gapped bulk spectrum by first introducing the aforementioned integer quantum Hall effect in greater detail, which is followed by examples of lattice realizations thereof. The importance of the fundamental physics presented in this section is emphasized by the high density of Nobel Prizes that have been awarded to scientists in the field. Klaus von Klitzing won the Nobel Prize in Physics in 1985 for his discovery of the integer quantum Hall effect [67], Robert Laughlin, Horst Strömer and Daniel Tsui received the Nobel Prize in Physics in 1998 for discovering and explaining the fractional quantum Hall effect [68], and last year David Thouless, Michael Kosterlitz and Duncan Haldane were awarded the Nobel Prize in Physics in 2016 "for theoretical discoveries of topological phase transitions and topological phases of matter" [69].

2.2.1 Integer Quantum Hall Effect

The importance of topology in condensed matter physics was recognized three decades ago with the theoretical investigation of the integer quantum Hall effect [2]. Upon applying a strong, perpendicular magnetic field, $B = 18\text{T}$, to a two-dimensional electron gas at low temperatures, $T = 1.5\text{K}$, and probing this set-up with a weak, longitudinal electrical current, $I = 10^{-6}\text{A}$, where the stated values correspond to the ones used by von Klitzing in his experiment, one finds that the Hall conductivity σ_{xy} quantizes to extremely good precision

$$\sigma_{xy} = \nu \frac{e^2}{h}, \qquad \nu \in \mathbb{Z}, \tag{2.1}$$

with h the Planck constant, e the electron charge and ν the number of filled Landau levels, $E_\nu = \hbar\omega_c(\nu + 1/2)$ with ω_c the cyclotron frequency, which form the energy bands of an electron confined to a two-dimensional space exposed to a perpendicular magnetic field. The physics of this system can be understood in a single-particle picture due to the Landau levels being completely filled or empty as dictated by the strictly integer value of ν. The exact quantization is related to the appearance of gapless, chiral states on the edges, while the bulk spectrum simultaneously features a gap. These concurrent properties can be understood from the nature of the Landau levels. In the bulk, the system is gapped and the Fermi energy is chosen such that ν Landau levels are filled. By mimicking the edges of the system with a potential wall, the Landau levels are deformed such that they curve up and ν levels cross the Fermi energy leading to the appearance of ν gapless, chiral modes localized to the edges.

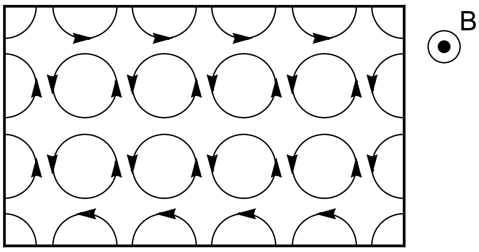

Figure 2.1: Schematic figure of the semiclassical picture of the integer quantum Hall effect. Upon the application of a strong, perpendicular magnetic field, it can be shown that the electrons acquire a circular motion whose direction is dictated by the direction of the magnetic field, and the frequency with which the electron go around the circle is set by the cyclotron frequency $\omega_c = eB/m$ with m the electron mass. The electrons are locked in their orbits, which results in insulating behavior in the bulk and the appearance of skipping orbits on the edges. The direction of the resulting skipping motion is set by the magnetic field, and the edge electrons are thus chiral.

This simplistic picture does not explain the robustness of the quantization of the Hall conductivity. ν is expressed in terms of the magnetic field as $\nu = nh/(eB)$ with n the electron density, derived from Drude's model where $\sigma_{xy} = ne/B$, which suggests that σ_{xy} behaves non-analytically with B. However, in reality the Hall conductivity forms plateaux while varying the applied magnetic field. In a semiclassical picture, this is can be understood from the bulk and edge behavior, which is schematically shown in Fig. 2.1. Varying the magnetic field results in a change in the number of available states in the system because one electronic state can exist per quantum flux $\phi_0 = h/e$ in each Landau level (see e.g. Ref. [70]). Only the edge states contribute to the conductivity such that the latter forms plateaux when the number of electrons in the bulk states changes while leaving the edge states untouched. Interestingly, in the presence of stronger disorder the plateaux become larger, whereas they completely disappear in the limit of vanishing disorder. Indeed, a key role is played by disorder which leads to the natural occurrence of localized and extended states [71–75]. Disorder smears out the Landau levels, where the perturbation away from the original Landau levels is formed by the localized states in the bulk, such that instead of an actual energy gap the system now has a so-called mobility gap. Through the mapping of the problem onto a cylinder, Laughlin showed by making use of gauge invariance that as long as the Fermi energy lies inside the mobility gap, the Hall conductivity is insensitive to edge effects and is quantized [73]. A more quantitative result was provided by Thouless, Kohmoto, Nightingale and Den Nijs (TKNN) [76], who showed that the Hall conductivity is a topological invariant. When the Fermi energy lies inside the mobility gap, linear-response theory is used to find the Kubo formula for the Hall conductivity of the integer quantum Hall system on a torus, where the integer ν is known as the TKNN invariant,

$$\sigma_{xy} = \frac{ie^2}{A\hbar} \sum_{E_\alpha < E_F} \sum_{E_\beta > E_F} \frac{\langle\phi_\alpha| \frac{\partial H}{\partial k_x} |\phi_\beta\rangle \langle\phi_\beta| \frac{\partial H}{\partial k_y} |\phi_\alpha\rangle - \langle\phi_\alpha| \frac{\partial H}{\partial k_y} |\phi_\beta\rangle \langle\phi_\beta| \frac{\partial H}{\partial k_x} |\phi_\alpha\rangle}{(E_\alpha - E_\beta)^2} = \frac{\nu e^2}{h}, \tag{2.2}$$

where A is the area of the sample, H the Hamiltonian in momentum space, ϕ_α the eigenfunctions, and E_α the eigenstates [76]. TKNN showed that this equation indeed leads to a quantization of the Hall conductance both in the presence of a weak and strong periodic potential. Therefore, the occurrence of the integer quantum Hall effect relies on the TKNN invariant being non-zero, which does not necessarily require the presence of a magnetic field, and in the next section such a case is explored.

2.2.2 Quantum Hall Effect Without a Magnetic Field

The beauty of the physics displayed by the integer quantum Hall effect juxtaposed with the experimental difficulty to observe it — one needs extremely clean samples, extremely strong magnetic fields, and do the experiment at extremely low temperatures — led Duncan Haldane to propose a theoretical model in which the integer quantum Hall effect is realized on the honeycomb lattice [5]. Instead of applying an actual magnetic field, the presence of a zero-average magnetic field is mimicked through the inclusion of time-reversal-symmetry breaking, complex next-nearest-neighbor hopping terms in the tight-binding Hamiltonian. The real-space Hamiltonian with one orbital per site reads

$$H = t_1 \sum_{\langle i,j\rangle} \left(\phi^\dagger_{A,i}\phi_{B,j} + h.c.\right) + t_2 \sum_{\langle\langle i,j\rangle\rangle} \mathrm{e}^{i\phi_{ij}} \left(\phi^\dagger_{A,i}\phi_{A,j} + \phi^\dagger_{B,i}\phi_{B,j}\right) + V \sum_{i} \left(\phi^\dagger_{A,i}\phi_{A,i} - \phi^\dagger_{B,i}\phi_{B,i}\right), \tag{2.3}$$

where $\phi_{A,i}$ ($\phi^\dagger_{A,i}$) annihilates (creates) an electron on sublattice A at site i, t_1 (t_2) is the (next-)nearest-neighbor hopping parameter, V is a staggering potential and the phase $\phi_{ij} = (-)\phi$ if the next-nearest-neighbor hopping is (anti-)clockwise as shown in Fig. 5. The sum in the first term runs over all the nearest-neighbor sites $\langle i, j\rangle$, and the second sum over all the next-nearest-neighbor sites $\langle\langle i, j\rangle\rangle$. The momentum-space Hamiltonian is retrieved by performing a Fourier transform,

$$\phi_{A,i} = \frac{1}{\sqrt{N_A}} \sum_{\mathbf{k}} \mathrm{e}^{i\mathbf{k}\cdot\mathbf{r}_i} \phi_{A,\mathbf{k}}, \tag{2.4}$$

where N_A is the total number of A sublattice sites in the system and $\mathbf{r}_i$ are the spatial vectors with $\mathbf{a}_i$ the lattice vectors $\mathbf{a}_1 = \boldsymbol{\delta}_1 - \boldsymbol{\delta}_3$, $\mathbf{a}_2 = \boldsymbol{\delta}_3 - \boldsymbol{\delta}_2$ and $\mathbf{a}_3 = \boldsymbol{\delta}_2 - \boldsymbol{\delta}_1$, and $\boldsymbol{\delta}_i$ the nearest-neighbor vectors $\boldsymbol{\delta}_1 = (1, \sqrt{3})/2$, $\boldsymbol{\delta}_2 = (1, -\sqrt{3})/2$, $\boldsymbol{\delta}_3 = -(1, 0)$ with the lattice constant $a = 1$, and reads

$$H = \sum_{\mathbf{k}} \Phi^\dagger_{\mathbf{k}} \mathcal{H}_{\mathbf{k}} \Phi_{\mathbf{k}}, \qquad \mathcal{H}_{\mathbf{k}} = \mathbf{d}(\mathbf{k}) \cdot \boldsymbol{\sigma} + d_0(\mathbf{k})\sigma_0, \tag{2.5}$$

where $\Phi^\dagger_{\mathbf{k}}$ is a spinor with pseudo-spin degree of freedom, $\boldsymbol{\sigma}$ are the Pauli matrices

$$\sigma_x = \sigma_1 = \begin{pmatrix} 0 & 1 \\ 1 & 0 \end{pmatrix}, \qquad \sigma_y = \sigma_2 = \begin{pmatrix} 0 & -i \\ i & 0 \end{pmatrix}, \qquad \sigma_z = \sigma_3 = \begin{pmatrix} 1 & 0 \\ 0 & -1 \end{pmatrix}, \tag{2.6}$$

acting in sublattice space, σ_0 is the (2×2) identity matrix $\mathbb{1}_2$ and

$$\begin{gathered} d_0(\mathbf{k}) = 2\,t_2 \cos(\phi) \sum_{i=1}^{3} \cos(\mathbf{k}\cdot\mathbf{a}_i), \quad d_x(\mathbf{k}) - i d_y(\mathbf{k}) = t \sum_{i=1}^{3} \mathrm{e}^{i\mathbf{k}\cdot\boldsymbol{\delta}_i}, \\ d_z(\mathbf{k}) = V - 2\,t_2 \sin(\phi) \sum_{i=1}^{3} \sin(\mathbf{k}\cdot\mathbf{a}_i). \end{gathered} \tag{2.7}$$

The eigenvalues read

$$E_\pm(\mathbf{k}) = d_0(\mathbf{k}) \pm |\mathbf{d}(\mathbf{k})|\,. \tag{2.8}$$

When there are two degrees of freedom in a system, the corresponding Hamiltonian can always be written in the Dirac form of Eq. (2.5) and such Hamiltonians will be encountered frequently in this thesis. Moreover, from now on, all Hamiltonians will be written directly in momentum space, where the corresponding real-space Hamiltonians can easily be recovered by performing an inverse Fourier transformation.

The same topological invariant as in the case of the integer quantum Hall effect can be associated with this model. Eq. (2.2) can be rewritten to read

$$\sigma_{xy} = \frac{ie^2}{2\pi h} \int_{BZ} \mathrm{d}^2k \left[\frac{\partial}{\partial k_x} \langle\phi(\mathbf{k})| \frac{\partial}{\partial k_y} |\phi(\mathbf{k})\rangle - \frac{\partial}{\partial k_y} \langle\phi(\mathbf{k})| \frac{\partial}{\partial k_x} |\phi(\mathbf{k})\rangle \right] = \frac{e^2}{h} C,$$

where $\mathbf{k}$ is the Bloch momentum, C is known as the first Chern number (see e.g. Ref. [11]) and the integration is over the Brillouin zone. The integrant is the Berry curvature

$$\mathcal{F}_{xy}(\mathbf{k}) = \frac{\partial A_y(\mathbf{k})}{\partial k_x} - \frac{\partial A_x(\mathbf{k})}{\partial k_y},$$

which can be interpreted as a magnetic field acting in momentum space with

$$A_x(\mathbf{k}) = i \langle\phi(\mathbf{k})| \frac{\partial}{\partial k_x} |\phi(\mathbf{k})\rangle\,,$$

the Berry connection, which acts as the vector potential in momentum space, and $|\phi(\mathbf{k})\rangle$ some isolated band [77]. The Chern number thus reads

$$C = \frac{1}{2\pi} \int_{BZ} \mathrm{d}^2k\, \mathcal{F}_{xy}(\mathbf{k}) \in \mathbb{Z}. \tag{2.9}$$

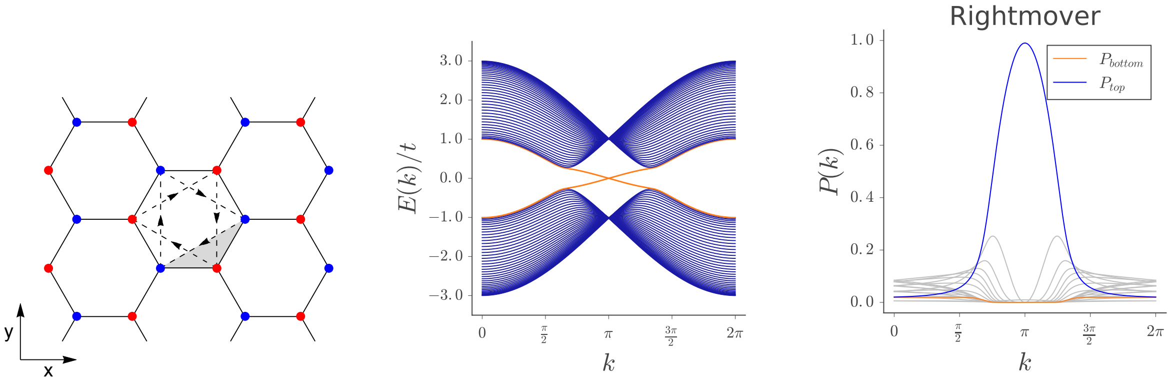

(a) (b) (c)

Figure 2.2: (a) The honeycomb lattice with two sublattices in red and blue. The dashed lines indicated the next-nearest-neighbor hopping with a positive phase when hopping along the direction of the arrows and vice versa. A flux $\phi\,[\phi_0 = h/e]$ penetrates the shaded area and the total flux through a unit cell is zero. (b) The energy spectrum of the honeycomb lattice wrapped in a cylinder with zigzag edges plotted for $N = 40$ with $|t/t_2| = 20$ and $V/t = 0$. The orange bands correspond to the edge states and the blue bands form the bulk bands. (c) The weight of the wave function of the right mover $P_m^+(k)$ is shown for $N = 10$ with the same parameters as in (b). The right mover strongly localizes to the "top", $m = 20$, of the cylinder, shown in blue, whereas it is weakly localized to the "bottom", $m = 1$, shown in orange. The weight of the wave function on the sites between the top and the bottom of the cylinder are shown in grey.

This integral always yields an integer value, which is required by the invariance of Berry's phase when measured on a closed path [77]. Note that the total Chern number of a band spectrum should always equal zero because a non-zero Chern number implies there is no way of choosing a smooth gauge [78], which is not allowed for a completely filled system. Using the Dirac form of the Hamiltonian in Eq. (2.5), the Chern number simplifies to

$$C = \frac{1}{4\pi}\int_{BZ} \mathrm{d}^2k\ \hat{\mathbf{d}}(\mathbf{k}) \cdot \left(\frac{\partial \hat{\mathbf{d}}(\mathbf{k})}{\partial k_x} \times \frac{\partial \hat{\mathbf{d}}(\mathbf{k})}{\partial k_y}\right), \tag{2.10}$$

where $\hat{\mathbf{d}}(\mathbf{k}) = \mathbf{d}(\mathbf{k})/|\mathbf{d}(\mathbf{k})|$, which maps the two-dimensional Brillouin zone to the unit sphere. Now the Chern number can be reinterpreted as the number of times $\hat{\mathbf{d}}(\mathbf{k})$ wraps the sphere, i.e. when $\hat{\mathbf{d}}(\mathbf{k})$ points outward everywhere, the Chern number $C = 1$ and when $\hat{\mathbf{d}}(\mathbf{k})$ points inward, the Chern number $C = -1$. Using this definition, one finds that the Chern numbers of the valence and conduction band of the Hamiltonian in Eqs. (2.5)-(2.7) are $C = 1$ and $C = -1$, respectively, when the parameters are for example in the region $\phi = \pi/2$, $t_2/t = 1/2$ and $|V/t| \leq 1.75$. Note that the Chern number may also be non zero for different parameter values. The finite value of the Chern number in this model can be understood from the way the degeneracy in the energy spectrum is lifted through the inclusion of the time-reversal-symmetry breaking mass term in the Hamiltonian. In the case of real nearest-neighbor hopping only, i.e. $t_2 = 0$ in Eq. (2.7), the band spectrum features Dirac points, which are touched upon in the next section, at the K and K' points in the hexagonal Brillouin zone of the honeycomb lattice. Turning on t_2, a gap is opened in these Dirac points with opposite mass at the K and K' points in the Brillouin zone such that one can show that $\hat{\mathbf{d}}(\mathbf{k})$ is ensured to point in- or outward everywhere on the unit sphere [65].

Similar to the integer quantum Hall effect, the non-zero Chern number implies the existence of non-trivial, chiral edge states, which can be studied by changing the geometry of the honeycomb lattice by wrapping it in a cylinder with zigzag edges. In such a geometry, the system is

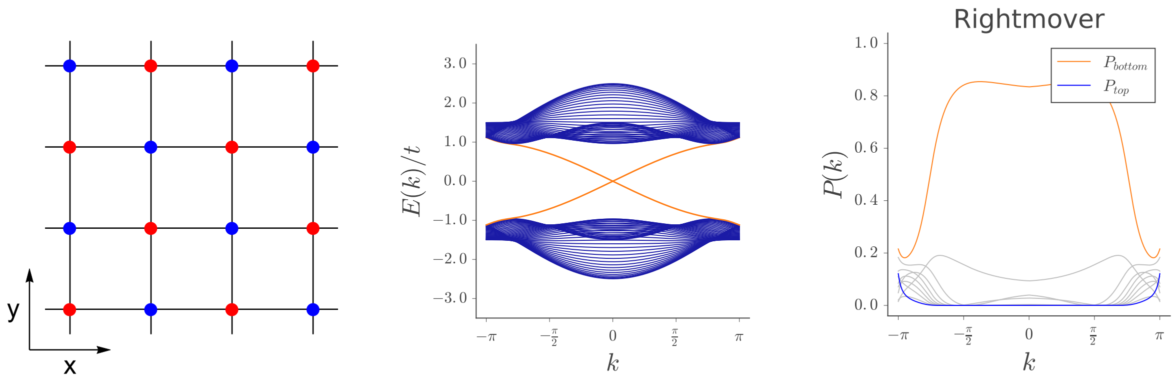

(a) (b) (c)

Figure 2.3: (a) The checkerboard lattice with two sublattices in red and blue. (b) The energy spectrum of the checkerboard model in a cylinder configuration with edges made up of a red-blue chain plotted for $N = 20$, $t_2/t = 1$ and $V/t = 0.5$. (c) The weight of the wave function of the right mover for a cylinder with $N = 10$ plotted per chain, i.e. $P^+_{2m-1}(k) + P^+_{2m}(k)$ for $m = 1, 2, ..., N$, for the same parameters as in (b). The right mover localizes to the "bottom", $N = 1$, of the cylinder, shown in orange. The localization to the "top", $N = 10$, is shown in blue and the weight of the wave function on the sites between the top and bottom of the cylinder are shown in grey.

no longer periodic in one direction and the corresponding Hamiltonian reads

$$H = \sum_k \Psi_k^\dagger \mathcal{H}_k^N \Psi_k, \qquad \mathcal{H}_k^N = \begin{pmatrix} \mathcal{H}_k & \mathcal{H}_\perp & 0 & 0 & 0 \\ \mathcal{H}_\perp^\dagger & \mathcal{H}_k & \mathcal{H}_\perp^\dagger & 0 & 0 \\ 0 & \mathcal{H}_\perp & \mathcal{H}_k & \cdots & 0 \\ 0 & 0 & \vdots & \ddots & \mathcal{H}_\perp^\dagger \\ 0 & 0 & 0 & \mathcal{H}_\perp & \mathcal{H}_k \end{pmatrix}, \tag{2.11}$$

where k is the crystal momentum parallel to the edges, N is the number of zigzag chains that are stacked to form the honeycomb lattice, Ψ_k is the annihilation operator with sublattice degree of freedom and

$$\mathcal{H}_k = 2\,t \cos\left(\frac{\sqrt{3}k}{2}\right)\sigma_x - \left[V - t_2 \sin\left(\sqrt{3}k\right)\right]\sigma_z, \quad \mathcal{H}_\perp = t_2 \sin\left(\frac{\sqrt{3}k}{2}\right)\sigma_z + t\,\sigma_-, \tag{2.12}$$

where $\sigma_\pm = (\sigma_x \pm i\,\sigma_y)/2$ and ϕ is set to $\pi/2$. The honeycomb lattice with this Hamiltonian is also used in Sect. III E of the accompanying paper. The energy spectrum is shown in Fig. 2.2(b) and features two states crossing the bulk gap, a right and a left mover. The presence of these states is a strong indication that there are indeed localized boundary states in the system, because such bands must necessarily break translational invariance, which means they must live near a boundary or other defect. However, to be certain, the weight of the associated wave functions $\psi_\pm(k)$,

$$P_{\pm,m}(k) = \langle \psi_{\pm,m}(k) | \psi_{\pm,m}(k) \rangle\,, \tag{2.13}$$

on each distinguishable site m in the cylinder with ± relating to the chirality is shown in Fig. 2.2(c). Indeed, one sees that the right mover localizes to one side of the cylinder. The weight of the left mover results in a similar plot with the localization to the opposite edge. The edge states can only disappear if the bulk gap closes, and they are thus protected by the bulk gap.

Lattices exhibiting this type of physics are known as Chern insulators. Such theoretical models can be realized on any two-dimensional lattice, such as for instance the checkerboard lattice shown in Fig. 2.3(a) with the Hamiltonian and its eigenvalues given in Eqs. (2.5) and (2.8), respectively, with N the number of red-blue chains that are stacked to form the checkerboard lattice, and

$$d_0(\mathbf{k}) = 0, \quad d_x(\mathbf{k}) = t\sin\left(\frac{k_x}{\sqrt{2}}\right), \quad d_y(\mathbf{k}) = t\sin\left(\frac{k_y}{\sqrt{2}}\right), \tag{2.14}$$

$$d_z(\mathbf{k}) = V + t_2\left[\cos\left(\frac{k_x+k_y}{\sqrt{2}}\right) + \cos\left(\frac{k_x-k_y}{\sqrt{2}}\right)\right], \tag{2.15}$$

where the lattice constant a is set to one. Computing the Chern number, one finds $C = 1$ and $C = -1$ for the valence and conduction band, respectively, when $t_2/t = 1$ and $|V/t| \leq 2$. The checkerboard lattice with this Hamiltonian is also featured in Sect. III C of the accompanying paper. The Hamiltonian for the lattice wrapped in a cylinder is given by Eq. (2.11) and

$$\mathcal{H}_k = t\sin\left(\frac{k}{2}\right)\sigma_x + V\sigma_z, \qquad \mathcal{H}_\perp = -i\frac{t}{2}\sigma_y + t_2\cos\left(\frac{k}{2}\right)\sigma_z, \tag{2.16}$$

with k the crystal momentum parallel to the edges. The corresponding energy spectrum with two states crossing the bulk gap is shown in Fig. 2.3(b). The weight of the wave function $P_m^+(k)$ associated with the right mover is shown in Fig. 2.3(c), and one can clearly see that the state localizes to one of the two edges of the cylinder.

The notion that time-reversal symmetry needs to be broken to find anything of topological interest prevailed for a long time in the community until it was realized in 2005 that the preservation of time-reversal symmetry could also lead to an interesting topological phase. Kane and Mele introduced a model in which they allow for a spin degree of freedom which is absent in Haldane's model [3]. Taking two time-reversed copies of Haldane's model in Eqs. (2.5) and (2.7) with $V = 0$ and $\phi = \pi/2$ yields $H = \sum_{\mathbf{k},s,s'} \Phi^\dagger_{\mathbf{k},s}\mathcal{H}_{\mathbf{k};s,s'}\Phi_{\mathbf{k},s'}$ where s labels the spin and

$$\mathcal{H}_{\mathbf{k};s,s'} = \left[d_x(\mathbf{k})\sigma_x + d_y(\mathbf{k})\sigma_y\right]\tau_0 + d_z(\mathbf{k})\sigma_z\tau_z,$$

with the vectors containing Pauli matrices $\boldsymbol{\sigma}$ and $\boldsymbol{\tau}$ acting in pseudo-spin and spin space, respectively. The last term is a spin-orbit coupling term, which can most obviously be seen when considering its real-space expression $\sim (\boldsymbol{\delta}_1 \times \boldsymbol{\delta}_2)\cdot\boldsymbol{\tau}$. Similar to the Haldane model, this model features edge states, which due to the presence of the spin-orbit coupling term appear in the form of time-reversal-symmetry protected, helical edge states. Their presence is defined by a $\mathbb{Z}_2$-topological invariant ν_2, which is zero if the system is in a topologically trivial phase and one if not. The $\mathbb{Z}_2$ invariant is found by using the parity eigenvalues $\xi_m(\Gamma_i) = \pm$ of the Bloch states $u_m(\Gamma_i)$ at the four time-reversal invariant points in the two-dimensional Brillouin zone Γ_i, where Kramers' theorem [79] requires the states to be doubly degenerate, such that $(-1)^{\nu_2} = \prod_{i=1}^4\prod_m \xi_m(\Gamma_i)$, where m are the occupied bands [80]. This equation requires the preservation of inversion symmetry. In case this symmetry is broken, other equations are available to compute the invariant [4]. Unfortunately, the value of the spin-orbit-coupling parameter in graphene is too small and such a phase does not exist. However, subsequently the same phase was proposed in zinc-blende semiconductors [8] and HgTe quantum wells [9], and experimentally detected in the latter [10]. Similar to Chern insulators, any two-dimensional lattice can be turned into a $\mathbb{Z}_2$ insulator, which in the simplest case just amounts to adding two time-reversed Chern-insulator copies. However, the fundamental difference between the Chern and $\mathbb{Z}_2$ insulators is that the first are protected by topology whereas the latter are protected by a symmetry in the system. By breaking time-reversal symmetry in the spin-full system, the helical edge states annihilate and gap out. With this discovery, the importance of symmetry was greatly advanced and led to the theoretical proposal and experimental discovery of three-dimensional topological insulators in $\mathrm{Bi}_{1-x}\mathrm{Sb}_x$ [12–17], where the surface states are formed by gapless, two-dimensional Dirac fermions, which are protected by time-reversal symmetry, as well as, topological crystalline insulators [20–23] where the boundary states are protected by crystal symmetries.

2.3 Gapless Topological Systems

Soon after the discovery of gapped topological systems, it was realized that systems that feature a gap closing in the bulk spectrum, can also harbor a topological phase. These gap closings are closely related to Dirac theory, which is reviewed at the start of this section. This is followed by a discussion on the condensed matter realization of Weyl fermions that follow from Dirac theory in Weyl semimetals.

2.3.1 Dirac Theory

In 1928 Paul Dirac presented the famous Dirac equation [81], which describes massive spin-1/2 particles, as to reconcile special relativity with quantum mechanics:

$$\left(i\hbar\gamma^\mu\partial_\mu - mc\right)\psi = 0, \tag{2.17}$$

where $\hbar = h/(2\pi)$, m is the mass of the particle, c is the speed of light, and γ^μ are the (4×4) gamma matrices, which generate the Clifford algebra $\{\gamma^\mu, \gamma^\nu\} = 2\eta^{\mu\nu}\mathbb{1}_4$ with $\eta^{\mu\nu} = (+, -, -, -)$ the Minkowski metric and

$$\gamma^0 = \begin{pmatrix}\sigma_0 & 0\\ 0 & -\sigma_0\end{pmatrix}, \qquad \gamma^i = \begin{pmatrix}0 & \sigma^i\\ -\sigma^i & 0\end{pmatrix},$$

with $\sigma^i = \sigma_i$ the Pauli matrices and σ_0 the (2×2) identity matrix $\mathbb{1}_2$. Particles obeying this equation are called Dirac fermions, and the corresponding Dirac Hamiltonian can be found by rewriting Eq. (2.17) in the form of the Schrödinger equation

$$i\hbar\,\partial_t\psi = \left(-\hbar c\,\gamma^0\gamma^i k_i + \gamma^0 mc^2\right)\psi,$$

where it is used that $\partial_0 = \partial_t/c$ and $-i\partial_i = k_i$, such that the Dirac Hamiltonian reads

$$H_{\text{Dirac}} = \psi^\dagger\mathcal{H}_{\text{Dirac}}\psi, \qquad \mathcal{H}_{\text{Dirac}} = -\hbar c\,\gamma^0\gamma^i k_i + \gamma^0 mc^2. \tag{2.18}$$

The Hamiltonian reveals that the dispersion relation of a Dirac fermion has a linear dependence on the momentum as opposed to the usual quadratic momentum dependence of free fermions.

A year after the introduction of the Dirac equation, Hermann Weyl proposed the existence of Weyl fermions [31], by rewriting the massless Dirac equation ($m = 0$) in the Weyl or chiral basis

$$\gamma^0 = \begin{pmatrix}0 & \sigma_0\\ \sigma_0 & 0\end{pmatrix}, \qquad \gamma^i = \begin{pmatrix}0 & \sigma^i\\ -\sigma^i & 0\end{pmatrix}.$$

In this basis the Dirac equation reduces to

$$\mathcal{H}_{\text{Dirac}} = \begin{pmatrix}\hbar c\,\sigma^i k_i & mc^2\sigma_0\\ mc^2\sigma_0 & -\hbar c\,\sigma^i k_i\end{pmatrix},$$

such that when $m = 0$ it can be projected onto two chiral subspaces $\psi = (\psi_L, \psi_R)^T$, which are defined by the following chiral projections

$$\psi_L = \frac{1-\gamma^5}{2}\psi = \begin{pmatrix}\mathbb{1}_2 & 0\\ 0 & 0\end{pmatrix}\psi, \qquad \psi_R = \frac{1+\gamma^5}{2}\psi = \begin{pmatrix}0 & 0\\ 0 & \mathbb{1}_2\end{pmatrix}\psi,$$

where

$$\gamma^5 = i\gamma_0\gamma_1\gamma_2\gamma_3 = \begin{pmatrix}-\sigma_0 & 0\\ 0 & \sigma_0\end{pmatrix}.$$

This leads to a decoupling into a left- and right-handed Weyl spinor

$$\bar{\sigma}^\mu \partial_\mu \psi_L = 0, \qquad \sigma^\mu \partial_\mu \psi_R = 0,$$

where $\bar{\sigma}^\mu = (\sigma^0, -\sigma^x, -\sigma^y, -\sigma^z)$. The Hamiltonian for a Weyl fermion with chirality $\chi = \pm 1$ is thus given by

$$H_{\text{Weyl}} = \psi^\dagger \mathcal{H}_{\text{Weyl}} \psi, \qquad \mathcal{H}_{\text{Weyl}} = \chi \hbar c \, \sigma^i k_i. \tag{2.19}$$

Similar to the Dirac fermions, a Weyl fermion has a linear-momentum dispersion.

Surprisingly, it turns out Dirac and Weyl fermions do not only exist in the realm of relativity theory but can be realized in the low-energy theory of condensed matter systems in which case the fermions are described by the Hamiltonians in Eqs. (2.18) and (2.19) with the speed of light c replaced by the Fermi velocity v_F. Systems that realize Dirac fermions are called Dirac semimetals. The first example of such a realization is the aforementioned appearance of two-dimensional, massless Dirac fermions in the effective low-energy theory of graphene [82]. The Dirac fermions are found around the K points in the hexagonal Brillouin zone, which reside exactly at the Fermi energy. The Haldane model and the model proposed by Kane and Mele introduce mass terms that open a non-trivial gap in these Dirac cones to find a Chern and $\mathbb{Z}_2$ insulator, respectively. The close relation between topology and Dirac theory is also revealed in the appearance of topologically non-trivial, two-dimensional Dirac fermions at the surfaces of three-dimensional topological insulators. Similarly, systems that feature Weyl fermions are called Weyl semimetals. The most prominent examples of such systems are three-dimensional Weyl semimetals that were first experimentally discovered in TaAs in 2015 [29, 30]. In analogy with three-dimensional topological insulators, a Weyl semimetal can be interpreted as the surface theory of a four-dimensional topological insulator. Whereas massless Dirac nodes can easily be gapped out because a mass term proportional to γ_0 can straightforwardly be introduced into the Hamiltonian, Weyl fermions are protected by the specific form of their Hamiltonian to which a mass term cannot be added. Weyl fermions are thus extremely robust against any perturbation, which already alludes to the fact that they are in fact protected by a topological invariant as is shown in the next section.

2.3.2 Weyl Semimetal

The close relation between topological phases and Dirac theory inspired the search for a similar connection between topology and other gapless phenomena. This resulted in the proposal of the Weyl semimetal [24–27], where the low-energy theory of the Weyl cones is given by

$$H_{\text{Weyl}} = \psi^\dagger \mathcal{H}_{\text{Weyl}} \psi, \qquad \mathcal{H}_{\text{Weyl}} = \chi \hbar v_F \mathbf{k} \cdot \boldsymbol{\sigma} + \left[\chi v_F \, p_F + E(\mathbf{k})\right] \sigma_0 \tag{2.20}$$

which is closely related to the Hamiltonian in Eq. (2.19) but with an additional momentum-dependent term $E(\mathbf{k})\sigma_0$, which tilts the Weyl cone and is usually forbidden in the high-energy context due to Lorentz invariance [83]. Note, however, that a strong contribution from gravity, which can for instance be found near the event horizon of a black hole, does allow for Weyl-node tilting [84]. Under certain conditions, $E(\mathbf{k})$ can overtilt the Weyl cone leading to a situation where the Fermi surface becomes infinite, the so-called type-II Weyl semimetals [85, 86]. Such overtilted cones are suspected to be the origin of many exotic features exhibited by Weyl semimetals, such as for instance extremely high magnetoresistance [87, 88], and much research is currently being into these materials. The specific form of the Hamiltonian prevents the addition of a mass term to the Weyl Hamiltonian in Eq. (2.20), which would result in a gap in the Weyl spectrum, and could thus be considered a signature of the robustness of Weyl nodes against perturbations. Indeed, there is a topological invariant associated with the Weyl node, which corresponds to its chirality χ and is given by the Chern number in Eq. (2.10), where the

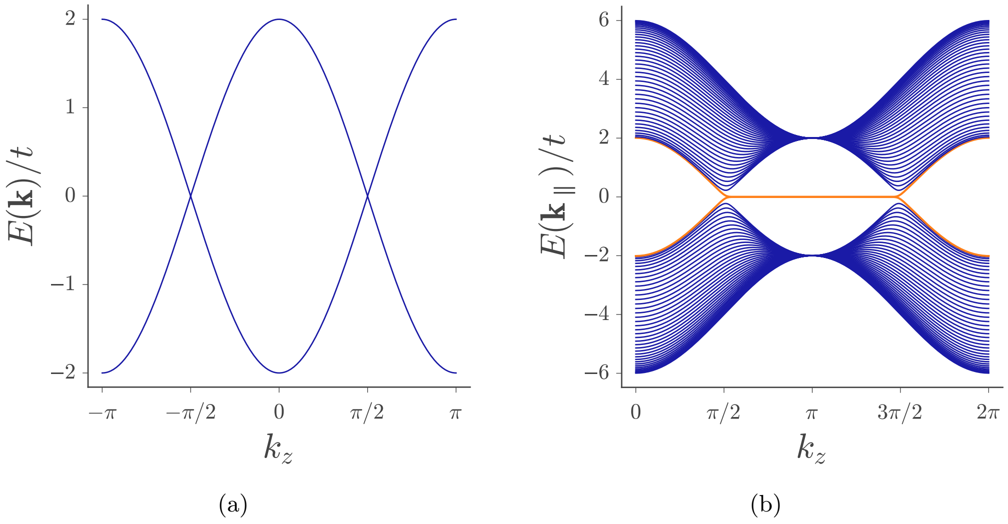

(a) (b)

Figure 2.4: (a) The eigenvalues for the Hamiltonian in Eq. (2.21) with $t = V = 1$ for varying k_z with the momentum cut $k_x = k_y = 0$. (b) The same system as in (a) with open boundary conditions in y and plotted for $N = 40$. The orange bands are the Fermi arcs.

integration in this case is over a sphere encapsulating the Weyl node. The Weyl node thus acts as a source or sink of Berry charge depending on its chirality. The chirality associated with the node also gives rise to the chiral anomaly (see e.g. Ref. [64]). Upon applying a magnetic field, the Weyl cone splits into Landau levels in the direction of the field while retaining the linear dispersion in the other directions. While all the Landau levels acquire a parabolic structure, the zeroth Landau level remains linear with the same chirality as the Weyl node and crosses the Fermi energy at $E_F = 0$. Upon the application of an electric field in the same direction as the magnetic field, electrons start moving, which results in an imbalance between the valence and conduction electrons. Therefore, the electromagnetic current is not preserved. As this is not allowed, there must always be an equal number of Weyl nodes in the system with opposite chirality. Another way to see this is by realizing that a Weyl node can be interpreted as a "magnetic" monopole, which is not allowed according to the Nielsen-Ninomiya theorem [89,90]. This is in accordance with the previous statement that the total Chern number of a band spectrum always has to be zero.

There are a plethora of tight-binding models which realize Weyl fermions in their low-energy theory. Due to the non-degenerate nature of the Weyl nodes, such theories need to include a (pseudo-)spin-orbit interaction to force the opposite (pseudo-)spin nodes apart. An example of a Weyl semimetal phase in a cubic lattice is presented here to illustrate the relative ease with which these models can be retrieved. The tight-binding model considered is introduced in Ref. 91 and corresponds to the Hamiltonian given in Eq. (2.5) with

$$\begin{aligned} &d_0(\mathbf{k}) = -2\,t\sin(k_x), \qquad d_x(\mathbf{k}) = 2\,t\sin(k_x), \qquad d_y(\mathbf{k}) = 2\,t\sin(k_y),\\ &d_z(\mathbf{k}) = 2\,t\cos(k_z) + 2\,V\,[2-\cos(k_x)-\cos(k_y)], \end{aligned} \tag{2.21}$$

where t is the nearest-neighbor hopping parameter and V is a staggering potential. This model features two Weyl nodes at $\mathbf{k}_\pm = (0,\,0,\,\pm\pi/2)$ as is shown in Fig. 2.4(a). Similar to the previously-discussed topological systems, Weyl semimetals possess robust surface states in the form of chiral Fermi arcs. They are a projection of the Fermi surface onto the boundaries of the system and can be interpreted as remnants of the chiral edge states of a Chern insulator. When a two-dimensional slice in a Weyl semimetal sweeps past a Weyl node with non-zero Chern number, the slice is penetrated by Berry flux and picks up the Chern number of the node. The slice is now a Chern insulator with chiral edge states. When sweeping past a Weyl node with opposite Chern number, the Chern number of the slice returns to zero and the slice returns to a topologically trivial state. The space between two Weyl nodes with opposite Chern number can thus be interpreted as a k-space stacking of Chern insulators with chiral edge states. From each of these edge states a point corresponding to the Fermi energy of the Weyl semimetal surfaces is picked up. These points connect and form chiral Fermi arcs that live on opposite surfaces and are connected via the Weyl nodes. The Fermi arcs can be identified in the energy spectrum of a Weyl semimetal with a surface as bands crossing the bulk gap as shown in Fig. 2.4(b) for the example on a cubic lattice where the system has open boundary conditions in the y-direction with the Hamiltonian given in Eq. (2.11) with

$$\begin{aligned}\mathcal{H}_k &= 2\,t\sin(k_x)\sigma_x + \{2\,t\cos(k_y) + 2\,V\,[2-\cos(k_x)]\}\,\sigma_z - 2\,t\sin(k_x)\sigma_0,\\ \mathcal{H}_\perp &= -it\,\sigma_y - V\sigma_z.\end{aligned} \tag{2.22}$$

Due to the degeneracy of the Fermi arcs between $k_z \in [\pi/2,\, 3\pi/2]$, it is not possible to study the localization of the bands. However, upon introducing an arbitrarily weak surface potential this degeneracy is lifted such that the arcs can be accessed.

In general, it should be noted that the Chern number associated with a Weyl node with a linear dispersion always equals ±1. Higher values for the Chern number can be achieved by generalizing the Hamiltonian to include higher-order dispersions. Moreover, one can show that if time-reversal symmetry is broken and inversion symmetry is preserved, a minimum of two Weyl nodes has to appear in the system, which is also the case for a system where symmetries are absent. When inversion symmetry is broken instead while time-reversal symmetry is preserved, a minimum of four Weyl nodes is required due to the rule that the total sum of Chern numbers has to vanish in a periodic band structure. If both symmetries are broken simultaneously, the only restriction on the number of Weyl cones is that it has to be even. However, in the case that both time-reversal symmetry and inversion symmetry are preserved, it automatically follows that $F_{ij}(\mathbf{k}) = 0$ and there are consequently no Weyl nodes. Moreover, the preservation of both symmetries forces two Weyl nodes with opposite charge to sit at the same place in momentum space and they form a two-fold degenerate Dirac node turning the system into a three-dimensional Dirac semimetal [92–96].

2.4 Boundary States

In all the previously-mentioned examples of topological systems, one returning feature is the famous bulk-boundary correspondence, where a non-trivial topological bulk invariant indicates the presence of robust boundary states. The observation of such states on the edges or surfaces of a material is an indication that this material may be in a topological phase. However, it must be mentioned at this point that the presence of a boundary state alone is by no means a prove of topology, as there are examples of other physical systems that feature such a state, such as for example the Fermi arcs that are present on the surfaces of high-T$_c$ superconductors (see e.g. [97]). Nevertheless, the importance of the boundary states should not be underestimated, because they are the only important aspect of topological states of matter from a technological perspective, and may be of practical use in the future. Boundary states can be experimentally observed by measuring the resistance of two-dimensional materials in a Hall bar geometry and using angle-resolved photoemission spectroscopy (ARPES) to probe the surface of three-dimensional systems. The latter technique can also be used to project the Fermi surface onto the material surface as to probe the bulk spectrum in order to confirm the expected bulk behavior. This way of detecting topological edge and surface states has resulted in the experimental confirmation of many theoretical proposals such as two- and three-dimensional topological insulators [10, 16, 17] and Weyl semimetals [28–30].

Despite the omnipresence of boundary states in topologically trivial and non-trivial systems, theoretical studies have mostly relied on numerical calculations. Having access to analytical solutions of the boundary states results in a better understanding of the boundary physics of topological materials because one can calculate, amongst other quantities, correlation functions, Chern numbers, and gap closings. Moreover, it sheds light on the interplay between bulk and boundary physics. There are, however, some examples of analytically acquired results. Famous exact solutions of boundary states in one-dimensional chains are for instance the spin-1/2 boundary states in the AKLT model that investigates the spin-1 Heisenberg chain [32], as well as, the Majorana modes recovered in the Kitaev chain [33]. Other efforts rely on the investigation of the suitability of Dirac Hamiltonians to model topological insulators. Edge states for Dirac Hamiltonians on a lattice with nearest-layer coupling are found [34], whereas, modified Dirac Hamiltonians are discussed in Ref. 35, where boundary solutions are found at interfaces separating sections with opposite Dirac mass in one- and two-dimensional systems, as well as, solutions in semi-infinite, one-, two- and three-dimensional models under some parameter conditions making use of effective Hamiltonians. Solutions are also found in two-dimensional topological insulators for the helical states in the HgTe quantum well approximated by a four-band model finding its origin in $\mathbf{k}\cdot\mathbf{p}$ perturbation theory [36,37] and in two-dimensional topological insulators modelled by the BHZ model presented in Ref. 9 on a square lattice [38], as well as in three-dimensional weak topological insulators at special points in the surface Brillouin zone [39]. An analytical solution for the Fermi arcs in a Weyl semimetal on the [001]-surface of a zinc-blende lattice with broken inversion symmetry is presented for semi-infinite system with a linearized model in Ref. 40. Lastly, solutions for the Andreev bound state in topological superconductors also exist [98]. Other works use the well-known method of transfer matrices to obtain surface solutions. Transfer matrices allow for a straight-forward computation of the boundary and bulk states in semi-infinite systems and systems with two edges or surfaces at a fixed energy [99,100]. The method requires a periodicity in lattice structure in the direction of the edge or surface and forbids hopping between these periodic cells. This method has been successfully applied to find solutions for topological edge states in two-dimensional topological systems [41–43].

The aforementioned results were found after extensive literature research but it can by no means be guaranteed that it captures all the published work related to analytically obtained equations describing topological boundary states. Nevertheless, they form an accurate reflection of the development in the field and give a general idea of what efforts have been made to recover analytical solutions. The majority of them only exists when the system is in the topological regime, heavily depend on the details of the Hamiltonian, and are not valid in the entire surface Brillouin zone. Those solutions recovered with the transfer matrix method are either found on a semi-infinite lattice, or for a fixed energy. In the accompanying paper, a new method is presented to find an exact wave-function solution in a system with two boundaries, which is valid over the entire boundary Brillouin zone and does not depend on these approximations. Moreover, unlike most known solutions, the validity of the wave-function solution is independent of the topological phase of the system and thus does not break down once the system becomes topologically trivial or non-trivial. This wave-function solution may localize when some requirements are met and corresponds to the topological boundary state when the lattice is in a topological phase.

Chapter 3

Geometrical Frustration and Flat Bands

This chapter discusses exact eigenstates on geometrically frustrated lattices. The kagome lattice is used as an example to explain how destructive interference leads to the natural occurrence of localized modes. By exploring this mechanism on a fully periodic lattice in Sect. 3.1, it is found that these modes are associated with a flat band. The accompanying energy spectrum has a degeneracy, which can be understood by using a counting argument. A similar phenomenon occurs in a model with boundaries, which is explored in Sect. 3.2, where the degeneracies are more intricate. Interestingly, different types of semi-localized modes are found, which are associated with dispersive bands. Wave-function solutions for these modes can be readily retrieved, and their form mirrors their potential to localize on either of the boundaries, which is in accordance with the behavior of topological edge and surface states.

3.1 Kagome Lattice

A prime example of geometrically frustrated lattices is the kagome lattice shown in Fig. 3.1(a). The basis vectors $\mathbf{a}_i$ and the nearest-neighbor vectors $\boldsymbol{\delta}_i$ read $\mathbf{a}_1 = (1,\, 0)$, $\mathbf{a}_2 = -(1,\, \sqrt{3})/2$ and $\mathbf{a}_3 = -(\mathbf{a}_1 + \mathbf{a}_2) = (-1,\, \sqrt{3})/2$ and $\boldsymbol{\delta}_1 = \mathbf{a}_1/2$, $\boldsymbol{\delta}_2 = \mathbf{a}_2/2$ and $\boldsymbol{\delta}_3 = \mathbf{a}_3/2$, respectively, with the lattice constant $a = 1$. Considering a real nearest-neighbor hopping model, the momentum-space Hamiltonian of the kagome lattice wrapped in a torus reads $H = \sum_{\mathbf{k}} \Phi_{\mathbf{k}}^{\dagger} \mathcal{H}_{\mathbf{k}} \Phi_{\mathbf{k}}$, where $\Phi_{\mathbf{k}}^{\dagger}$ has pseudo-spin (sublattice) degree of freedom and

$$\mathcal{H}_{\mathbf{k}} = 2\,t \begin{pmatrix} 0 & \cos(\mathbf{k}\cdot\boldsymbol{\delta}_1) & \cos(\mathbf{k}\cdot\boldsymbol{\delta}_3) \\ \cos(\mathbf{k}\cdot\boldsymbol{\delta}_1) & 0 & \cos(\mathbf{k}\cdot\boldsymbol{\delta}_2) \\ \cos(\mathbf{k}\cdot\boldsymbol{\delta}_3) & \cos(\mathbf{k}\cdot\boldsymbol{\delta}_2) & 0 \end{pmatrix}, \tag{3.1}$$

with t the nearest-neighbor hopping parameter and the on-site potential set to zero. The eigenvalues are

$$E_0 = -2\,t, \qquad E_{\pm}(\mathbf{k}) = t\left(1 \pm \sqrt{1 + 8\cos(\mathbf{k}\cdot\boldsymbol{\delta}_1)\cos(\mathbf{k}\cdot\boldsymbol{\delta}_2)\cos(\mathbf{k}\cdot\boldsymbol{\delta}_3)}\right), \tag{3.2}$$

as shown in Fig. 3.1(b). The band E_0 is a flat band, and there are touching points between E_0 and $E_-(\mathbf{k})$ at the $\Gamma = (0,\, 0)$ point in the Brillouin zone, and between $E_+(\mathbf{k})$ and $E_-(\mathbf{k})$ at the $K = (4\pi/3,\, 0)$ and $K' = (2\pi/3,\, 2\pi/\sqrt{3})$ points.

The eigenfunction solution associated with the flat band $\phi_0(\mathbf{k})$,

$$\phi_0(\mathbf{k}) = \frac{1}{\sqrt{\sum_{i=1}^{3} \sin^2(\mathbf{k}\cdot\boldsymbol{\delta}_i)}} \begin{pmatrix} \sin(\mathbf{k}\cdot\boldsymbol{\delta}_2) \\ \sin(\mathbf{k}\cdot\boldsymbol{\delta}_3) \\ \sin(\mathbf{k}\cdot\boldsymbol{\delta}_1) \end{pmatrix} \tag{3.3}$$

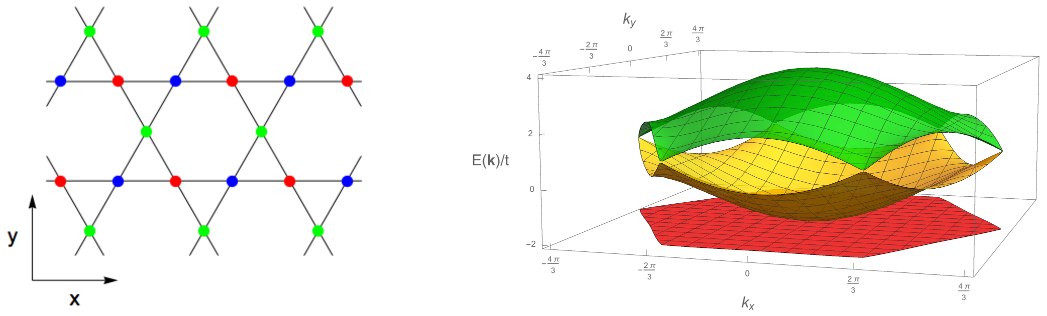

(a) (b)

Figure 3.1: (a) The kagome lattice with three sublattices in red, blue and green. (b) The energy spectrum of the kagome lattice described by the Hamiltonian in Eq. (3.1).

can be used to construct a localized mode in the kagome lattice shown schematically in Fig. 3.2(a). Following Ref. 58, one can define a creation operator for the localized modes $A^\dagger_{\mathbf{R}}$ on a plaquette

$$A^\dagger_{\mathbf{R}} = \mathcal{N} \int \mathrm{d}\mathbf{k}\, \mathrm{e}^{-i\mathbf{k}\cdot\mathbf{R}} \sum_{j=1}^{3} \sin\left(\mathbf{k}\cdot\boldsymbol{\delta}_{j+1}\right) c^\dagger_j(\mathbf{k}), \tag{3.4}$$

where an alternative notation for the eigenvector is used in terms of the creation operator $c^\dagger_j(\mathbf{k})$, which creates a particle with momentum $\mathbf{k}$ at site j, $\mathcal{N}$ is the normalization and $\mathbf{R}$ is the position at the center of the hexagonal plaquette. Note that the normalization factor of the eigenfunction was multiplied out because it complicates the integral while it does not influence the wavefunction qualitatively. Using that $\mathbf{R}$ is at the center of the plaquette and by explicitly writing out the sum and the sine functions, the creation operator reduces to

$$A^\dagger_{\mathbf{R}} = \frac{1}{\sqrt{6}} \sum_{j=1}^{6} (-1)^{j+1} c^\dagger_j, \tag{3.5}$$

where the normalization factor $\mathcal{N}$ was picked such that the operator is normalized, $c^\dagger_j$ creates a state at site j and the site corresponding to j is shown in Fig. 3.2(a). The localization of the plaquette mode is understood by considering a triangle on the lattice whose corners have the amplitudes $1/\sqrt{6}$, $-1/\sqrt{6}$ and 0. By hopping from the first two sites to the third, the hopping amplitudes cancel out. This phenomenon is called destructive interference, and a mode is localized if the hopping to all the sites outside the mode interfere out. To see that the mode is indeed an eigenfunction, one applies the real-space nearest-neighbor hopping Hamiltonian H_{nn} to the wave function sketched in Fig. 3.2(a) and finds $H_{nn}\,|\psi_{\hexagon}\rangle = -2t\,|\psi_{\hexagon}\rangle$ such that $|\psi_{\hexagon}\rangle$ is indeed an eigenfunction and its corresponding eigenvalue is $-2t$ in accordance with Eq. (3.2). Eqs. (3.1)-(3.5) are presented in Ref. 58 with Eqs. (3.3)-(3.5) forming part of the main results. They were rederived by the author of this licentiate thesis.

Whereas the band touchings in the energy spectrum in Fig. 3.1(b) at the K and K' points are required by symmetry arguments, the band touching at the Γ point is there because of a redundancy of states in the flat band [58]. This is understood by making use of a counting argument presented in Ref. 58. Assuming that the kagome lattice is fully periodic by wrapping it in a torus, one finds that the sum of the plaquette operator must be zero $\sum_{\mathbf{R}} A^\dagger_{\mathbf{R}} = 0$ at $\mathbf{k} = 0$. This can be straightforwardly understood from the example shown in Fig. 3.2(b) where the sum over three plaquette operators shows that the amplitude on each site shared by neighboring plaquettes is cancelled out while making use of the fact that the Bloch phase vanishes for $\mathbf{k} = 0$. This means that in a system of N plaquettes, there are $(N-1)$ independent states and there

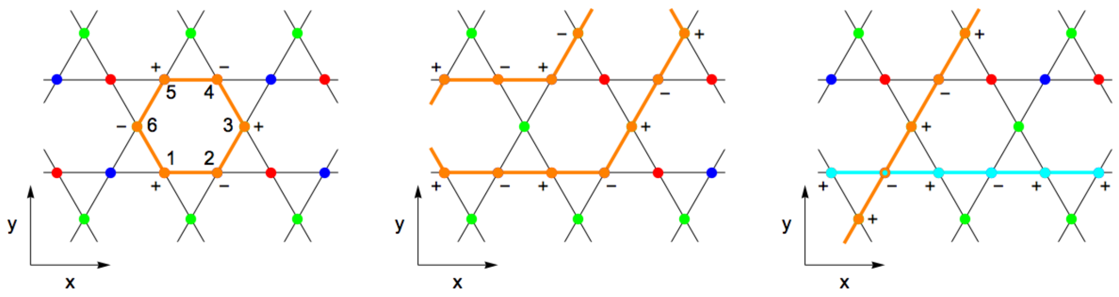

(a) (b) (c)

Figure 3.2: (a) Localized mode on the boundary of one plaquette as described by the operator in Eq. (3.5). The wave function has non-zero and equal weight on the orange sites, and zero weight on all other sites. The sign of the phase changes as indicated by + and − signs. (b) Sum of three localized modes at $\mathbf{k} = 0$. (c) Two non-contractible loops on the torus.

is thus a state missing in the flat band. This state is found upon realizing that there are two non-contractable loops in the torus that also correspond to the localized mode in Eq. (3.3) shown in Fig. 3.2(c). There are thus $(N + 1)$ states in the flat band in agreement with the touching point in the energy spectrum.

3.2 Localized Modes on Kagome Lattice with Boundaries

In the previous section, it was shown that localized modes are natural inhabitants of geometrically frustrated lattices, and that they are associated with a flat band in the energy spectrum. These are well-known and well-established results. A similar phenomenon occurs in lattice models that are not completely periodic but instead feature boundaries. When wrapping the kagome lattice in a cylinder as shown in Fig. 3.3(a), it is more straightforward to think about the lattice as being composed of red-blue and intermediate green chains that are stacked in an alternating fashion. Choosing the cylinder to start and terminate with a red-blue chain, the Hamiltonian for this model reads

$$H = \sum_k \Psi_k^\dagger \mathcal{H}_k^N \Psi_k, \qquad \mathcal{H}_k^N = \begin{pmatrix} \mathcal{H}_k & \mathcal{H}_\perp^A & 0 & 0 & 0 \\ \mathcal{H}_\perp^{\dagger,A} & h_k & \mathcal{H}_\perp^{\dagger,B} & 0 & 0 \\ 0 & \mathcal{H}_\perp^B & \mathcal{H}_k & \cdots & 0 \\ 0 & 0 & \vdots & \ddots & \mathcal{H}_\perp^{\dagger,B} \\ 0 & 0 & 0 & \mathcal{H}_\perp^B & \mathcal{H}_k \end{pmatrix}, \tag{3.6}$$

with N the total number of red-blue chains, Ψ_k the annihilation operator with sublattice degree of freedom and

$$\mathcal{H}_k = t\cos\left(\frac{k}{2}\right)\sigma_x, \qquad h_k = 0, \qquad \mathcal{H}_\perp^A = \left(\mathcal{H}_\perp^B\right)^* = \frac{t}{2}\begin{pmatrix} \mathrm{e}^{-i\frac{k}{4}} \\ \mathrm{e}^{i\frac{k}{4}} \end{pmatrix}, \tag{3.7}$$

with $\mathcal{H}_k$ the Hamiltonian for the red-blue chain, h_k the Hamiltonian for the intermediate green chain, and $\mathcal{H}_\perp^A$ and $\mathcal{H}_\perp^B$ the Hamiltonians describing how the red-blue and intermediate green chains are connected. The Hamiltonian in Eq. (3.6) corresponds to the Hamiltonian in Eq. (2) in the accompanying paper. The energy spectrum of this model features a degenerate flat band where the degree of degeneracy equals the number of green chains as shown in Fig. 3.3(b). Due to the open boundary conditions in the y direction, there are now $(N-1)$ different plaquettes on which a localized mode can be defined as shown schematically in Fig. 3.4(a). As for the kagome

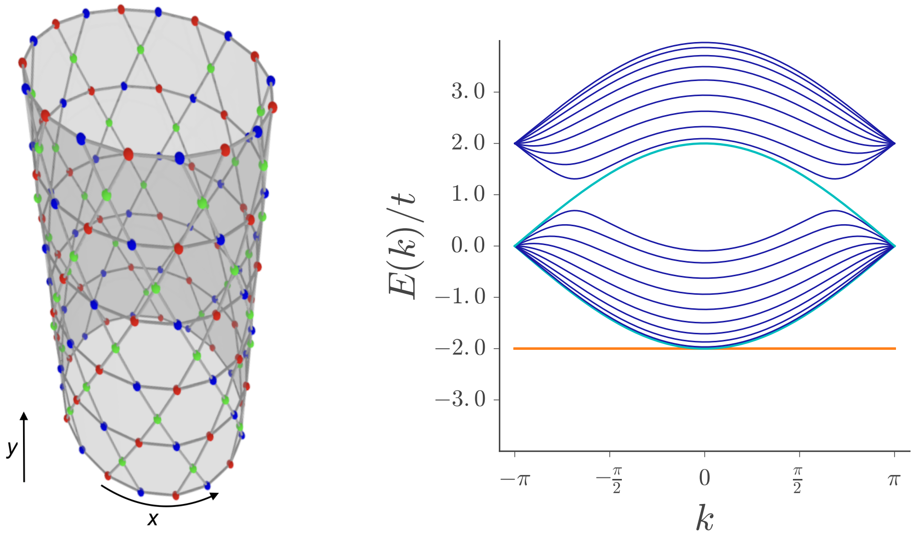

(a) (b)

Figure 3.3: (a) The kagome lattice wrapped in a cylinder with open boundary conditions in the y direction. (b) Energy spectrum of the Hamiltonian in Eqs. (3.6) and (3.7) with $N = 10$. The orange band is nine-fold degenerate, and in general is $N-1$-fold degenerate. The orange band and cyan bands are associated with the modes shown in Figs. 3.4 and 3.5, respectively.

lattice on a torus, there is a touching point in the band spectrum at $k = 0$. The localized modes corresponding to this point in the Brillouin zone are shown in Fig. 3.4(b), and can be related to the localized modes in Fig. 3.4(a) by picking the appropriate gauge θ for the following general solution of the flat band

$$|\Psi_{\text{flat}}(k)\rangle = \sum_R \mathrm{e}^{-ikR+i\theta R} d_R^\dagger |0\rangle \,,$$

where $d_R^\dagger$ is an operator that creates a localized plaquette mode at position R similar to the plaquette operator in Eq. (3.5), $|0\rangle$ is the vacuum and θ a gauge choice. The band spectrum also features a touching point at $k = \pm\pi$, where the number of bands reduces to three. This can be understood by realizing that at $k = \pm\pi$ the Hamiltonian reduces to $\mathcal{H}_{k=\pm\pi} = 0$ and $\mathcal{H}_\perp^{\dagger,A} = \frac{t}{2\sqrt{2}}(1 \mp i,\, 1 \pm i)$ such that diagonalizing $\mathcal{H}_k^N$ leads to $E(k=\pm\pi)/t = -2, 0, 2$ for any N. These touching points are thus a consequence of the inherent symmetry of the model.

3.3 Semi-Localized Modes on Kagome Lattice with Boundaries

Besides the flat band, there are also two semi-localized modes in the system shown in Fig. 3.5 corresponding to the cyan bands in Fig. 3.3(b). Studying the modes on each separate red-blue chain, one notices that they resemble the eigensystem of the red-blue chain Hamiltonian $\mathcal{H}_k$

$$E_\pm(k) = \pm\, t\cos\left(\frac{k}{2}\right), \qquad |\Phi_\pm\rangle = \frac{1}{\sqrt{2}}\begin{pmatrix}1\\ \pm 1\end{pmatrix}. \tag{3.8}$$

The wave-function solution for the two semi-localized modes in Fig. 3.5 can thus be written as

$$|\Psi_\pm\rangle = \bigoplus_{m=1}^{N} r_\pm^m \, |\Phi_\pm\rangle_m \,, \tag{3.9}$$

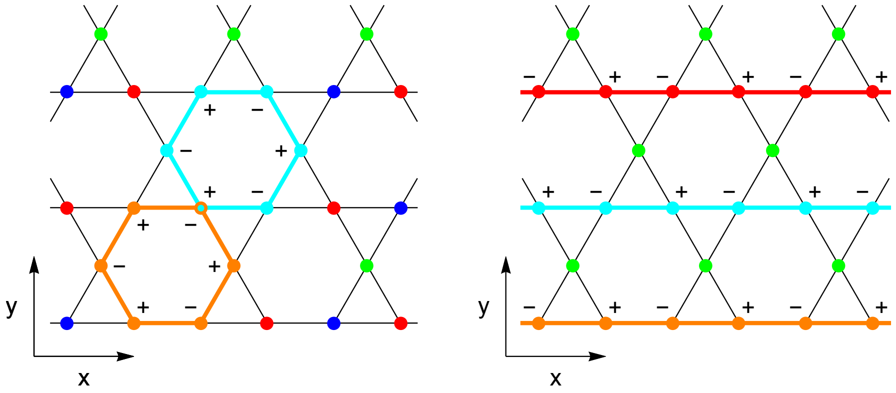

(a) (b)

Figure 3.4: Sketch of localized modes on the kagome lattice wrapped in a cylinder. The same conventions are used as in Fig. 3.2. Localized modes corresponding to the flat band in Fig. 3.3(b) (a) away from $k = 0$ in the Brillouin zone and (b) at $k = 0$.

where m labels the red-blue chains, such that this wave function has a zero-amplitude on the intermediate green chains. Solving the Schrödinger equation

$$\mathcal{H}_k^N \Psi_\pm = E_\pm^N(k)\Psi_\pm,$$

yields the following two equations

$$\mathcal{H}_k \Phi_\pm = E_\pm^N(k)\Phi_\pm, \tag{3.10}$$

$$\mathcal{H}_\perp^{\dagger,A}\Phi_\pm + r_\pm \mathcal{H}_\perp^{\dagger,B}\Phi_\pm = 0 \quad \Rightarrow \quad r_\pm = -\frac{\mathcal{H}_\perp^{\dagger,A}\Phi_\pm}{\mathcal{H}_\perp^{\dagger,B}\Phi_\pm}, \tag{3.11}$$

where it should be noted that the right-hand side of the last equation reduces to a scalar. Eq. (3.10) shows that the eigenvalues associated with $|\Psi_\pm(k)\rangle$ correspond to the eigenvalue solutions of $\mathcal{H}_k$, i.e. $E_\pm^N(k) = E_\pm(k)$, and from Eq. (3.11) in combination with Eqs. (3.7) and (3.8) it follows that $r_+ = -1$ and $r_- = 1$. The solution in Eq. (3.9) therefore correctly describes the semi-localized modes in Fig. 3.5.

3.4 Generalized Hoppings on Kagome Lattice with Boundaries

From the Hamiltonian in Eq. (3.6) it can be seen that Eq. (3.9) is a solution regardless of Hamiltonian details as long as the red-blue chains do not communicate with each other directly. The validity of the wave-function solution in Eq. (3.9) thus originates directly from the lattice geometry. Whereas allowing for hoppings different from real nearest-neighbor hoppings results in the immediate disappearance of the localized modes, the solution in Eq. (3.9) simply acquires a momentum dependence and is written more generally as

$$|\Psi_\pm(k)\rangle = \mathcal{N}_\pm(k) \bigoplus_{m=1}^{N} (r_\pm(k))^m \, |\Phi_\pm(k)\rangle_m \,, \tag{3.12}$$

where $\mathcal{N}_\pm(k)$ is the overall normalization factor

$$\mathcal{N}_\pm(k) = \sqrt{\frac{|r_\pm(k)|^2 - 1}{(|r_\pm(k)|^2)^N - 1}}. \tag{3.13}$$

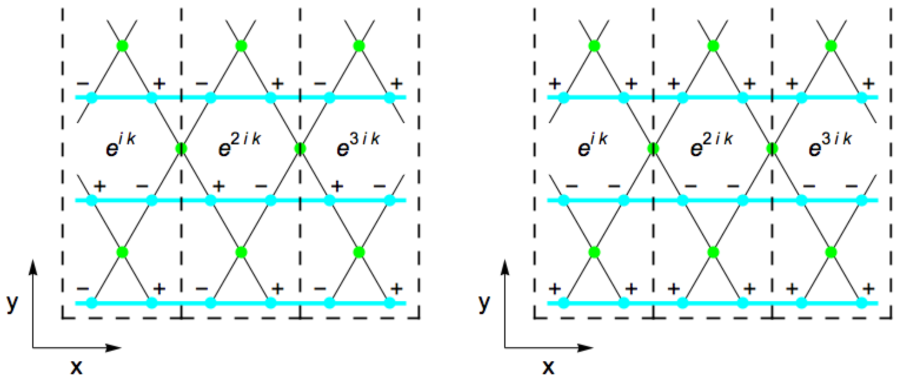

(a) (b)

Figure 3.5: Sketch of semi-localized modes on the kagome lattice wrapped in a cylinder with the unit cell indicated by dashed lines and the Bloch phase written in each unit cell. The same conventions are used as in Fig. 3.2. The modes correspond to the (a) bottom and (b) top cyan band in Fig. 3.3(b).

Similarly, the equations in Eqs. (3.10) and (3.11) pick up a momentum dependence and now read

$$\mathcal{H}_k\Phi_\pm(k) = E^N_\pm(k)\Phi_\pm(k), \qquad r_\pm(k) = -\frac{\mathcal{H}^{\dagger,A}_\perp\Phi_\pm(k)}{\mathcal{H}^{\dagger,B}_\perp\Phi_\pm(k)}. \tag{3.14}$$

Eqs. (3.12), (3.13), and (3.14) correspond to eqs.(4)-(7) in the accompanying paper. Interestingly, the solution in Eq. (3.12) corresponds to an exponentially localized mode when $|r_\pm(k)| \neq 1$, which can be seen both from the inverse localization length

$$\xi_\pm(k) = \frac{1}{\ln|r_\pm(k)|}, \tag{3.15}$$

and the weight of the wave function per red-blue chain m

$$P_{\pm,m}(k) = |\mathcal{N}_\pm(k)|^2|r_\pm(k)|^{2m}, \tag{3.16}$$

derived from Eq. (2.13). Imposing the appropriate Hamiltonian on the kagome lattice may thus result in the appearance of localized edge modes described by the exact wave-function solution in Eq. (3.12), which correspond to topological edge states if the correct symmetries are preserved and/or broken by the lattice Hamiltonian.

Lastly, when the cylinder is allowed to end with a green chain instead of terminating with a red-blue chain, the eigenfunction in Eq. (3.12) is still a solution for this model as long as

$$r_\pm(k)\,\mathcal{H}^{\dagger,A}_\perp\Phi_\pm(k) = 0,$$

which leads to

$$\mathcal{H}^{\dagger,A}_\perp\Phi_\pm(k) = 0, \tag{3.17}$$

where the other solution $r_i(k) = 0$ leads to the same equation. This is an extremely strict constraint on the validity of the wave function, and for the example with real nearest-neighbor hopping only holds for Φ_+ when $\cos(k/4) = 0, k \in 2\pi \bmod 4\pi$ and for Φ_- when $\sin(k/4) = 0, k \in 0 \bmod 4\pi$. The same situation is encountered for the case where the cylinder has two green chains as its edges, where one has to satisfy an extra constraint on top of the previous one

$$r_\pm(k)\,\mathcal{H}^{\dagger,B}_\perp\Phi_\pm(k) = 0 \quad\Rightarrow\quad \mathcal{H}^{\dagger,B}_\perp\Phi_\pm(k) = 0, \tag{3.18}$$

which in the example of real nearest-neighbor hopping only on the kagome lattice does not alter the just-mentioned conditions for Φ_+ and Φ_-. By allowing a termination with one or two B lattices, the solution in Eq. (3.12) thus remains valid at some points in the Brillouin zone. Nevertheless, the exact solution is much more general in that it is valid in the entire surface Brillouin zone by only studying cases where the lattices end with A lattices only.

Chapter 4

Summary of Accompanying Paper

This chapter introduces the work that is presented in the accompanying paper, which is written by the author of this licentiate thesis, Maximilian Trescher and Emil J. Bergholtz and was published in Physical Review B on August 30, 2017 with the title *Anatomy of topological surface states: Exact solutions from destructive interference on frustrated lattices* [1]. In ch. 2 it was highlighted that even though topological edge and surface states are a signature feature of topological phases of matter, no general, exact solutions exist to describe their wave functions. By studying the natural localization of modes on frustrated lattices in ch. 3, a formalism was developed with which solutions are retrieved that in some cases correspond to topological boundary states. A generalized version of this formalism and its application to explicit examples are the main results of the accompanying paper [1], and are summarized in this chapter by first reviewing the general framework of the method after which its application to examples is outlined.

4.1 General Framework

The formalism outlined in the previous chapter to finding exact solutions for semi-localized modes is extremely general. Even though flat bands and exactly localized modes disappear on frustrated lattices when exotic hopping terms such as spin-orbit coupling are included in the Hamiltonian or a magnetic field is applied, the solutions in Eqs. (3.12)-(3.14) persist and their existence is completely independent of Hamiltonian details. In addition, these solutions are valid for a large class of geometrically frustrated lattices beyond the kagome lattice, which is discussed in the following.

Lattices that harbor solutions of the from of Eq. (3.12) fulfill three conditions, which were already implicitly mentioned in the previous chapter. In accordance with the labelling in the accompanying paper, the first condition simply states that (i) the lattices can be decomposed into two periodic building blocks, the A and B lattices, which are stacked in an alternating fashion to form a system, which terminates with A lattices on both sides. For the example of the kagome lattice, the A lattice corresponds to the red-blue chains and the B lattice to the green chain. The second condition ensures the presence of destructive interference by (ii) disallowing any direct hopping between the A lattices. It is straightforward to see from Eq. (3.12) that allowing such hopping terms would result in a non-zero weight on the B lattices, which invalidates the exact wave-function solution. However, it should be noted that whereas allowing for such hopping terms destroys the analytical solution, as long as they are not strong enough they do not have an effect on the physical phase of the system. If the model is in a topologically non-trivial phase, it will remain to be in this phase if hoppings between A lattices are switched on. This condition therefore does not have as restrictive a nature as may seem at first because models fulfilling this condition are simply adiabatically connected to models that do allow for hoppings between the A lattices. The third condition dictates that (iii) the A and B lattices are stacked such that the system is geometrically frustrated meaning that there is an inequivalent way to hop from the A lattices to the B lattice. Together with condition (ii) this leads to a local constraint, which is satisfied by the exact wave-function solution in Eq. (3.12).

When conditions (i)-(iii) are satisfied, the solutions in Eqs. (3.12)-(3.14) exist regardless of the presence of a topologically trivial or non-trivial phase. This wide applicability of the formalism sets the method in the accompanying paper apart from other methods summarized in sect. 2.4, where the solutions are typically only valid in the topological regime. The solution in Eq. (3.12) corresponds to a topological boundary state when two additional conditions are fulfilled, referred to as conditions (iv) and (v) in the accompanying paper. Firstly, (iv) the local constraint has to involve more than one minimal unit cell in one of the A lattices or the hopping strength between the A and B lattices has to be inequivalent. Secondly, (v) the A lattice Hamiltonian has to support the relevant topological phase. Condition (iv) is essential to facilitating the localization of the state, and solely fulfilling this condition can lead to the localization of a state to the boundary albeit not topological protected. A topological phase only appears on the lattice when conditions (iv) and (v) are satisfied simultaneously.

This method to finding exact wave-function solutions for topological boundary states was inspired by earlier work by the two co-authors of the accompanying paper, where they find exact solutions for Fermi arcs in pyrochlore lattices [101, 102]. In the accompanying paper, the technique used in those works is generalized to be applicable to any topological phase, and on a large class of geometrically frustrated lattices. This generalized formalism has not been presented elsewhere, and Eqs. (3.12)-(3.14) form the main result of the accompanying paper where they correspond to Eqs. (4)-(7). The exact form of the topological boundary state allows for the analytical analysis of several quantities that are usually only numerically accessible. Firstly, through studying the behavior of the function $|r_i(\mathbf{k})|$, the localization of the wave function to the boundaries is determined analytically by either computing the localization length given in Eq. (3.15) or the weight of the wave function on each A layer given in Eq. (3.16). The value of $|r_i(\mathbf{k})|$ may change in the surface Brillouin zone from smaller than one to larger than one or vice versa such that the wave function switches boundaries. Surface switching requires that there is some point in the Brillouin zone $\mathbf{q}$ where $|r_i(\mathbf{q})| = 1$, where the state is completely delocalized in the system. This behavior of surface switching is observed when looking at explicit examples, and is also mentioned in the next section. Secondly, an explicit relation for the gap closing between the boundary band and the bulk bands is also computed by making use of perturbation theory. It is shown that at the point in the Brillouin zone $\mathbf{q}$ where the state completely delocalizes, i.e. $|r_i(\mathbf{q})| = 1$, the band gap between the boundary band and the bulk bands behaves as N^{-2}, where N is the total number of A lattices. It is therefore proven that for an infinitely large system, the boundary state fully attaches to the bulk at those points in the Brillouin zone where the state is completely delocalized. Thirdly, by making use of the exact solution for the wave function for three-dimensional models an equation for the Chern number, which is the relevant topological invariant for Chern insulators and Weyl semimetals, is derived in terms of the Berry curvature of the two-dimensional A layer. Using the resulting formula, it is shown that if $|r_i(\mathbf{k})| = 1$, the Chern number of the total system simply equals the Chern number of the single A layer. More interestingly, it is observed in the examples that in the case $|r_i(\mathbf{k})| \neq 1$, the total Chern number of a model with N stacked A layers equals N times the Chern number of the single A layer, which means that the two-dimensional surface state absorbs the Chern number of each A layer. Lastly, assuming models with only two degrees of freedom on each A lattice such that their Hamiltonian can be written in the general form of Eq. (2.5), it is shown by making use of the form of the Chern number in Eq. (2.10) that a finite Chern number on the A lattices always leads to the appearance of a Fermi arc.

4.2 Topological Boundary States

To demonstrate the versatility of the developed formalism, one-, two- and three-dimensional examples are discussed in the accompanying paper. In the one-dimensional case, a ladder-like lattice is studied in which it is found that localized end modes can exist on either end or at the same end of the ladder. To render these modes topological, the tenfold way dictates that either a chiral or a superconducting theory is required [18], which is beyond the scope of the work. This example therefore does not fulfill condition (v) such that the end modes discussed in the paper are not topologically protected.

To study the role of condition (iv), it is shown in three two-dimensional examples that when this condition is not satisfied, no topological phase can be retrieved on the lattice. The kagome lattice is studied as a fourth two-dimensional example, which does satisfy condition (iv). By satisfying condition (v), a Chern-insulating phase is recovered whose chiral edge states are described by the exact wave-function solution in Eq. (3.12). By plotting the inverse localization length in Eq. (3.15), the localization of the chiral states is explicitly shown. The function $r_\pm(k_x)$ varies over varying momentum k_x from values smaller than one to values larger than one in accordance with the chirality of the associated band. This ensures that the right mover localizes to one end of the cylinder and the left mover to the other end in a consistent fashion. It is mentioned in the accompanying paper that a $\mathbb{Z}_2$-insulating phase can be straightforwardly realized on the kagome lattice by simply taking two time-reversed copies of the already-implemented Chern insulator. In this case, there are four exact wave-function solutions as in Eq. (3.12), which correspond to the helical edge states. Their localization can be studied in a similar fashion to the Chern-insulator edge states.

Lastly, topologically non-trivial models in three dimensions are also explored, in which case a Weyl semimetal phase is found in both the pyrochlore lattice and a toy model coined the checkerboard model. These phases are generated by implementing a Chern insulator on each of the two-dimensional A layers. The wave-function solution in Eq. (3.12) now corresponds to Fermi arcs, and through studying the function $r_i(\mathbf{k})$ the surface switching of the Fermi arcs is explicitly shown. Interestingly, regimes are found in which a Fermi arc with non-zero Chern number exists in the absence of Weyl points. This observation was derived from exact calculations and as such does not rely on any approximation. The robustness of these Fermi arcs against perturbations is not understood because the presence of a Chern number suggests topological protection, whereas the absence of Weyl nodes suggests the opposite, and requires further investigation. Even though it is not treated explicitly in the accompanying paper, Dirac semimetals can also be realized on these lattices by restoring time-reversal symmetry through taking two time-reversed copies of the Weyl semimetal. As Dirac semimetals are not topological, the exact wave-function solution in Eq. (3.12) no longer corresponds to a topological boundary state in this case. Similar to the topologically-trivial two-dimensional examples, it is shown that it is not possible to find a topological phase when condition (iv) is not fulfilled in a three-dimensional model composed of honeycomb lattices.

In addition to the topological phases discussed in the paper, other, more exotic, topological phases can also be realized, some of which have already be implemented by the author of this licentiate thesis after the accompanying paper was published. These models and other future research directions are discussed in the next chapter.

Chapter 5

Outlook

As was already mentioned in the previous chapter, exact solutions have also been found for topological phases that have not been discussed in the accompanying paper. Through discussion with Guido van Miert, a PhD student and collaborator at the University of Utrecht in the Netherlands, it was realized that the exact solution persists when the third condition pertaining to having a frustrated lattice geometry is relaxed. In fact, only satisfying conditions (i) and (ii) and assuming a vanishing amplitude on the B lattices are sufficient ingredients to finding an exact solution of the form of Eq. (3.12). This generalization of the method is currently being explored and will result in a follow-up publication. Using this new insight, exact solutions for edge states have been found on graphene, as well as for nodal lines in hyperhoneycomb lattices.

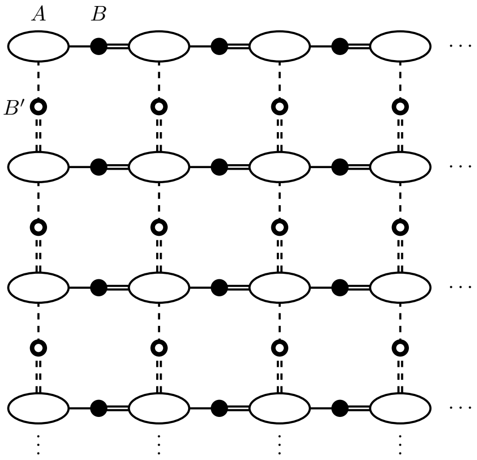

Figure 5.1: Schematic figure of a lattice consisting of stacked $(d-2)$-dimensional lattices A, B and B' on which exact wave-function solutions can be found.

Moreover, this discussion also led to the realization that exact wave-function solutions also exist when considering a d-dimensional lattice that consists of stacked $(d-2)$-dimensional lattices, as long as a similar repetitive structure of lattice stacking as described in condition (i) is preserved. An example of such as lattice is shown in Fig. 5.1. The exact solutions on this lattice are of a similar form as in Eq. (3.12) but with additional $r_i(\mathbf{k})$ factors for each direction of stacking. This realization has also led to retrieval of exact solutions for hinge states in the pyrochlore lattice by the author of this paper. These higher order topological phases have recently been proposed to exist on corners or hinges of two- or two- and three-dimensional lattices [103–109]. By combining the exact solutions in the kagome and pyrochlore lattices, chiral hinge states have been isolated that live on all four hinges of a rhombus-spahed pyrochlore system that is periodic in one direction. Further explorations of different shapes of the pyrochlore lattice and different models will lead to a new publication.

Other future projects derived from the work in the accompanying paper relate to the realization of topological phases that have chiral symmetries or are superconducting. One of the aims is to see whether topological boundary solutions can be retrieved for all the topological phases that are described in the tenfold way [18].

Lastly, as was already mentioned in the previous chapter, it is not obvious whether the Fermi arcs that have a non-zero Chern number but appear in a system with no Weyl nodes are robust against disorder. It would be interesting to test their stability against such effects.

Acknowledgements

I would like to thank my former colleagues at the Free University Berlin from whom I have learned a lot about the field of topology, and with whom I have enjoyed many lunches, conferences, drinks on the rooftop, the occasional canoeing trip and other experiences: Björn Sbierski, Max Hering, Marese Rieder, Thomas Kiendl, Jörg Berhman, Zhao Liu, Piet Brouwer and many others.

Moreover, I would like to thank my new colleagues here at the University of Stockholm with whom I have discussed about varying topics, some relating to physics, visited conferences, and drink the occasional coffees: Thomas Kvorning, Iman Mahyaeh, Axel Gagge, Pil Saugmann, Irina Dumitru, Johan Carlstrom, Yaron Kedem, Eddy Ardonne and many others.

I would like to thank Christian Spånslätt for lending me his licentiate thesis so that I had some idea of what was expected of the content.

I would like to thank Guido van Miert for fruitful discussions relating to the work, and the future projects this has resulted in.

I would like to thank Maximilian Trescher with whom I have attended and enjoyed many conferences, from whom I have learned a lot and who gave me his python code and helped me whenever I had problems with the computer. He is a co-author on the accompanying paper, where he contributed the work on the pyrochlore lattices.

Lastly, I would like to thank my PhD supervisor Emil Bergholtz. I started working for him in Berlin and have followed him to Stockholm. I have learned a lot about physics from him over the last years, and he inspires me to keep on learning. I thank him for his support, teaching me all the things I do not know, and carefully reading all the texts I write and scrutinizing all the talks I give. Moreover, I thank him for the many opportunities I have gotten to attend conferences, start new collaborations and to travel all over the world. It is truly a pleasure to be part of his research group.

Bibliography

[1] F.K. Kunst, M. Trescher, and E.J. Bergholtz, *Anatomy of Topological Surface States: Exact Solutions from Destructive Interference on Frustrated Lattices*, Phys. Rev. B **96**, 085443 (2017).

[2] K. von Klitzing, G. Dorda, and M. Pepper, *New Method for High-Accuracy Determination of the Fine-Structure Constant Based on Quantized Hall Resistance*, Phys. Rev. Lett. **45**, 494 (1980).

[3] C.L. Kane and E.J. Mele, *Quantum Spin Hall Effect in Graphene*, Phys. Rev. Lett. **95**, 226801 (2005).

[4] C. L. Kane and E. J. Mele, *Z_2 Topological Order and the Quantum Spin Hall Effect*, Phys. Rev. Lett. **95**, 146802 (2005).

[5] F.D.M. Haldane, *Model for a Quantum Hall Effect without Landau Levels: Condensed-Matter Realization of the "Parity Anomaly"*, Phys. Rev. Lett. **61**, 2015 (1988).

[6] C.-Z. Chang, J. Zhang, X. Feng, J. Shen, Z. Zhang, M. Guo, K. Li, Y. Ou, P. Wei, L.-L. Wang, Z.-Q. Ji, Y. Feng, S. Ji, X. Chen, J. Jia, X. Dai, Z. Fang, S.-C. Zhang, K. He, Y. Wang, L. Lu, X.-C. Ma, and Q.-K Xue, *Experimental Observation of the Quantum Anomalous Hall Effect in a Magnetic Topological Insulator*, Science **340**, 167 (2013).

[7] G. Jotzu, M. Messer, R. Desbuquois, M. Lebrat, T. Uehlinger, D. Greif, and T. Essliner, *Experimental realization of the topological Haldane model with ultracold fermions*, Nature **515**, 237 (2014).

[8] B. A. Bernevig and S.-C. Zhang, *Quantum Spin Hall Effect*, Phys. Rev. Lett. **96**, 106802 (2006).

[9] B. A. Bernevig, T. L. Hughes, and S.-C. Zhang, *Quantum Spin Hall Effect and Topological Phase Transition in HgTe Quantum Wells*, Science **314**, 1757 (2006).

[10] M. König, S. Wiedmann, C. Brüne, A. Roth, H. Buhmann, and L. W. Molenkamp, *Quantum Spin Hall Insulator State in HgTe Quantum Wells*, Science **318**, 766 (2007).

[11] D. Xiao, M.-C. Chang, and Q. Niu, *Berry phase effects on electronic properties*, Rev. Mod. Phys. **82**, 1959 (2010).

[12] L. Fu, C. L. Kane, and E. J. Mele, *Topological Insulators in Three Dimensions*, Phys. Rev. Lett. **98**, 106803 (2007).

[13] J. E. Moore and L. Balents, *Topological invariants of time-reversal-invariant band structures*, Phys. Rev. B **75**, 121306(R) (2007).

[14] X. Dai, T. L. Hughes, X.-L. Qi, Z. Fang, and S.-C. Zhang, *Helical edge and surface states in HgTe quantum wells and bulk insulators*, Phys. Rev. B **77**, 125319 (2008).

[15] J. C. Y. Teo, L. Fu, and C. L. Kane, *Surface states and topological invariants in three-dimensional topological insulators: Application to* $Bi_{1-x}Sb_x$, Phys. Rev. B **78**, 045426 (2008).

[16] D. Hsieh, D. Qian, L. Wray, Y. Xia, Y. S. Hor, R. J. Cava, and M. Z. Hasan, *A topological Dirac insulator in a quantum spin Hall phase*, Nature **452**, 970 (2008).

[17] Y. Xia, D. Qian, D. Hsieh, L. Wray, A. Pal, H. Lin, A. Bansil, D. Grauer, Y. S. Hor, R. J. Cava, and M. Z. Hasan, *Observation of a large-gap topological-insulator class with a single Dirac cone on the surface*, Nature Physics **5**, 398 (2009).

[18] A. P. Schnyder, S. Ryu, A. Furusaki, and A. W. W. Ludwig, *Classification of topological insulators and superconductors in three spatial dimensions*, Phys. Rev. B **78**, 195125 (2008).

[19] R.-J. Slager, A. Mesaros, V. Juričić, and J. Zaanen, *The space group classification of topological band-insulators*, Nature Phys. **9**, 98 (2013).

[20] L. Fu, *Topological Crystalline Insulators*, Phys. Rev. Lett. **106**, 106802 (2011).

[21] T. H. Hsieh, H. Lin, J. Liu, W. Duan, A. Bansil, and L. Fu, *Topological crystalline insulators in the SnTe material class*, Nature Commun. **3**, 982 (2012).

[22] S.-Y. Xu, C. Liu, N. Alidoust, M. Neupane, D. Qian, I. Belopolski, J. D. Denlinger, Y. J. Wang, H. Lin, L. A. Wray, G. Landolt, B. Slomski, J. H. Dil, A. Marcinkova, E. Morosan, Q. Gibson, R. Sankar, F. C. Chou, R. J. Cava, A. Bansil, and M. Z. Hasan, *Observation of a topological crystalline insulator phase and topological phase transition in* $Pb_{1-x}Sn_xTe$, Nature Commun. **3**, 1192 (2012).

[23] P. Dziawa, B. J. Kowalski, K. Dybko, R. Buczko, A. Szczerbakow, M. Szot, E. Łusakowska, T. Balasubramanian, B. M. Wojek, M. H. Berntsen, O. Tjernberg, and T. Story, *Topological crystalline insulator states in* $Pb_{1?x}Sn_xSe$, Nature Mat. **11**, 1023 (2012).

[24] G.E. Volovik, *The Universe in a Helium Droplet* (Clarendon, Oxford, 2003).

[25] S. Murakami, *Phase transition between the quantum spin Hall and insulator phases in 3D: emergence of a topological gapless phase*, New J. Phys. **9**, 356 (2007).

[26] X. Wan, A. M. Turner, A. Vishwanath, and S. Y. Savrasov, *Topological semimetal and Fermi-arc surface states in the electronic structure of pyrochlore iridates*, Phys. Rev. B **83**, 205101 (2011).

[27] A.A. Burkov and L. Balents, *Weyl Semimetal in a Topological Insulator Multilayer*, Phys. Rev. Lett. **107**, 127205 (2011).

[28] L. Lu, Z. Wang, D. Ye, L. Ran, L. Fu, J.D. Joannopoulos, and M. Soljačić, *Experimental observation of Weyl points*, Science **349**, 622 (2015).

[29] S.-Y. Xu, I. Belopolski, N. Alidoust, M. Neupane, G. Bian, C. Zhang, R. Sankar, G. Chang, Z. Yuan, C.-C. Lee, S.-M. Huang, H. Zheng, J. Ma, D.S. Sanchez, B.K. Wang, A. Bansil, F. Chou, P.P. Shibayev, H. Lin, S. Jia, and M.Z. Hasan, *Discovery of a Weyl fermion semimetal and topological Fermi arcs*, Science **349**, 613 (2015).

[30] B.-Q. Lv, H.-M. Weng, B.-B. Fu, X.-P. Wang, H. Miao, J. Ma, P. Richard, X.-C. Huang, L.-X. Zhao, G.-F. Chen, Z. Fang, X. Dai, T. Qian, and H. Ding, *Experimental Discovery of Weyl Semimetal TaAs*, Phys. Rev. X **5**, 031013 (2015).

[31] H. Weyl, *Elektron und Gravitation. I*, Zeitschrif für Physik **56**, 330 (1929).

[32] I. Affleck, T. Kennedy, E. H. Lieb, and H. Tasaki, *Rigorous results on valence-bond ground states in antiferromagnets*, Phys. Rev. Lett. **59**, 799 (1987).

[33] A. Y. Kitaev, *Unpaired Majorana fermions in quantum wires*, Phys.-Usp. **44**, 131 (2001).

[34] R. S. K. Mong and V. Shivamoggi, *Edge states and the bulk-boundary correspondence in Dirac Hamiltonians*, Phys. Rev. B **83**, 125109 (2011).

[35] S.-Q. Shen, W.-Y. Shan, and H.-Z. Lu, *Topological insulator and the Dirac equation*, SPIN **1**, 33 (2011).

[36] M. König, H. Buhmann, L. W. Molenkamp, T. Hughes, C.-X. Liu, X.-L. Qi, and S.-C. Zhang, *The Quantum Spin Hall Effect: Theory and Experiment*, J. Phys. Soc. Jpn. **77**, 031007 (2008).

[37] B. Zhou, H.-Z. Lu, R.-L. Chu, S.-Q. Shen, and Q. Niu, *Finite Size Effects on Helical Edge States in a Quantum Spin-Hall System*, Phys. Rev. Lett. **101**, 246807 (2008).

[38] S. Mao, Y. Kuramoto, K.-I. Imura, and A. Yamakage, *Analytic Theory of Edge Modes in Topological Insulators*, J. Phys. Soc. Jpn. **79**, 124709 (2010).

[39] C.-X. Liu, X.-L. Qi, and S.-C. Zhang, *Half quantum spin Hall effect on the surface of weak topological insulators*, Physica E **44**, 906 (2012).

[40] T. Ojanen, *Helical Fermi arcs and surface states in time-reversal invariant Weyl semimetals*, Phys. Rev. B **87**, 245112 (2013).

[41] Y. Hatsugai, *Chern number and edge states in the integer quantum Hall effect*, Phys. Rev. Lett. **71**, 3697 (1993).

[42] C. Tauber and P. Delplace, *Topological edge states in two-gap unitary systems: a transfer matrix approach*, New. J. Phys. **17**, 115008 (2015).

[43] V. Dwivedi and V. Chua, *Of bulk and boundaries: Generalized transfer matrices for tight-binding models*, Phys. Rev. B **93**, 134304 (2016).

[44] L. Balents, *Spin liquids in frustrated magnets*, Nature **464**, 199 (2010).

[45] A. Mielke, *Ferromagnetic ground states for the Hubbard model on line graphs*, J. Phys. **A 24**, L73 (1991); A. Mielke, *Ferromagnetism in the Hubbard model on line graphs and further considerations*, J. Phys. **A 24**, 3311 (1991); A. Mielke, *Exact ground states for the Hubbard model on the Kagome lattice*, J. Phys. **A 25**, 4335 (1992).

[46] H. Tasaki, *Ferromagnetism in the Hubbard models with degenerate single-electron ground states*, Phys. Rev. Lett. **69**, 1608 (1992).

[47] A. Mielke and H. Tasaki, *Ferromagnetism in the Hubbard model*, Commun. Math. Phys. **158**, 341 (1993).

[48] C. Zeng and V. Elser, *Numerical studies of antiferromagnetism on a Kagomé net*, Phys. Rev. B **42**, 8436 (1990).

[49] H. Asakawa and M. Suzuki, *Possibility of a sublattice order of the kagomé antiferromagnet*, Physica A **250**, 687 (1994).

[50] J. Schulenburg, A. Honecker, J. Schnack, J. Richter, and H.-J. Schmidt, *Macroscopic magnetization jumps due to independent magnons in frustrated quantum spin lattices*, Phys. Rev. Lett. **88**, 167207 (2002).

[51] J. Schnack, H.-J. Schmidt, J. Richter, and J. Schulenburg, *Independent magnon states on magnetic polytopes*, Eur. Phys. J. B **24**, 475 (2001).

[52] O. Derzhko, J. Richter, and M. Maksymenko, *Strongly correlated flat-band systems: The route from Heisenberg spins to Hubbard electrons*, Intern. Journal of Mod. Phys. B **29**, 1530007 (2015).

[53] Z. Gulácsi, A. Kampf, and D. Vollhardt, *Route to Ferromagnetism in Organic Polymers*, Phys. Rev. Lett. **105**, 266403 (2010).

[54] S.D. Huber and E. Altman, *Bose condensation in flat bands*, Phys. Rev. B **82**, 184502 (2010).

[55] N. Goldman, D.F. Urban, and D. Bercioux, *Topological phases for fermionic cold atoms on the Lieb lattice*, Phys. Rev. A **83**, 063601 (2011).

[56] S. Flach, D. Leykam, J.D. Bodyfelt, P. Matthies, and A.S. Desyatnikov, *Erratum: Detangling flat bands into Fano lattices*, Europhys. Lett. **106**, 19901 (2014).

[57] J.D. Bodyfelt, D. Leykam, C. Danieli, X. Yu, and S. Flach, *Flatbands under Correlated Perturbations*, Phys. Rev. Lett. **113**, 236403 (2014).

[58] D. L. Bergman, C. Wu, and L. Balents, *Band touching from real-space topology in frustrated hopping models*, Phys. Rev. B **78**, 125104 (2008).

[59] F. Baboux, L. Ge, T. Jacqmin, M. Biondi, E. Galopin, A. Lemaître, L. Le Gratiet, I. Sagnes, S. Schmidt, H.E. Türeci, A. Amo, and J. Bloch, *Bosonic Condensation and Disorder-Induced Localization in a Flat Band*, Phys. Rev. Lett. **116**, 066402 (2016).

[60] S. Mukherjee, A. Spracklen, D. Choudhury, N. Goldman, P. Öhberg, E. Andersson, and R.R. Thomson, *Observation of a Localized Flat-Band State in a Photonic Lieb Lattice*, Phys. Rev. Lett. **114**, 245504 (2015).

[61] D. Tong, *Lectures on the Quantum Hall Effect*, arXiv: 1606.06687v2 (2016).

[62] M. S. Hasan and C. L. Kane, *Colloquium: Topological insulators*, Rev. Mod. Phys. **82**, 3045 (2010).

[63] E. Witten, *Three lectures on topological phases of matter*, La Rivista del Nuovo Cimento **39**, 313 (2016).

[64] P. Hosur and X. Qi, *Recent developments in transport phenomena in Weyl semimetals*, C. R. Physique **14**, 857 (2013).

[65] C.L. Kane, *Topological Band Theory and the $\mathbb{Z}_2$ Invariant*, in *Topological Insulators*, edited by M. Franz and L. Molenkamp, pp. 3-34, Elsevier, (2013).

[66] A. Bansil, H. Lin, and T. Das, *Colloquium: Topological Band Theory*, Rev. Mod. Phys. **88**, 021004 (2016).

[67] “The Nobel Prize in Physics 1985”, Nobelprize.org. Nobel Media AB 2014. Web. 8 Jul 2017. `<https://www.nobelprize.org/nobel_prizes/physics/laureates/1985/>`

[68] “The Nobel Prize in Physics 1998”, Nobelprize.org. Nobel Media AB 2014. Web. 17 Nov 2017. `<https://www.nobelprize.org/nobel_prizes/physics/laureates/1998/>`

[69] “The Nobel Prize in Physics 2016”, Nobelprize.org. Nobel Media AB 2014. Web. 8 Jul 2017. `<https://www.nobelprize.org/nobel_prizes/physics/laureates/2016/>`

[70] J.K. Jain, *Composite fermions*, (Cambridge University Press, New York, 2007).

[71] P.W. Anderson, *Absence of Diffusion in Certain Random Lattices*, Phys. Rev. **109**, 1492 (1958).

[72] E. Abrahams, P.W. Anderson, D.C. Licciardello, and T. V. Ramakrishnan, *Scaling Theory of Localization: Absence of Quantum Diffusion in Two Dimensions*, Phys. Rev. Lett. **42**, 673 (1979).

[73] R.B. Laughlin, *Quantized Hall conductivity in two dimensions*, Phys. Rev. B **23**, 5632(R) (1981).

[74] B.I. Halperin, *Quantized Hall conductance, current-carrying edge states, and the existence of extended states in a two-dimensional disordered potential*, Phys. Rev. B **25**, 2185 (1982).

[75] T. Ando, *Theory of quantum transport in a two-dimensional electron system under magnetic fields. III. Many-Site Approximation*, J. Phys. Soc. Jpn. **37**, 622 (1974).

[76] D.J. Thouless, M. Kohmoto, M.P. Nightingale, and M. den Nijs, *Quantized Hall Conductance in a Two-Dimensional Periodic Potential*, Phys. Rev. Lett. **49**, 405 (1982).

[77] M.V. Berry, *Quantal Phase Factors Accompanying Adiabatic Changes*, Proc. R. Soc. London, Ser. A **392**, 45 (1984).

[78] D.J. Thouless, *Wannier functions for magnetic sub-bands*, J. Phys. C **17**, L325 (1984).

[79] H.A. Kramers, Proc. Amsterdam Acad. 33, 959 (1930).

[80] L. Fu and C.L. Kane, *Topological insulators with inversion symmetry*, Phys. Rev. B **76**, 045302 (2007).

[81] P.A.M Dirac, *The Quantum Theory of the Electron*, Proc. R. Soc. A **117**, 610 (1928).

[82] A.H. Castro Neto, F. Guinea, N.M.R. Peres, K.S. Novoselov, and A.K. Geim, *The electronic properties of graphene*, Rev. Mod. Phys. **81**, 109 (2009).

[83] E.J. Bergholtz, Z. Liu, M. Trescher, R. Moessner, and M. Udagawa, *Topology and Interactions in a Frustrated Slab: Tuning from Weyl Semimetals to $\mathcal{C} > 1$ Fractional Chern Insulators*, Phys. Rev. Lett. **114**, 016806 (2015).

[84] C. Beenakker, *Tipping the Weyl cone*, J. Club for Cond. Mat. Phys. August (2015).

[85] M. Trescher, B. Sbierski, P.W. Brouwer, and E.J. Bergholtz, *Quantum transport in Dirac materials: Signatures of tilted and anisotropic Dirac and Weyl cones*, Phys. Rev. B **91**, 115135 (2015).

[86] A.A. Soluyanov, D. Gresch, Z. Wang, Q. Wu, M. Troyer, X. Dai, and B.A. Bernevig, *Type-II Weyl semimetals*, Nature **527**, 495 (2015).

[87] M.N. Ali, J. Xiong, S. Flynn, J. Tao, Q.D. Gibson, L.M. Schoop, T. Liang, N. Haldolaarachchige, M. Hirschberger, N.P. Ong, and R.J. Cava, *Large, non-saturating magnetoresistance in* WTe_2, Nature **514**, 205 (2014).

[88] N. Kumar, Y. Sun, N. Xu, K. Manna, M. Yao, V. Suess, I. Leermakers, O. Young, T. Foerster, M. Schmidt, B. Yan, U. Zeitler, M. Shi, C. Felser, and C. Shekhar, *Extremely high magnetoresistance and conductivity in the type-II Weyl semimetals* WP_2 *and* MoP_2, arXiv:1703.04527 (2017).

[89] H.B. Nielsen and M. Ninomiya, *A no-go theorem for regularizing chiral fermions*, Phys. Lett. B **105**, 219 (1981).

[90] D. Friedan, *A proof of the Nielsen-Ninomiya theorem*, Commun. Math. Phys. **85**, 481 (1982).

[91] M. Udagawa, and E.J. Bergholtz, *Field-Selective Anomaly and Chiral Mode Reversal in Type-II Weyl Materials*, Phys. Rev. Lett. **117**, 086401 (2016).

[92] S.M. Young, S. Zaheer, J.C.Y. Teo, C.L. Kane, E.J. Mele, and A.M. Rappe, *Dirac Semimetal in Three Dimensions*, Phys. Rev. Lett. **108**, 140405 (2012).

[93] Z. Wang, Y. Sun, X.-Q. Chen, C. Franchini, G. Xu, H. Weng, X. Dai, and Z. Fang, *Dirac semimetal and topological phase transitions in* $\mathbf{A}_3Bi$ *(A = Na, K, Rb)*, Phys. Rev. B **85**, 195320 (2012).

[94] Z. Wang, H. Weng, Q. Wu, X. Dai, and Z. Fang, *Three-dimensional Dirac semimetal and quantum transport in* Cd_3As_2, Phys. Rev. B **88**, 125427 (2013).

[95] Z. K. Liu, B. Zhou, Y. Zhang, Z. J. Wang, H. M. Weng, D. Prabhakaran, S.-K. Mo, Z. X. Shen, Z. Fang, X. Dai, Z. Hussain, and Y. L. Chen, *Discovery of a Three-Dimensional Topological Dirac Semimetal,* Na_3Bi, Science **343**, 864 (2014).

[96] Z. K. Liu, J. Jiang, B. Zhou, Z. J. Wang, Y. Zhang, H. M. Weng, D. Prabhakaran, S-K. Mo, H. Peng, P. Dudin, T. Kim, M. Hoesch, Z. Fang, X. Dai, Z. X. Shen, D. L. Feng, Z. Hussain, and Y. L. Chen, *A stable three-dimensional topological Dirac semimetal* Cd_3As_2, Nature Mat. **13**, 677 (2014).

[97] B. Keimer, S.A. Kivelson, M.R. Norman, S. Uchida, and J. Zaanen, *From quantum matter to high-temperature superconductivity in copper oxides*, Nature **518**, 179 (2015).

[98] A.P. Schnyder, P.M.R. Brydon, D. Manske, and C. Timm, *Andreev spectroscopy and surface density of states for a three-dimensional time-reversal-invariant topological superconductor*, Phys. Rev. B **82**, 184508 (2010).

[99] D. H. Lee and J. D. Joannopoulos, *Simple scheme for surface-band calculations*, Phys. Rev. B **23**, 4988 (1981).

[100] Y.-C. Chang and J.N. Schulman, *Complex band structures of crystalline solids: An eigenvalue method*, Phys. Rev. B **25**, 3975 (1982).

[101] M. Trescher and E.J. Bergholtz, *Flat bands with higher Chern number in pyrochlore slabs*, Phys. Rev. B **86**, 241111(R) (2012).

[102] E.J. Bergholtz, Z. Liu, M. Trescher, R. Moessner, and M. Udagawa, *Topology and Interactions in a Frustrated Slab: Tuning from Weyl Semimetals to* $C > 1$ *Fractional Chern Insulators*, Phys. Rev. Lett. **114**, 016806 (2015).

[103] W.A. Benalcazar, B.A. Bernevig, and T.L. Hughes, *Quantized electric multipole insulators*, Science **357**, 61 (2017).

[104] J. Langbehn, Y. Peng, L. Trifunovic, F. von Oppen, P.W. Brouwer, *Reflection symmetric second-order topological insulators and superconductors*, arXiv:1708.03640 (2017).

[105] M. Lin and T. Hughes, *Topological Quadrupolar Semimetals*, arXiv:1708.08457 (2017).

[106] Z. Song, Z. Fang, and C. Fang, $(d?2)$-*dimensional edge states of rotation symmetry protected topological states*, arXiv:1708.02952.

[107] W.A. Benalcazar, B.A. Bernevig, T.L. Hughes, *Electric Multipole Moments, Topological Multipole Moment Pumping, and Chiral Hinge States in Crystalline Insulators*, arXiv:1708.04230 (2017).

[108] F. Schindler, A.M. Cook, M.G. Vergniory, Z. Wang, S.S.P. Parkin, B.A. Bernevig, and T. Neupert, *Higher-Order Topological Insulators*, arXiv:1708.03636.

[109] M. Ezawa, *Higher-order topological insulators and semimetals on the breathing Kagome and pyrochlore lattices*, arXiv: 1709.08425 (2017).

Accompanying Paper

PHYSICAL REVIEW B **96**, 085443 (2017)

Anatomy of topological surface states: Exact solutions from destructive interference on frustrated lattices

Flore K. Kunst,[1,2,*] Maximilian Trescher,[2] and Emil J. Bergholtz[1,2,†]
[1]*Department of Physics, Stockholm University, AlbaNova University Center, 106 91 Stockholm, Sweden*
[2]*Dahlem Center for Complex Quantum Systems and Insitut für Theoretische Physik, Freie Universität Berlin, Arnimallee 14, 14195 Berlin, Germany*

(Received 31 March 2017; published 30 August 2017)

The hallmark of topological phases is their robust boundary signature whose intriguing properties—such as the one-way transport on the chiral edge of a Chern insulator and the sudden disappearance of surface states forming open Fermi arcs on the surfaces of Weyl semimetals—are impossible to realize on the surface alone. Yet, despite the glaring simplicity of noninteracting topological bulk Hamiltonians and their concomitant energy spectrum, the detailed study of the corresponding surface states has essentially been restricted to numerical simulation. In this work, however, we show that exact analytical solutions of both topological and trivial surface states can be obtained for generic tight-binding models on a large class of geometrically frustrated lattices in any dimension without the need for fine-tuning of hopping amplitudes. Our solutions derive from local constraints tantamount to destructive interference between neighboring layer lattices perpendicular to the surface and provide microscopic insights into the structure of the surface states that enable analytical calculation of many desired properties including correlation functions, surface dispersion, Berry curvature, and the system size dependent gap closing, which necessarily occurs when the spatial localization switches surface. This further provides a deepened understanding of the bulk-boundary correspondence. We illustrate our general findings on a large number of examples in two and three spatial dimensions. Notably, we derive exact chiral Chern insulator edge states on the spin-orbit-coupled kagome lattice, and Fermi arcs relevant for recently synthesized slabs of pyrochlore-based $Eu_2Ir_2O_7$ and $Nd_2Ir_2O_7$, which realize an all-in-all-out spin configuration, as well as for spin-ice-like two-in-two-out and one-in-three-out configurations, which are both relevant for $Pr_2Ir_2O_7$. Remarkably, each of the pyrochlore examples exhibit clearly resolved Fermi arcs although only the one-in-three-out configuration features bulk Weyl nodes in realistic parameter regimes. Our approach generalizes to symmetry protected phases, e.g., quantum spin Hall systems and Dirac semimetals with time-reversal symmetry, and can furthermore signal the absence of topological surface states, which we illustrate for a class of models akin to the trivial surface of Hourglass materials KHgX where the exact solutions apply but, independently of Hamiltonian details, yield eigenstates delocalized over the entire sample.

DOI: 10.1103/PhysRevB.96.085443

I. INTRODUCTION

The experimental discovery of the quantum Hall effect in 1980 [1] decisively put topological phases in the limelight, and especially during the past decade the interplay between theoretical ideas and experimental advances has led to spectacular developments with intriguing prospects for future technological applications [2–5]. Most early work focused on topological insulators [2,3], the most basic of which are simple two-dimensional lattice generalizations of the quantum Hall states, namely Chern insulators [6–10], while quantum spin Hall insulators stem from two time-reversed copies thereof [11,12]. Weyl semimetals, experimentally realized in 2015 [13–16], are paradigmatic examples of a gapless topological phase existing in three dimensions [17–20], whose time-reversal invariant cousins, the Dirac semimetals, were unraveled in 2014 [21,22].

What makes these topological phases so intriguing is their robust and novel boundary states. Despite their central importance, and the simplicity of their bulk description, explicit solutions for the boundary states of topological phases are only known in a very limited number of special cases [23–31]. While powerful transfer matrix methods, which in some special cases allow analytical progress, have been developed [32–34], there is a glaring absence of generic analytical solutions that do not require fine-tuning, that are valid in any dimension, in the entire surface Brillouin zone, at finite size, and without the need for approximations.

In this work, we devise a general strategy for finding exact surface state solutions for trivial as well as for topological phases in any dimension, notably including Chern insulators and Weyl semimetals as well as their time-reversal invariant counter parts in quantum spin Hall insulators and Dirac semimetals. Rather than stemming from fine-tuning of hopping amplitudes our method is rooted in the underlying lattice structure. The lattices we consider can be seen as composed by $(d-1)$-dimensional layers of different variety, referred to as A and B lattices, that are stacked on top of each other in an alternating fashion such that the full d-dimensional lattice is geometrically frustrated (Fig. 1). Prominent examples of this type are kagome lattices in $d=2$ and pyrochlore in $d=3$.

Frustrated lattices are usually studied in the context of magnetism and lead to rich physics while being notoriously difficult to understand even at a qualitative level [35]. In glaring contrast, we find that frustration greatly simplifies the study of surface states of both trivial and topological variety. Under

---

[*] flore.kunst@fysik.su.se

[†] emil.bergholtz@fysik.su.se

©2017 American Physical Society

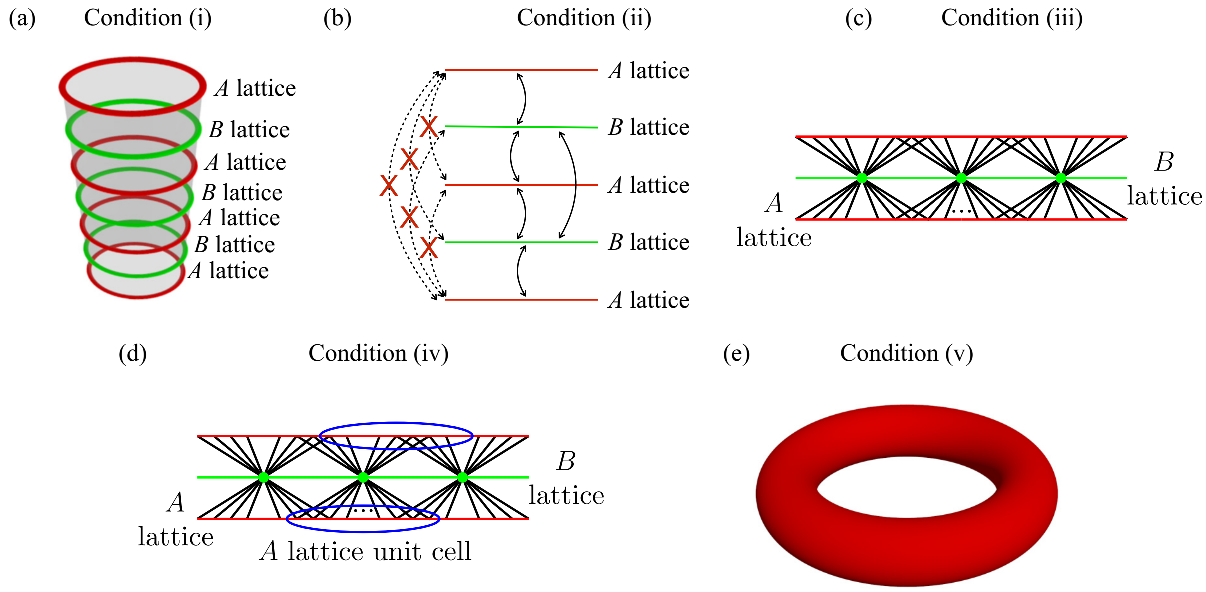

FIG. 1. Schematic figures to illustrate conditions (i)–(v). (a) The periodic, $(d-1)$-dimensional A and B lattices are shown in red and green, respectively. They are stacked such that condition (i) is fulfilled. (b) Schematic figure of which hoppings between the A and B lattices are allowed to fulfill condition (ii). Allowed hoppings are shown with arrows, and forbidden hoppings are indicated by crossed-out, dashed arrows. (c) The A and B lattices are shown in red and green, respectively, and the black lines indicate the hoppings between them. The lattices are coupled in a geometrically frustrated fashion, condition (iii). (d) Schematic figure of the frustrated lattice models with the minimal unit cell of the A lattice indicated by a blue ellipse. The unit cell is chosen to be the same for each A lattice. The hopping constraint to the intermediate site involves a nontrivial connection between unit cells fulfilling condition (iv). (e) Condition (v) states that the bulk Hamiltonian must support a topological phase, here symbolized by a torus.

very general conditions, we find exact eigenstates of the form

$$|\Psi(\mathbf{k})\rangle = \mathcal{N}(\mathbf{k}) \bigoplus_{m=1}^{N} (r(\mathbf{k}))^m |\Phi(\mathbf{k})\rangle_m, \qquad (1)$$

where $\mathbf{k}$ is the $(d-1)$-dimensional quasimomentum parallel to the surface, $|\Phi(\mathbf{k})\rangle_m$ is a Bloch state of the mth A lattice layer in a system composed of N such layers and $N-1$ intermediate B lattice layers, and $r(\mathbf{k})$ is a simple function determined by the local connectivity between neighboring layers and the Bloch states of the individual A layers. A salient feature of (1) is the vanishing amplitudes on the B lattice layers, which is directly related to how the exact solutions are found: assuming vanishing amplitudes on the B lattices puts constraints on $r(\mathbf{k})$ and provides a bootstrapping procedure uniquely leading to (1). The existence of these solutions hinges only on the counting of local constraints in combination with locality and translation invariance, and as such is insensitive to Hamiltonian details. In this context we stress that the local constraints are not a feature of the Hamiltonian but rather an emergent exact property of the eigenstates in Eq. (1), which is, however, not fulfilled for any other eigenstate. It is also noticeable that the exact solutions are for the full tight-binding model and thus extend in the full $(d-1)$-dimensional surface Brillouin zone and thereby also describe the attachment to bulk bands as the states switch surface. Moreover, the solutions remain exact at any finite size, i.e., for any number of layers, N.

Our approach is akin to the construction of flat band models arising due to local constraints on "line graphs" such as kagome and pyrochlore lattices (see, e.g., Ref. [36]). In contrast to our setup, these models require precise fine-tuning of the hopping amplitudes, typically allowing real and strictly nearest-neighbor hopping only. A second key difference is that the flat bands studied earlier are d-dimensional bulk bands while our solutions provide a $(d-1)$-dimensional manifold corresponding to the surface Brillouin zone. A similarity is, however, that band touchings necessarily occur in both setups.

Expanding on the seminal work by Mielke [37], a large body of work, including effects of interactions and disorder on line graphs, has accumulated during the past 25 years. In this context, valuable insights have been obtained for antiferromagnetic Heisenberg models on frustrated lattices with a flat band corresponding to a localized magnons [38–41] as well as on flat-band Hubbard models [42,43]. Alongside the extensive literature on theory (see also Refs. [37,44–49]), intriguing recent experiments [50,51] have underscored the value of these works.

It is conceivable that a similar progress on topological (and trivial) surface states can be spurred by the present work. Indeed, earlier work by two of us exploring Eq. (1) in the special case of $\{111\}$-oriented slabs of the pyrochlore lattice [52,53] has already borne fruit: for thin slabs this provided a natural platform for nearly flat bands with higher Chern numbers [53] and led to the subsequent discovery of an entire zoo of novel fractional Chern insulators qualitatively different from their quantum Hall relatives [52,54,55]. For thicker slabs, we discovered that Fermi arcs can in fact persist without Weyl nodes in the bulk—and that when Weyl nodes do occur their dispersion is generally both anisotropic and tilted [52,56]. In particular, the tilting can easily be so strong that the Weyl cones become "over-tilted" forming a compensated metal where the Weyl point is a singular point connecting two Fermi pockets [52]. These systems were later popularly coined type-II Weyl semimetals [57] and subsequently experimentally identified in a growing list of intriguing materials [58–65]. The phenomenon of Fermi arcs without the presence of Weyl nodes has been corroborated by recent experimental findings [66,67].

Building on our previous work, we here explore the connection between frustration and surface topology in much more detail and generality whereby we derive a number of generic results regarding correlation functions, surface dispersion, Berry curvature, energy gaps, and the bulk-boundary correspondence. While we mostly focus on two- and three-dimensional examples our results apply *mutatis mutandis* to any dimension. We also refine the earlier analysis of pyrochlore slabs to relate more directly to experiments on pyrochlore iridates. In particular, this makes contact to beautiful recent experimental progress in growing (thin) single-crystal slabs of the pyrochlore iridates $Eu_2Ir_2O_7$ [68] and $Nd_2Ir_2O_7$ [69]—two materials that both exhibit an all-in-all-out spin ordering and that we conclude are likely to have Fermi-arc-like surface states without possessing Weyl nodes in the bulk. For the yet to be grown slabs of $Pr_2Ir_2O_7$, we, however, find that Weyl nodes exist depending on the particular spin ordering [70], which is either spin-ice-like two-in-two-out and one-in-three-out, while Fermi arcs exist in either configuration.

This work is structured as follows. In Sec. II, we introduce a generic recipe for constructing our models and present the exact solutions and consequences thereof in general terms. In Sec. III, we illustrate the effectiveness of our recipe with a number of examples. In Sec. III A, we introduce a one-dimensional chain, and analyze the exact expressions for its end modes. In Sec. III B, we focus on two dimensions and derive exact edge state solutions on the kagome lattice including the chiral edge states occurring when the system is a Chern insulator. We also discuss the connection between the local lattice structure and topology. In Secs. III C–III E, we investigate the surface states of three-dimensional lattice models, most saliently obtaining exact solutions for the Fermi arcs of Weyl semimetals. Throughout this exposition, we comment on the relevance of our solutions for naturally existing, synthesized and artificial materials. We conclude with a discussion in Sec. IV.

II. SETUP AND GENERAL CONSIDERATIONS

In this section, we introduce five conditions—illustrated in Fig. 1 and detailed below—which, when they are fulfilled, allow us to find a $(d-1)$-dimensional manifold of exact wave functions and energies corresponding to the topological surface theory of a given d-dimensional topological phase. After detailing the general setup, we describe a number of results that can be derived directly from the exact surface state solutions.

A. Lattice structure

We study d-dimensional models with periodic boundary conditions in $(d-1)$ dimensions while they are left open in the remaining dimension giving the possibility of surface state solutions. More precisely, we consider models that can be decomposed in terms of alternating layers of two different $(d-1)$-dimensional periodic lattices; a lattice with n degrees of freedom (A lattice) and a lattice with n' degrees of freedom (B lattice) such that the surfaces of the material are formed by A lattices as shown schematically in Fig. 1(a), which we refer to as condition (i). In this work, for the sake of transparency, we mostly consider examples in which the degrees of freedom equal the number of sites in the unit A lattice cells, there is one available state per site. Note, however, that our results can readily be generalized to include more degrees of freedom which is necessary for instance for time-reversal symmetric models including onsite spin degrees of freedom.

The key assumption is that the A lattices are only connected to each other via the intermediate B lattices, and hence that direct hopping between different A lattices is prohibited as shown in Fig. 1(b). We refer to this as condition (ii). This is a realistic scenario, because it is unlikely that the orbitals of electrons sitting on different A lattices will overlap. Upon solving the Schrödinger equation, we find precisely n exact solutions to the wave function, which have total-zero weight on the intermediate-lattice sites if the layers are connected such that the full model is geometrically frustrated, condition (iii), as shown schematically in Fig. 1(c). This is due to geometric frustration, which allows the hoppings from the A lattices to the intermediate B lattice to interfere out. We refer to this interference as the local hopping constraint, and wave functions obeying this constraint can always be found when the lattice satisfies conditions (ii) and (iii). This shows that the connection of the A lattices via the intermediate B lattices is essential for our problem. Hopping within the A and within the B lattices is allowed and will be elaborated upon in the next section.

We distinguish two types of connectivity in this stacking construction. In the first, the intermediate sites on the B lattice are connected to sites in the minimal unit cells on both neighboring A lattices in a symmetric way. In the second case, the intermediate sites on the B lattice are connected differently to the sites in the minimal unit cells of the A lattice below than to the sites in the unit cells in the A lattice above, as shown in the bottom panel of Fig. 1(d). In either case, there is a natural constraint—zero total hopping amplitude to the B lattice sites—that leads to a bootstrapping procedure and exact eigenstates that can be expressed entirely in terms of the Bloch eigenstates of the A lattice layers. In the symmetric case, the solutions are rather mundane with $|r(\mathbf{k})| = 1$, while the latter case, where the local constraint necessarily connects multiple minimal unit cells, gives more interesting solutions for $r(\mathbf{k})$ including those that correspond to topological surface states. The latter situation is referred to as condition (iv). Note that in this discussion we have assumed that the coupling strength between the intermediate B lattice and the degrees of freedom in the unit cell of the A lattice above and equals the coupling strength between the intermediate B lattice and the degrees of freedom in the unit cell of the A lattice below. We refer to this as the isotropic case. If this coupling were anisotropic, we can find nontrivial solutions for $|r(\mathbf{k})|$, which depend on both the crystal momentum $\mathbf{k}$ and the strength of the various perpendicular hopping parameters, regardless of whether the local constraint involves multiple unit cells. If we now include pertinent terms in the Hamiltonian such that the system indeed supports a topological phase, as shown in Fig. 1(e), we find that our wave-function solutions describe a topological boundary state. This final condition is referred to as condition (v).

We can thus list five conditions that need to be fulfilled to find topological boundary states.

(i) The lattices are formed by alternating $(d-1)$-dimensional lattices, referred to as A and B lattices, which have periodic boundary conditions. There are open boundary conditions in the direction of stacking and the outermost layers are A lattices [Fig. 1(a)].

(ii) The A lattices are only coupled to each other via intermediate B lattices and cannot directly communicate [Fig. 1(b)].

(iii) The A and B lattices are connected in a geometrically frustrated fashion meaning that there are several inequivalent ways of hopping from the neighboring A lattices to the single orbital in the B lattice unit cell leading, together with (ii), to the emergence of a local constraint obeyed by the exact solutions in Eq. (1) [Fig. 1(c)]. (In the presence of pertinent symmetries, this can be generalized to several orbitals in the B lattice unit cell.)

(iv) There is no way of choosing a minimal unit cell such that the local constraint obeyed by the exact solutions in Eq. (1) takes place within a single unit cell on both of the involved A lattices [Fig. 1(d)]. Alternatively, this condition can be satisfied if the coupling between the A and B lattices is anisotropic.

(v) The bulk Hamiltonian supports the pertinent topological phase [Fig. 1(e)].

Exact wave-function solutions corresponding to n $(d-1)$-dimensional bands can be found whenever conditions (i)–(iii) are fulfilled. Fulfilling condition (iv), the exact solution generically yields exponentially localized boundary states, and whenever the bulk supports a given topological phase, condition (v), the exact solution corresponds to its surface theory.

B. Generic tight-binding models

We consider tight-binding models describing noninteracting identical particles on the lattices described above. For the sake of clarity we set $n'=1$, i.e., we consider intermediate B lattices with a single degree of freedom per unit cell. The Hamiltonian describing a system with N stacked A lattices is written directly in momentum space and reads $H^N(\mathbf{k}) = \Psi^\dagger(\mathbf{k})\mathcal{H}^N_{\mathbf{k}}\Psi(\mathbf{k})$ with $\Psi(\mathbf{k}) = \bigoplus_{s=1}^{l}\psi_s(\mathbf{k})$, $l \equiv (n+1)N-1$, the annihilation operator of an electron in the full lattice, and $\mathcal{H}^N_{\mathbf{k}}$ an $((n+1)N-1)\times((n+1)N-1)$-dimensional matrix given by

$$\mathcal{H}^N_{\mathbf{k}} = \begin{pmatrix} \mathcal{H}_{\mathbf{k}} & \mathcal{H}^A_\perp & 0 & 0 & 0 & 0 & 0 \\ \mathcal{H}^{\dagger,A}_\perp & h_{\mathbf{k}} & \mathcal{H}^{\dagger,B}_\perp & 0 & 0 & 0 & 0 \\ 0 & \mathcal{H}^B_\perp & \mathcal{H}_{\mathbf{k}} & \mathcal{H}^A_\perp & 0 & 0 & 0 \\ 0 & 0 & \mathcal{H}^{\dagger,A}_\perp & h_{\mathbf{k}} & \mathcal{H}^{\dagger,B}_\perp & 0 & 0 \\ 0 & 0 & 0 & \mathcal{H}^B_\perp & \mathcal{H}_{\mathbf{k}} & \dots & 0 \\ 0 & 0 & 0 & 0 & \vdots & \ddots & \mathcal{H}^{\dagger,B}_\perp \\ 0 & 0 & 0 & 0 & 0 & \mathcal{H}^B_\perp & \mathcal{H}_{\mathbf{k}} \end{pmatrix}, \tag{2}$$

where $\mathcal{H}_{\mathbf{k}}$ is the $(n\times n)$-dimensional Hamiltonian for the A lattice, $h_{\mathbf{k}}$ is the (1×1)-dimensional Hamiltonian for the intermediate B lattice, and $\mathcal{H}^\alpha_\perp$ is an $(n\times 1)$ matrix connecting the A lattice to the intermediate B lattice. In general, this connecting Hamiltonian can be written as

$$\mathcal{H}^\alpha_\perp = \bigoplus_{s=1}^{n} t_{\perp,\alpha,s}\, f_{\alpha,s}(\mathbf{k}), \tag{3}$$

where $t_{\perp,\alpha,s}$ is the hopping amplitude from site s in the unit cell of the A lattice to the intermediate B lattice, and $f_{\alpha,s}(\mathbf{k})$ is a $\mathbf{k}$-dependent phase derived from the local lattice structure. Note that all hopping amplitudes are allowed to be complex, i.e., allowing for spin-orbit coupling as well as commensurate magnetic fields incorporated via Peierls substitution.

C. Exact eigenstates

Using the Hamiltonian in Eq. (2), we find a subset of solutions to the Schrödinger equation, $\mathcal{H}^N_{\mathbf{k}}|\Psi_i(\mathbf{k})\rangle = E^N_i(\mathbf{k})|\Psi_i(\mathbf{k})\rangle$, $i=1,2,\dots,n$, corresponding to the number of degrees of freedom in the A lattice, given by

$$E^N_i(\mathbf{k}) = E_i(\mathbf{k}), \tag{4}$$

$$|\Psi_i(\mathbf{k})\rangle = \mathcal{N}_i(\mathbf{k})\bigoplus_{m=1}^{N}(r_i(\mathbf{k}))^m|\Phi_i(\mathbf{k})\rangle_m, \tag{5}$$

where $E_i(\mathbf{k})$ are the eigenvalues of the A lattice Hamiltonian $\mathcal{H}_{\mathbf{k}}$ and $\Phi_i(\mathbf{k})$ the eigenstates with components $\phi_{i,s}(\mathbf{k})$, $s=1,\dots,n$, thereof, $\mathbf{k}$ is the $(d-1)$-dimensional momentum,

$$\mathcal{N}_i(\mathbf{k}) = \frac{1}{|r_i(\mathbf{k})|}\sqrt{\frac{|r_i(\mathbf{k})|^2-1}{(|r_i(\mathbf{k})|^2)^N-1}}, \tag{6}$$

ensures normalization,[1] m labels the A lattice layer, and $r_i(\mathbf{k})$ is a prefactor given by

$$r_i(\mathbf{k}) = -\frac{\psi_{i,m,s}(\mathbf{k})}{\psi_{i,m+1,s}(\mathbf{k})}, \quad \forall s\in\{1\cdots n\}, \quad m\in\{1\cdots N-1\}, \tag{7}$$

where $\psi_{i,m,s}$ are the components of $\Psi_i(\mathbf{k})$ in the mth A lattice on sublattice site s. Using that the weight of the wave function on the intermediate site of the B lattice is zero, $r_i(\mathbf{k})$ can also be expressed in terms of the components of $\Phi_i(\mathbf{k})$:

$$r_i(\mathbf{k}) = -\frac{\mathcal{H}^{\dagger,A}_\perp\Phi_i(\mathbf{k})}{\mathcal{H}^{\dagger,B}_\perp\Phi_i(\mathbf{k})} = -\frac{\sum_{s=1}^{n} t_{\perp,A,s}f^\dagger_{A,s}(\mathbf{k})\phi_{i,s}(\mathbf{k})}{\sum_{s=1}^{n} t_{\perp,B,s}f^\dagger_{B,s}(\mathbf{k})\phi_{i,s}(\mathbf{k})}, \tag{8}$$

where $f_{\alpha,s}(\mathbf{k})$ is given in Eq. (3). From this equation, we can formalize condition (iv): this condition is fulfilled when $|r_i(\mathbf{k})|\neq 1$, i.e., $t_{\perp,A,s}f_{A,s}\neq t_{\perp,B,s}f_{B,s}$, and broken when $|r_i(\mathbf{k})|=1$, i.e., $t_{\perp,A,s}f_{A,s}=t_{\perp,B,s}f_{B,s}$. Note that explicitly calculating $|r_i(\mathbf{k})|$, one can still find $|r_i(\mathbf{k})|=1$ when $t_{\perp,A,s}f_{A,s}\neq t_{\perp,B,s}f_{B,s}$. This is due to the explicit form of $\phi_{i,s}(\mathbf{k})$ and closely related to topology in the model, condition

---

[1] As $|r(\mathbf{k})|\to 1$, the normalization factor is smooth approaching $\mathcal{N}(\mathbf{k}) = 1/\sqrt{N}$.

(v), which is further discussed towards the end of this section. We want to emphasize that the exact solution is completely independent of the Hamiltonian $h_{\mathbf{k}}$ on the intermediate B lattice. It should, however, be mentioned that the remaining $((n+1)N-(n+1))$ solutions to the Schrödinger equation, which are only numerically accessible, do depend on this Hamiltonian and are subject to deformation by changing the perpendicular hopping strength.

Inspecting the solution in Eq. (5), we notice three properties. First, the solution has zero weight on the intermediate sites, which means that the Hamiltonian $h_{\mathbf{k}}$ for the intermediate B lattice is completely irrelevant to the solution and as such can generally include arbitrary terms. Second, only the connectivity of the A lattices via the intermediate B lattices encoded by $t_{\perp,\alpha,s} f_{\alpha,s}(\mathbf{k})$ is relevant. The coupling between A lattices may differ in strength effectively yielding strongly or weakly coupled layers. Third, we can now understand why satisfying condition (iv) leads to boundary states. If $|r_i(\mathbf{k})| = 1$, the weight of the wave function on layer m,

$$P_{i,m}(\mathbf{k}) = |\mathcal{N}_i(\mathbf{k})|^2 |r_i(\mathbf{k})|^{2m}, \tag{9}$$

is the same for all m, and the wave function is equally localized on each A lattice. However, if $|r_i(\mathbf{k})| \neq 1$, the eigenstate will localize to one of the boundaries. If $|r_i(\mathbf{k})| < 1$, $P_{i,m}(\mathbf{k})$ decreases with increasing m and the wave function is strongly localized on the first layer $m = 1$ corresponding to the surface on one side. When $|r_i(\mathbf{k})| > 1$, $P_{i,m}(\mathbf{k})$ increases with increasing m and the state is localized on the last layer $m = N$ corresponding to the surface on the other side. Therefore, when $|r_i(\mathbf{k})| \neq 1$, we have exponentially localized boundary states with a localization length, and the solution in Eq. (5) thus corresponds to the solution for the boundary state. Now, if $|r_i(\mathbf{k})|$ also has a $\mathbf{k}$-dependent structure the boundary state can switch surfaces, which for a three-dimensional material means a constant energy contour represents a Fermi arc. When discussing the exponential surface localization we will make use of the localization length $\xi_i(\mathbf{k}) = (\ln |r_i(\mathbf{k})|)^{-1}$.

Satisfying condition (iv) means we have found a suitable geometry for the lattices to find boundary states. However, when one plugs the solution to the eigenfunctions into Eq. (8), we may still find $|r_i(\mathbf{k})| = 1$ for systems deep in the topologically trivial regime. In the trivial regime, it is also possible to find unprotected, weakly-localized boundary states for which $|r_i(\mathbf{k})|$ has a nontrivial structure. Therefore we need to impose a fifth condition, condition (v), that introduces nontrivial topology in the models such that we for instance obtain a Chern insulator and Weyl semimetal, which are examples of two- and three-dimensional models, respectively. One needs to minimally break time-reversal symmetry to find a Chern insulator, such that in two dimensions, the Hamiltonian should include at least one such term. To obtain a Weyl semimetal, one could either break inversion or time-reversal symmetry. In the cases studied in this work, we break the latter symmetry by turning the A lattice into a Chern insulator. In Sec. II E, we present an argument to understand why this leads to an eigenstate that switches surfaces.

It is worth emphasizing that the exact wave-function solution directly enables the computation of correlation functions within the surface bands which are otherwise only numerically or approximately tractable. For example, the expectation value of any operator $\mathcal{A}$, which acts the same within each layer, reads $\langle \mathcal{A} \rangle = |\mathcal{N}(\mathbf{k})|^2 \sum_{m=1}^{N} |r_i(\mathbf{k})|^{2m} \langle \Phi_i(\mathbf{k}) | \mathcal{A} | \Phi_i(\mathbf{k}) \rangle$. This expression can readily be extended to more complicated, layer dependent, operators.

Diagonalizing the Hamiltonian in Eq. (2) leads to the band spectrum of the full system with $((n+1)N-1)$ bands, which are divided into $(n+1)$-bulk parts separated by band gaps. When conditions (i)–(v) are met, boundary states are present, which can be identified in the bulk spectrum as bands crossing a gap and connecting two bulk parts.

It should be noted that, while the exact solutions remain unchanged, all other eigenstates change while deforming the coupling to the B lattices. For instance, as we will demonstrate in Sec. III, increasing the interlayer coupling strength drives a transition between the quasi-two-dimensional layered Chern insulators phase and a truly three-dimensional Weyl semimetal regime.

D. Attachment of bulk bands and surface switching

It is a generic property of our exact solutions that in part of the surface Brillouin zone they attach to bulk bands in the limit of many stacked layers. This happens precisely at those points $\mathbf{q}$ in the $(d-1)$-dimensional (surface) Brillouin zone where the boundary state connects to the bulk where $|r(\mathbf{q})| = 1$, i.e., where the penetration depth ξ diverges. Below we will provide a variational argument that shows that the gap—either from below or from above—vanishes as N^{-2} for large N. In contrast, whenever the penetration is finite there is a gap to neighboring bands also in the limit $N \to \infty$.

There are two types of penetration depth divergences and concomitant bulk band attachments. First, at $\mathbf{q} = 0$, it immediately follows that $|r(\mathbf{q} = \mathbf{0})| = 1$ independently of model details. Second, many models feature $(d-2)$-dimensional families of such $\mathbf{q}$ points, typically along high symmetry paths cutting through the surface Brillouin zone. The existence of these motifs depend on details of the lattice geometry and the tight-binding Hamiltonian. In particular, the boundary states may switch surfaces at $\mathbf{q}$, i.e., $\mathrm{sign}[\ln|r_i(\mathbf{q}-\epsilon\mathbf{k})|] \neq \mathrm{sign}[\ln|r_i(\mathbf{q}+\epsilon\mathbf{k})|]$ as $\epsilon \to 0$. Notably, $(d-2)$-dimensional families of such $\mathbf{q}$ points necessarily exist for topologically nontrivial models although they can also occur in topologically trivial models.

It is intuitively plausible that the energy gap between the boundary states and the bulk bands at the points $\mathbf{q}$ should disappear. We can explicitly demonstrate that this is indeed the case by introducing a class of ansatz wave functions describing bulk state with nearly the same energy as the exact solution $|r(\mathbf{q})| = 1$. In this case, the exact solution to the low-energy boundary state can be written as

$$|\psi(\mathbf{q})\rangle = \frac{1}{\sqrt{N}} \bigoplus_{m=1}^{N} \mathrm{e}^{i\alpha(\mathbf{q})m} |\phi(\mathbf{q})\rangle_m. \tag{10}$$

We can now make an ansatz for a class of states expected to be close in energy,

$$|\chi^0(\mathbf{q})\rangle = \frac{1}{\sqrt{N}} \bigoplus_{m=1}^{N} \mathrm{e}^{i\tilde{\alpha}(\mathbf{q})m} |\phi(\mathbf{q})\rangle_m, \tag{11}$$

which has to be orthogonal to the exact solution in Eq. (10), such that we find

$$\alpha(\mathbf{q}) - \tilde{\alpha}(\mathbf{q}) = \frac{2\pi}{N} p, \quad p = 1,2,\ldots,N-1. \tag{12}$$

This leads to

$$e^{i\tilde{\alpha}(\mathbf{q})m} = e^{i(\alpha(\mathbf{q})-2\pi p/N)m}. \tag{13}$$

However, the trial wave function in Eq. (11) is not an eigenfunction of the Hamiltonian because it has zero weight on the intermediate site of the B lattice, which it should not have.

Therefore the trial wave function can be made an eigenstate by mixing in the state for the intermediate site $|\tilde{\chi}(\mathbf{q})\rangle$, which results in altering the entries given in $|\phi(\mathbf{q})\rangle$, such that we can create an approximate eigenstate, which becomes exact in the limit of large N:

$$|\chi(\mathbf{q})\rangle = \frac{1}{\sqrt{N}} \bigoplus_{m=1}^{N} e^{i\tilde{\alpha}(\mathbf{q})m} |\phi(\mathbf{q})\rangle_m + \frac{1}{\sqrt{N}} \bigoplus_{m=1}^{N} a_m |\tilde{\chi}(\mathbf{q})\rangle_m, \tag{14}$$

where

$$a_m \sim -\frac{t_\perp p}{N}. \tag{15}$$

Therefore we find that the energy difference between the two states behaves as

$$\Delta \sim -\frac{t_\perp^2 p^2 + \mathcal{O}(t_\perp^4)}{N^2} \tag{16}$$

for large N. Therefore the energy difference between the exact solution and our variational bulk state disappears as N^{-2} at $\mathbf{k} = \mathbf{q}$ for large N. In fact, there will be many such states as signaled by the family of states constructed (varying p). Note, however, that depending on details, in particular the strength of the interlayer tunneling $t_\perp$, the variational state may be lower or higher in energy. For weak $t_\perp$, the variational state is always lower in energy than the exact solution. However, for stronger $t_\perp$, this can change in the Brillouin zone, as is strikingly manifested in the case of Weyl points at which these energies are equal and a sign change of Δ takes place.

E. Berry curvature and surface state topology

The appearance of boundary states is closely related to nontrivial topology in the bulk of a material. For Chern insulators and Weyl semimetals, this bulk topology is manifested by a nonzero Chern number. The Chern number for an isolated band $|\rho_s(\mathbf{k})\rangle$ of a two-dimensional periodic lattice is computed by integrating the Berry curvature over the Brillouin zone:

$$C_s = \frac{1}{2\pi} \int_{BZ} \mathcal{F}_{xy,s}(\mathbf{k})\, d^2k, \tag{17}$$

where $\mathcal{F}_{ij,s}(\mathbf{k})$ is the Berry curvature given by $\mathcal{F}_{ij,s}(\mathbf{k}) = \partial_{k_i} A_{j,s}(\mathbf{k}) - \partial_{k_j} A_{i,s}(\mathbf{k})$ with $A_{j,s}(\mathbf{k}) = -i\langle \rho_s(\mathbf{k})|\partial_{k_j}|\rho_s(\mathbf{k})\rangle$ the Berry connection. The total Chern number of any system has to be zero, i.e., $\sum_s C_s = 0$. While correlation functions are easily calculated, the derivatives entering the Berry curvature complicate analytical calculations thereof. Alternatively, this problem can be seen from the fact that a (derivative-free) expression of the Berry curvature involves all energy eigenstates of the model—not just the solvable surface bands. Nevertheless, a number of instructive results can be derived.

For (quasi-)three-dimensional models, we use the solution to the surface state in Eq. (5) such that one can write the Berry curvature of a system with N two-dimensional A lattices as

$$\begin{aligned}\mathcal{F}_{N,xy,i} = {} & \mathcal{F}_{1,xy,i} - i\, F(N,r_i(\mathbf{k}))\big\{\big[\partial_{k_x} r_i^*(\mathbf{k})\big]\big[\partial_{k_y} r_i(\mathbf{k})\big] \\ & - \big[\partial_{k_y} r_i^*(\mathbf{k})\big]\big[\partial_{k_x} r_i(\mathbf{k})\big]\big\},\end{aligned} \tag{18}$$

with

$$\begin{aligned}\mathcal{F}_{1,xy,i} = {} & -i\big[\big(\partial_{k_x}\langle \Phi_i(\mathbf{k})|\big)\partial_{k_y}|\Phi_i(\mathbf{k})\rangle \\ & - \big(\partial_{k_y}\langle \Phi_i(\mathbf{k})|\big)\partial_{k_x}|\Phi_i(\mathbf{k})\rangle\big],\end{aligned}$$

being the Berry curvature of a single A layer and

$$\begin{aligned}F(N,r_i(\mathbf{k})) \equiv {} & (1-|r_i(\mathbf{k})|^2)^{-2} \\ & - N^2|r_i(\mathbf{k})|^{2N-2}(1-|r_i(\mathbf{k})|^{2N})^{-2}.\end{aligned} \tag{19}$$

We emphasize that $F(N,r_i(\mathbf{k}))$ contains the full N-dependence of the Berry curvature in Eq. (18). In the limit $|r_i(\mathbf{k})| \to 1$, Eq. (19) reduces to $(N^2-1)/12$, thus for large N the Berry curvature exhibits a peak scaling with N^2 at those parts in the Brillouin zone where the exact solution is not a surface state but is completely delocalized over all layers. In contrast, whenever $|r_i(\mathbf{k})| \neq 1$, the Berry curvature saturates as a function of N consistent with the exponential localization of the wave functions to the surface layers.

The Chern number $C_{N,i}$ of the solvable bands in a system with N A lattices can be found upon integrating the Berry curvature in Eq. (18) over the Brillouin zone as shown in Eq. (17). When $|r_i(\mathbf{k})| = 1$ everywhere, the derivative over the second part of Eq. (18) yields zero such that the total Chern number equals that of one layer $C_{1,i}$. However, in the generic situation when $|r_i(\mathbf{k})| \neq 1$, we observe in our examples that the total Chern number grows with N as

$$C_{N,i,|r|\neq 1} = N\, C_{1,i}, \tag{20}$$

which means that the Chern number that is associated with each A lattice is absorbed into the surface state.

Furthermore, it can be shown that a finite Chern number on the A lattice implies Fermi arcs by considering a generic two-band model on the A lattice whose Hamiltonian reads

$$\mathcal{H}_{\mathbf{k}} = d(\mathbf{k}) \cdot \boldsymbol{\sigma} + d_0(\mathbf{k})\sigma_{\mathbf{0}}, \tag{21}$$

where $\boldsymbol{\sigma}$ are the Pauli matrices, $\sigma_0 = \mathbb{I}_{2\times 2}$, and

$$\mathcal{P}_\pm(\mathbf{k}) = \tfrac{1}{2}(\sigma_0 \pm \hat{\mathbf{d}}(\mathbf{k}) \cdot \sigma), \tag{22}$$

projects on to the upper (+) and lower (−) bands, respectively, with $\hat{\mathbf{d}}(\mathbf{k}) = \mathbf{d}(\mathbf{k})/|\mathbf{d}(\mathbf{k})|$. Using the projector, the Chern number can be written in terms of $\hat{\mathbf{d}}(\mathbf{k})$ as

$$C = \frac{1}{4\pi} \int dk_x \int dk_y\, \hat{\mathbf{d}}(\mathbf{k}) \cdot \left(\frac{\partial \hat{\mathbf{d}}(\mathbf{k})}{\partial k_x} \times \frac{\partial \hat{\mathbf{d}}(\mathbf{k})}{\partial k_y} \right). \tag{23}$$

The Chern number can thus be interpreted as the number of times $\hat{\mathbf{d}}(\mathbf{k})$ wraps the unit sphere. Provided the general structure of $r_i(\mathbf{k})$ one can show that, for a very generic class of models, this implies that $\hat{\mathbf{d}}(\mathbf{k})$ renders both the numerator and denominator of $r_i(\mathbf{k})$ given in Eq. (8) to vanish at *different* $\mathbf{k}$

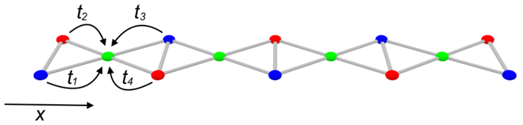

FIG. 2. The chain model featuring a two-band model (red and blue sites) stacked on top of each other with a single (green) site in between.

whenever the single layer Chern number is finite. Thus $r_i(\mathbf{k})$ has zeros and infinities when the A lattice is a Chern insulator implying surface switching and the existence of Fermi arcs in the sense that the surface state is entirely localized at the top and bottom layer at different points in the surface Brillouin zone. An explicit example of this is provided in Sec. III C.

III. EXAMPLES

A. One dimension: end modes on a chain

As a simple warmup, we start by studying a one-dimensional system, which has two degrees of freedom in the A lattice and one degree of freedom in the intermediate B lattice shown in Fig. 2. This chain readily satisfies conditions (i)–(iii), and the absence of a surface momentum parameter means that condition (iv) can only be satisfied if the A and intermediate B lattices are coupled in an anisotropic fashion.

In its most generic form, the Hamiltonian for each A lattice reads $H = \Phi^\dagger \mathcal{H}^{1\mathrm{D}} \Phi$, where Φ is the annihilation operator of an electron in the A lattice and $\mathcal{H}^{1\mathrm{D}}$ can be written in the Dirac form

$$\mathcal{H}^{1\mathrm{D}} = \mathbf{d} \cdot \boldsymbol{\sigma} + d_0 \sigma_0, \tag{24}$$

with the energy eigenvalues

$$E_\pm = \pm |\mathbf{d}| + d_0, \tag{25}$$

and eigenstates $|\Phi_\pm\rangle$. Due to the lack of a momentum parameter, the eigenvalues and the amplitudes of the eigenstates are constants. The Hamiltonian for the one-dimensional chain is given in Eqs. (2) and (3) with the phases $f_{\alpha,s} = 1\,\forall\,\alpha, s$, and we set the intermediate B lattice Hamiltonian $h = 0$ and $t_{\perp,A,s} = t_s$, and $t_{\perp,B,s} = t_{s+2}$ with $t_{\perp,\alpha,s} \in \mathbb{R}\,\forall\,\alpha, s$. Using Eq. (8), we find

$$r_\pm(t_s) = -\frac{t_1\phi_{\pm,1} + t_2\phi_{\pm,2}}{t_3\phi_{\pm,1} + t_4\phi_{\pm,2}}, \tag{26}$$

which is a function of t_s. When $t_1 = t_3$ and $t_2 = t_4$, $r_\pm = -1$ and according to Eq. (9) the wave function in Eq. (5) has equal weight on each A lattice m. However, when $t_1 \neq t_3$ and/or $t_2 \neq t_4$, we find $|r_\pm| \neq 1$ and there are end modes on the chain. These modes either reside at the same end, e.g., at $t_1 = 10\,t_3$ and $t_2 = 10\,t_4$ yields $r_\pm = -10$ hence both end modes are exponentially localized around the A lattice $m = N$—or they live at opposite ends, e.g., when the Hamiltonian for the A lattice in Eq. (24) reads $\mathbf{d} = (V, 0, 0)$ and we require the perpendicular hopping parameters to satisfy $t_1 + t_2 < t_3 + t_4$ and $t_1 - t_2 > t_3 - t_4$ yielding $|r_+| < 1$ and $|r_-| > 1$ such that the end modes Ψ_+ and Ψ_- appear at $m = 1$ and $m = N$, respectively. The exactly obtained end modes of the chain thus switch ends as a function of the perpendicular hopping parameters t_s.

B. Two dimensions: Chern and quantum spin Hall insulators on kagome and related lattices

In this section, we study two-dimensional lattice models by stacking (periodic) chains containing two sites in the lattice unit cell (red and blue in Fig. 3), which are connected via an intermediate chain with a single site per unit cell (green). The two types of chains are stacked in an alternating fashion in such a way that the lattice geometry is frustrated and a local hopping constraint is naturally realized, such that conditions (i)–(iii) are fulfilled. The four different stacking possibilities are shown in Fig. 3, where the lattices in Figs. 3(a) and 3(d) are related to the lattices in Figs. 3(c) and 3(b), respectively, via sublattice exchange in every other two-site chain.

The A lattice for the models in Figs. 3(a) and 3(d) are the two-site periodic chains in red and blue, and the intermediate B lattice is the one-site periodic chain in green. For the lattices in Figs. 3(b) and 3(c), however, one has to consider the composite of three chains as the A lattice indicated by the black brackets in the figures. The intermediate lattice is the one-site green

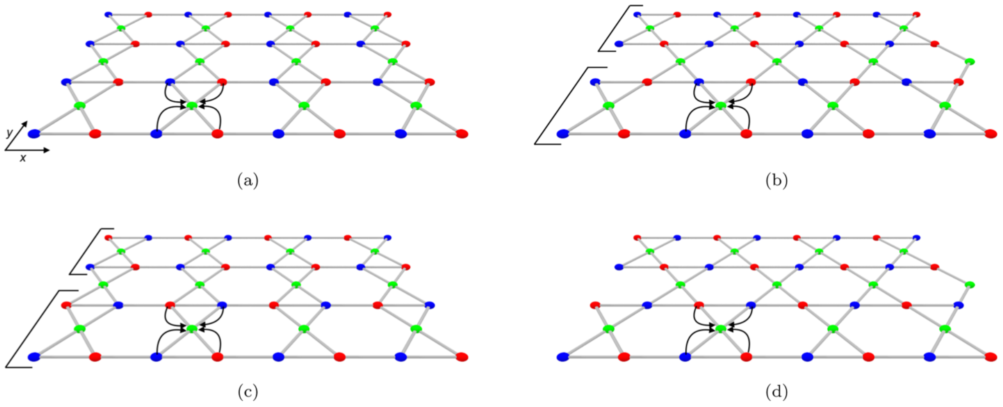

(a) (b) (c) (d)

FIG. 3. Four ways to stack two different chains, a chain with a two-site unit cell in red and blue and a chain with a one-site unit cell in green. If the models were fully periodic, the lattices in (a) and (d) would have three sites in the unit cell, whereas the lattices in (b) and (c) would contain six sites in the unit cell. In (a) and (d), the two-site chains correspond to the A lattices. In (b) and (c), the A lattices are formed by a composite of three chains as is indicated by the black brackets. The black arrows illustrate the hopping from the A lattice to the intermediate B lattice, which leads to a zero-total hopping amplitude to the intermediate (green) site.

chain in between. We treat all four models in detail and find a subset of solutions to the Schrödinger equation for each of them. First, we will show that when condition (iv) is not fulfilled, as is the case for the lattices in Figs. 3(a)–3(c), the system remains topologically trivial, signaled by an absence of edge states and vanishing topological invariants, regardless of the microscopic Hamiltonian (as long as it is local in the sense of condition (ii)). Then, by considering models living on the lattice displayed in Fig. 3(d), which does fulfill condition (iv), we illuminate the relevance of condition (v). Strikingly, we find that whenever the system has a bulk band characterized by a unit Chern number our exact solutions describe the chiral edge states of the model.

Let us now proceed to demonstrate what is advertised in the preceding paragraph by considering a generic description of translation invariant tight-binding models on the aforementioned lattices. The Hamiltonian for each chain with two sublattices in red and blue is $H(k_x) = \Phi^\dagger(k_x)\mathcal{H}^{\mathrm{ch}}_{k_x}\Phi(k_x)$, where Φ is the annihilation operator of an electron in the A lattice and

$$\mathcal{H}^{\mathrm{ch}}_{k_x} = \mathbf{d}(k_x)\cdot\boldsymbol{\sigma} + d_0(k_x)\sigma_0. \tag{27}$$

The corresponding energy eigenvalues are given by

$$E_\pm(k_x) = \pm|\mathbf{d}(k_x)| + d_0(k_x), \tag{28}$$

and $|\Phi_\pm(k_x)\rangle$ are the eigenstates. In all four cases, the Hamiltonian for the full models is given in Eqs. (2) and (3), and we set $h_{k_x} = 0$ and $t_{\perp,\alpha,s} = t_\perp \in \mathbb{R}\,\forall\,\alpha, s$. The latter can be interpreted as a gauge choice, and does not impede our general approach: one can always choose the perpendicular hopping parameter $t_\perp$ to be real by suitably redefining $H(k_x)$ to account for the “flux” through each closed path of the lattice [71].

We first focus on the model in Fig. 3(a). The A lattice Hamiltonian $\mathcal{H}_{k_x}$ is given by Eq. (27), and the pertinent phases are $f_{A,1}(k_x) = f_{B,1}(k_x) = \exp(-ik_x/4)$ and $f_{A,2}(k_x) = f_{B,2}(k_x) = \exp(ik_x/4)$ such that by using Eq. (8) we immediately find that $r_\pm(k_x) = -1$ and condition (iv) is thus not fulfilled. The weight of the wave function on each individual chain given in Eq. (9) is thus equal for each chain m, which labels the A lattice, meaning that the state is fully delocalized. We thus expect to find a topologically trivial system. Indeed, regardless of any details of $\mathbf{d}(k_x)$ for the A lattice Hamiltonian, the Chern number remains zero.

Next, we look at the system in Fig. 3(b). The suitably redefined A lattice Hamiltonian now accounts for the five sites in the unit cell, hence we can find exact expressions for five edge state bands. The A lattice Hamiltonian $\mathcal{H}_{k_x}$ is given by

$$\mathcal{H}_{k_x} = \left(\begin{array}{ccccc} \multicolumn{2}{c}{\mathcal{H}^{\mathrm{ch}}_{k_x}} & \begin{matrix} t_\perp \mathrm{e}^{-i\frac{k_x}{4}} \\ t_\perp \mathrm{e}^{i\frac{k_x}{4}} \end{matrix} & \multicolumn{2}{c}{0} \\ t_\perp \mathrm{e}^{i\frac{k_x}{4}} & t_\perp \mathrm{e}^{-i\frac{k_x}{4}} & h^{\mathrm{ch}}_{k_x} & t_\perp \mathrm{e}^{i\frac{k_x}{4}} & t_\perp \mathrm{e}^{-i\frac{k_x}{4}} \\ \multicolumn{2}{c}{0} & \begin{matrix} t_\perp \mathrm{e}^{-i\frac{k_x}{4}} \\ t_\perp \mathrm{e}^{i\frac{k_x}{4}} \end{matrix} & \multicolumn{2}{c}{\mathcal{H}^{\mathrm{ch}}_{k_x}} \end{array}\right),$$

and the concomitant phase factors are $f_{A,4}(k_x) = f_{B,1}(k_x) = \exp(ik_x/4)$, $f_{A,5}(k_x) = f_{B,2}(k_x) = \exp(-ik_x/4)$ and $f_{A,\alpha}(k_x) = 0, \alpha = 1,2,3$ and $f_{B,\alpha'}(k_x) = 0, \alpha' = 3,4,5$. Before analyzing the five solutions to the Schrödinger equation for the full system, we first take a closer look at the solution for the A lattice Hamiltonian $\mathcal{H}_{k_x}$. We observe that we can interpret the A lattice as existing out of two sub-A lattices, the two-site chains in red and blue, and a subintermediate B lattice, the green sites. We thus find $n_{\mathrm{sub}} = 2$ solutions of the following form, which look similar to the solution in Eq. (5):

$$|\Phi_\pm(k_x)\rangle \doteq \tilde{\mathcal{N}}_\pm(k_x)\begin{pmatrix} \phi_{\pm,1}(k_x) \\ \phi_{\pm,2}(k_x) \\ 0 \\ s_\pm(k_x)\phi_{\pm,1}(k_x) \\ s_\pm(k_x)\phi_{\pm,2}(k_x) \end{pmatrix}, \tag{29}$$

where $\tilde{\mathcal{N}}_\pm(k_x)$ is the normalization factor, $|\Phi_\pm(k_x)\rangle$ are the eigenstates of the two-site chain, and $s_\pm(k_x) = -1$, which can be straightforwardly derived. The corresponding eigenvalues are given in Eq. (28). Plugging this and the phases into Eq. (8) yields $r_\pm(k_x) = -1$ such that we retrieve a system in which the wave functions are completely delocalized. For the remaining three solutions, we find $\Phi_i(\mathbf{k}) = \bigoplus_{s=1}^5 \phi_{i,s}(\mathbf{k})$ with $i = 1,2,3$ with the energy E_i and again $r_i(k_x) = -1, \forall\, i$, independent of the Hamiltonian used for the chain. Again, regardless of the hopping terms included in the Hamiltonian, the system stays in a topologically trivial phase, as expected by the absence of edge states stemming from the breaking of condition (iv).

Now, we turn to the lattice model in Fig. 3(c), which shows slightly more complex behavior. The A lattice Hamiltonian again includes five sites in the unit cell and reads

$$\mathcal{H}_{k_x} = \left(\begin{array}{ccccc} \multicolumn{2}{c}{\mathcal{H}^{\mathrm{ch}}_{k_x}} & \begin{matrix} t_\perp \mathrm{e}^{-i\frac{k_x}{4}} \\ t_\perp \mathrm{e}^{i\frac{k_x}{4}} \end{matrix} & \multicolumn{2}{c}{0} \\ t_\perp \mathrm{e}^{i\frac{k_x}{4}} & t_\perp \mathrm{e}^{-i\frac{k_x}{4}} & h^{\mathrm{ch}}_{k_x} & t_\perp \mathrm{e}^{-i\frac{k_x}{4}} & t_\perp \mathrm{e}^{i\frac{k_x}{4}} \\ \multicolumn{2}{c}{0} & \begin{matrix} t_\perp \mathrm{e}^{i\frac{k_x}{4}} \\ t_\perp \mathrm{e}^{-i\frac{k_x}{4}} \end{matrix} & \multicolumn{2}{c}{\mathcal{H}^{\mathrm{ch}}_{k_x}} \end{array}\right).$$

The phases for the full model are $f_{A,4}(k_x) = f_{B,2}(k_x) = \exp(ik_x/4)$, $f_{A,5}(k_x) = f_{B,1}(k_x) = \exp(-ik_x/4)$ and $f_{A,\alpha}(k_x) = 0, \alpha = 1,2,3$ and $f_{B,\alpha'}(k_x) = 0, \alpha' = 3,4,5$. Similar to the model corresponding to Fig. 3(b), we find $n_{\mathrm{sub}} = 2$ wave-function solutions as given in Eq. (29) with

$$s_\pm(k_x) = -\frac{\mathrm{e}^{i\frac{k_x}{4}}\phi_{\pm,1}(k_x) + \mathrm{e}^{-i\frac{k_x}{4}}\phi_{\pm,2}(k_x)}{\mathrm{e}^{-i\frac{k_x}{4}}\phi_{\pm,1}(k_x) + \mathrm{e}^{i\frac{k_x}{4}}\phi_{\pm,2}(k_x)}, \tag{30}$$

such that

$$\begin{aligned} r_\pm(k_x) &= -\frac{\mathrm{e}^{-i\frac{k_x}{4}}s_\pm(k_x)\phi_{\pm,1}(k_x) + \mathrm{e}^{i\frac{k_x}{4}}s_\pm(k_x)\phi_{\pm,2}(k_x)}{\mathrm{e}^{i\frac{k_x}{4}}\phi_{\pm,1}(k_x) + \mathrm{e}^{-i\frac{k_x}{4}}\phi_{\pm,2}(k_x)} \\ &= -s_\pm(k_x)\, s_\pm^{-1}(k_x) = -1. \end{aligned}$$

These two wave functions are thus equally localized to each A lattice present in the full model. However, we notice that there may occur some localization inside the A lattice as $|s_\pm(k_x)|$ is not trivially equal to 1, which is shown in Figs. 4(a) and 4(b).

For the remaining three solutions to the wave function, which read $\Phi_i(\mathbf{k}) = \bigoplus_{s=1}^5 \phi_{i,s}(\mathbf{k})$ with $i = 1,2,3$, we find a nontrivial $|r_i(k_x)|$ as shown in Fig. 5(a). However, one can see in the corresponding energy spectrum in Fig. 5(b) that the localized states are not topologically protected, which is

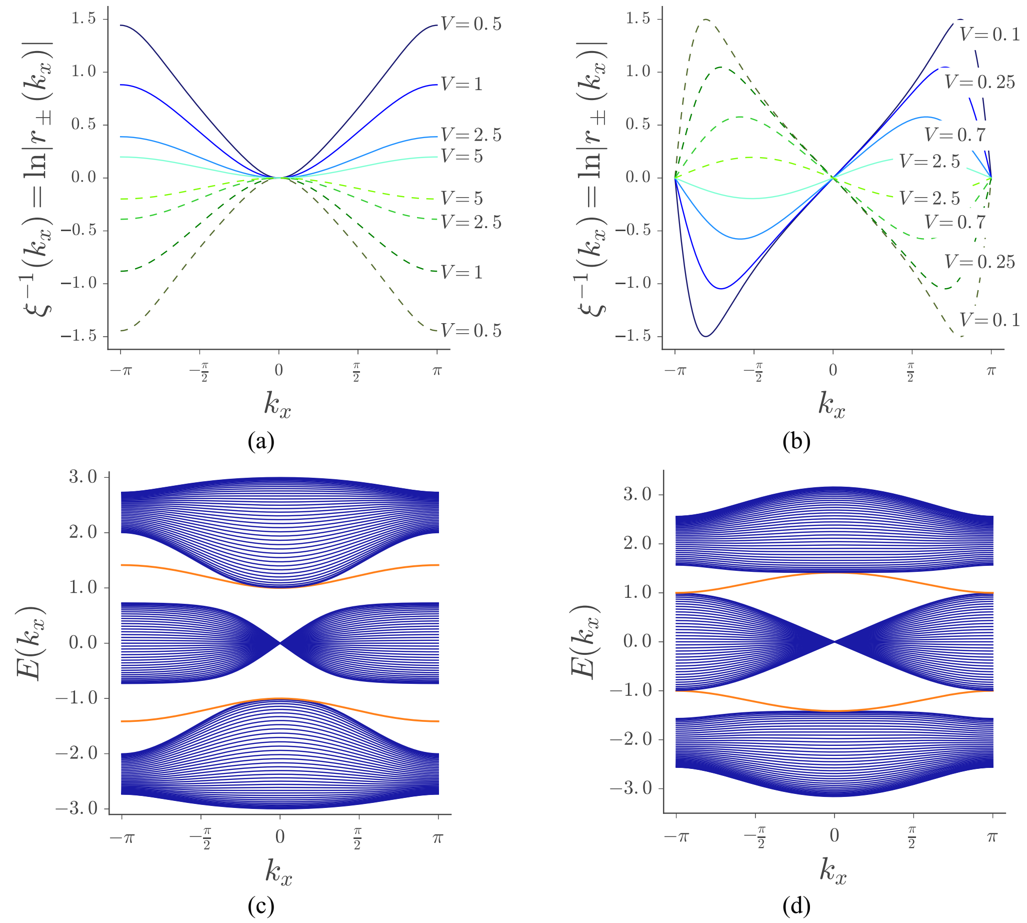

(a) (b)

(c) (d)

FIG. 4. Plots for the kagome model in Fig. 3(d) with the chain Hamiltonian given in Eqs. (27) and (31). (a) and (b) show the inverse localization length $\ln|r_\pm(k_x)|$ as given in Eq. (30). (c) and (d) show the energy spectrum with $N=40$ and the energy is plotted in units of t_1' and t', respectively. The blue and green lines in (a) and (b) correspond to the $+$ and $-$ solution of the wave function, respectively, and top and bottom orange lines in (c) and (d) depict the $+$ and $-$ energy solutions, respectively. (a) and (c) are plotted for $t/t_1'=t_1/t_1'=t'/t_1'=0$, $t_\perp/t_1'=1$, and varying values of V in units of t_1' in (a), and $V/t_1'=1$ in (c). (b) and (d) are plotted for $t/t'=t_1/t'=t_1'/t'=0$, $t_\perp/t'=1$, and varying values of V in units of t' in (b), and $V/t'=1$ in (d). (a) and (c) correspond to a topologically trivial system whereas (b) and (d) reveal that the system is a Chern insulator, where we find that the right movers are localized on the edge $m=1$ and the left movers on the edge $m=N$. (a) and (b) also correspond to $\ln|s_\pm(k_x)|$ for the A lattice of the model in Fig. 3(c) with $h^{\mathrm{ch}}_{k_x}=0$ and the other parameters as mentioned before.

supported by the retrieval of a zero-Chern number for these parameters.

Finally, we turn to the kagome lattice in Fig. 3(d), which shows significantly richer and more complex behavior. This lattice is also of special interest as it occurs naturally in many materials and can also be engineered in cold atom systems [72,73]. The A lattice Hamiltonian is given by Eq. (27), and the phases are $f_{A,1}(k_x)=f_{B,2}(k_x)=\exp(-ik_x/4)$ and $f_{A,2}(k_x)=f_{B,1}(k_x)=\exp(ik_x/4)$, such that $r_\pm(k_x)$ corresponds to the expression in Eq. (30), and constraint (iv) is fulfilled. This allows us to review condition (v). To specify the A lattice Hamiltonian in Eq. (27), we use the following:

$$\mathbf{d}(k_x)=\left(t\cos\frac{k_x}{2}+t_1\sin\frac{k_x}{2},\,t'\cos\frac{k_x}{2}+t_1'\sin\frac{k_x}{2},\,V\right),\qquad(31)$$

where t, t', t_1 and t_1' are nearest-neighbor hopping parameters, and V is a staggering potential, and $d_0(k_x)=0$. We emphasize that details of the lattice Hamiltonian are irrelevant as long as it is local and translation invariant, and we have introduced nearest-neighbor hopping terms only to be able to review the localization of the state in a transparent fashion. We find that $|r_\pm(k_x)|\neq 1$ only when at least $t_1'\neq 0$ and/or $t'\neq 0$ as is shown in Fig. 4. We first review the situation where $t_1'\neq 0$ and $t'=0$, in which case both sublattice and inversion symmetry are broken but time-reversal symmetry is preserved. We thus expect to be unable to find a Chern-insulator phase, which is indeed what is revealed in Figs. 4(a) and 4(c). The case in which $t_1'=0$ and $t'\neq 0$ is more interesting. Now inversion symmetry is preserved but sublattice and time-reversal symmetry are broken such that we are able to find a Chern insulator as is shown in Figs. 4(b) and 4(d). We see that the energy spectrum has two bulk gaps with a band crossing each of these gaps. These two bands (in orange) correspond to our exact wave-function solution in Eq. (5) and their inverse localization length $\ln|r_\pm(k_x)|$ reveals that the right mover localizes to the chain $m=1$ and the left mover to the chain $m=N$, which is in accordance with the chirality of the edge states in a Chern

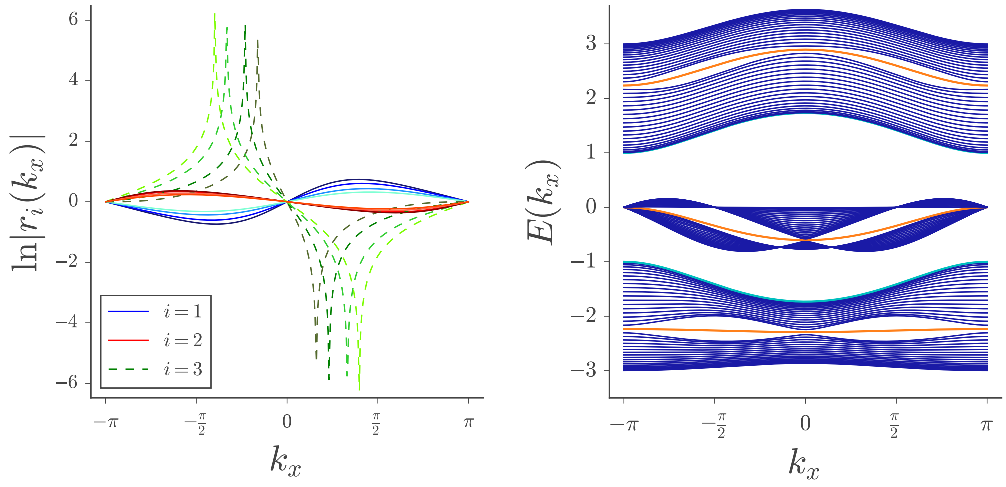

(a) (b)

FIG. 5. Plots for the model in Fig. 3(c) with the chain Hamiltonian given in Eqs. (27) with $d_0(k_x) = 0$ and $\mathbf{d}(k_x) = (t\cos\frac{k_x}{2}, t'\cos\frac{k_x}{2}, V)$ where t and t' are nearest-neighbor hopping parameters and V is a staggering potential, and $h^{\mathrm{ch}}_{k_x} = 0$. (a) Plot of the inverse localization length $\ln|r_i(k_x)|$ for $t'/t = t_\perp/t = 1$ and different values of $V/t = 0,1,2,3$ corresponding from dark to light, and where blue corresponds to $r_1(k_x)$, red to $r_2(k_x)$ and green to $r_3(k_x)$. (b) Energy spectrum with $N = 40$ shown in units of t with $V/t = 1$, where the orange bands indicate the energies $E_i(k_x)$ with the lowest one corresponding to $E_1(k_x)$, the middle to $E_2(k_x)$ and the top to $E_3(k_x)$. The two bands in cyan correspond to the energy solutions $E_-(k_x)$ and $E_+(k_x)$, respectively, corresponding to the wave-function solution in Eqs. (29) and (30). Even though, the inverse localization length shown in (a) indicates that the three solutions $|\Psi_i(k_x)\rangle$ localize, the band spectrum in (b) reveals that they are not topologically protected.

insulator. This localization is corroborated by the weight of the wave function on each A lattice m given in Eq. (9) shown in Fig. 6 for a system of five layers. The Chern number for the fully periodic kagome lattice is governed by the values of $V/t_\perp$, and we find for half-filling that the Chern number $C = 1$ for $|t_\perp/V| > 0.7$. This leads to another interesting observation, namely, that when the system is no longer a Chern insulator, the exact solution still localizes, which is reflected by $\ln|r_\pm(k_x)|$ in Fig. 4(b) still having a structure for $V/t' = 2.5, t_\perp/t' = 1$. We have thus found a Chern insulator on the kagome lattice with chiral-edge states whose exact wave-function solution is given in Eq. (5) when both time-reversal and sublattice symmetry are broken simultaneously. The breaking of the first is a minimal requirement to find a Chern insulator, whereas the breaking of the second is inherent to our specific choice of lattice as preserving sublattice symmetry would yield $|\phi_{\pm,1}(k_x)| = |\phi_{\pm,2}(k_x)|$ such that one trivially finds $|r_\pm(k_x)| = 1$. Note that a quantum spin Hall insulator can simply be retrieved by taking two time-reversed copies of the Chern insulator, which introduces spin degree of freedom. In that case, the system supports four helical-edge states, whose wave function is described by our exact solution.

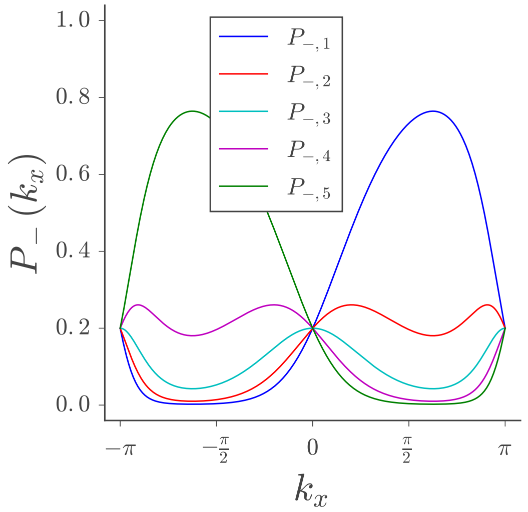

FIG. 6. Plot of the weight of the wave function $|\Psi_-(k_x)\rangle$ on each layer m shown in Eq. (9) for $N = 5$ for the model in Fig. 3(d) with the A-lattice Hamiltonian given in Eq. (31) with $t_\perp/t' = 1$ and $|t_\perp/V| = 2$ and all other parameters equal to zero. The wave functions are completely localized to layer m if the weight equals $P_{-,m}(k_x) = 1$. Blue is $P_{-,1}(k_x)$, red $P_{-,2}(k_x)$, cyan $P_{-,3}(k_x)$, magenta $P_{-,4}(k_x)$, and green $P_{-,5}(k_x)$. This plot is in perfect agreement with what is shown in Fig. 4(b).

C. Three dimensions, first example: Dirac and Weyl semimetals from stacked checkerboard models

We now turn to three-dimensional models built from stacking two-dimensional layers in a frustrated fashion. In the first example, the A lattice is a checkerboard lattice, which has two sites in the unit cell, and the intermediary B lattice is a square lattice with one site in the unit cell. By stacking them we obtain the lattice shown in Fig. 7, which is a three-dimensional cousin of the kagome model in Fig. 3(d). The two-dimensional surface Brillouin zone is shown as an inset in Fig. 8(d). Conditions (i)–(iv) are fulfilled and we have a Weyl phase when condition (v) is fulfilled in which case we expect that the exact solution corresponds to (a family of) Fermi arcs. In particular, this model is well suited for exploring

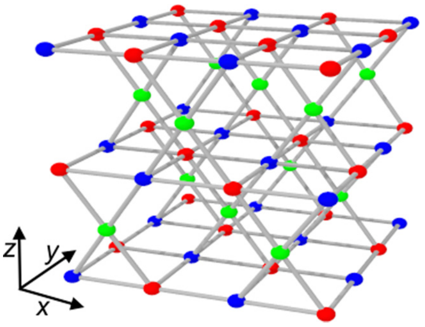

FIG. 7. The checkerboard model featuring checkerboard lattices (red and blue sites) stacked on top of each other with a square lattice (green) in between. Notice the relative displacement between checkerboard lattices.

the connection between the topology of the two-dimensional layers and the band switching properties of the surface bands.

The Hamiltonian for the individual checkerboard lattice is given by $H(\mathbf{k}) = \Phi^{\dagger}(\mathbf{k})\mathcal{H}_{\mathbf{k}}\Phi(\mathbf{k})$, where $\Phi(\mathbf{k})$ is the annihilation operator of an electron in the checkerboard layer and

$$\mathcal{H}_{\mathbf{k}} = \mathbf{d}(\mathbf{k}) \cdot \boldsymbol{\sigma} + d_0(\mathbf{k})\sigma_0. \tag{32}$$

The eigenvalues read

$$E_{\pm}(\mathbf{k}) = \pm|\mathbf{d}(\mathbf{k})| + d_0(\mathbf{k}). \tag{33}$$

The Hamiltonian for the full model is given in Eqs. (2) and (3) with $h_{\mathbf{k}} = 0$, $t_{\perp,s,\alpha} = t_{\perp} \in \mathbb{R}\,\forall\, s,\alpha$, and $f_{A,1}(k_x) = f_{B,2}(k_x) = \exp[-ik_x/2\sqrt{2}]$ and $f_{A,2}(k_x) = f_{B,1}(k_x) = \exp[ik_x/2\sqrt{2}]$. We find two exact solutions to the wave function, which are given in Eq. (5) with

$$r_{\pm}(\mathbf{k}) = -\frac{\mathrm{e}^{i\frac{k_x}{2\sqrt{2}}}\phi_{\pm,1}(\mathbf{k}) + \mathrm{e}^{-i\frac{k_x}{2\sqrt{2}}}\phi_{\pm,2}(\mathbf{k})}{\mathrm{e}^{-i\frac{k_x}{2\sqrt{2}}}\phi_{\pm,1}(\mathbf{k}) + \mathrm{e}^{i\frac{k_x}{2\sqrt{2}}}\phi_{\pm,2}(\mathbf{k})}. \tag{34}$$

It is trivial to see that $|r_{\pm}(\mathbf{k})| = 1$ when $k_x = 0$. In Sec. II E, we discussed that $r_i(\mathbf{k})$ must have zeros and infinities when the A lattice is a Chern insulator. For this specific model, this means that we need to solve

$$\mathrm{e}^{is\frac{k_x}{2\sqrt{2}}}\phi_{\pm,1}(\mathbf{k}) + \mathrm{e}^{-is\frac{k_x}{2\sqrt{2}}}\phi_{\pm,2}(\mathbf{k}) = 0, \tag{35}$$

with $s = 1$ $(s = -1)$ which corresponds to setting the numerator (denominator) in Eq. (34) to zero. Using the standard representation of the Pauli matrices, we have

$$|\Phi_{\pm}(\mathbf{k})\rangle \doteq \tilde{\mathcal{N}}_{\pm}(\mathbf{k})\begin{pmatrix} \pm|\mathbf{d}(\mathbf{k})| + d_z(\mathbf{k}) \\ d_x(\mathbf{k}) + i\,d_y(\mathbf{k}) \end{pmatrix}, \tag{36}$$

where $\tilde{\mathcal{N}}_{\pm}(\mathbf{k})$ is the normalization factor. The above requirement (35) thus decomposes into

$$\pm|\mathbf{d}(\mathbf{k})| + d_z(\mathbf{k}) + \cos\left(\frac{k_x}{\sqrt{2}}\right)d_x(\mathbf{k}) + s\sin\left(\frac{k_x}{\sqrt{2}}\right)d_y(\mathbf{k}) + i\left[\cos\left(\frac{k_x}{\sqrt{2}}\right)d_y(\mathbf{k}) - s\sin\left(\frac{k_x}{\sqrt{2}}\right)d_x(\mathbf{k})\right] = 0, \tag{37}$$

such that the real and imaginary part of this equation have to be zero simultaneously. When the Hamiltonian in Eq. (32) describes a Chern insulator, we know that $\mathbf{d}(\mathbf{k})$ points in every direction in the Brillouin zone, which means we can always satisfy Eq. (37) at, except in pathological cases, *different* $\mathbf{k}$, thus implying Fermi arc like surface bands. To be more specific, the Fermi arcs are formed as one-dimensional constant energy contours in the two-dimensional surface bands. In these two-dimensional bands, the argument above shows that there are momenta where the state is entirely localized at the topmost layer [diverging $r(\mathbf{k})$] and other points where it is identically localized to the bottom layer [$r(\mathbf{k}) = 0$]. It is also important to note that this is independent of the presence of Weyl nodes in the bulk as those only appear at sufficiently strong interlayer tunneling.

We will now proceed by considering a specific layered checkerboard model which supports a Weyl semimetal phase at strong interlayer coupling. The Hamiltonian of a single A layer, as specified in Eq. (32), is known to describe a Chern insulator when it has the following components

$$d_0(\mathbf{k}) = 0, \quad d_x(\mathbf{k}) = t\sin\left(\frac{k_x}{\sqrt{2}}\right), \quad d_y(\mathbf{k}) = t'\sin\left(\frac{k_y}{\sqrt{2}}\right),$$

$$d_z(\mathbf{k}) = V + t_2\left[\cos\left(\frac{k_x + k_y}{\sqrt{2}}\right) + \cos\left(\frac{k_x - k_y}{\sqrt{2}}\right)\right],$$

where t and t' are the nearest-neighbor hopping amplitudes, t_2 is the next-nearest-neighbor hopping amplitude, and V is the staggering potential. The single-layer system has $C = 1$ at half-filling for $t'/t = t_2/t = 1$ and $|V/t| \leqslant 2$ and $C = 0$ for $|V/t| > 2$. The solution of the inverse localization length $\xi^{-1}(\mathbf{k}) = \ln|r_{-}(\mathbf{k})|$ is shown in Fig. 8(a) for a set of parameters in which the checkerboard lattice features a Chern insulator, and they agree with the solutions to Eq. (37) explicitly mentioned in a footnote below.[2] We notice that $\xi^{-1}(\mathbf{k})$ respects the symmetry of the lattice model, which has a mirror symmetry along the line $y = 0$. The black line in the plot corresponds to the energy contour of the surface state $E_{-}(\mathbf{k})$ at the chemical potential $\mu/t = -0.9$. $\xi^{-1}(\mathbf{k})$ changes sign four times when we trace the equal-energy line of the surface state meaning that this state switches surfaces an equal number of times. The solution to the boundary state in Eq. (5) with $r_{\pm}(\mathbf{k})$ given in Eq. (34) thus describes a family of Fermi arcs, while a constant energy contour in the manifold of these solutions, as the one just described, describes a Fermi arc.

Moreover, we find numerically that the two-dimensional surface band carries a Chern number whose value corresponds

---

[2] We set $t'/t = t_2/t = V/t = 1$ such that they agree with the parameters used to plot the inverse localization length $\xi^{-1}(\mathbf{k}) = \ln|r_{-}(\mathbf{k})|$ in Fig. 8(a). The solutions for setting the numerator and denominator of $r_i(\mathbf{k})$ zero are the same for $i = +$ and $i = -$. The numerator, i.e., $s = 1$, is zero when $\mathbf{k} = (0,\pm\sqrt{2}\pi)$, $(\pm\sqrt{2}\pi,0)$, $(-\frac{\pi}{2\sqrt{2}},\frac{3\pi}{2\sqrt{2}})$, $(\frac{3\pi}{2\sqrt{2}},-\frac{\pi}{2\sqrt{2}})$, $(\pm\frac{\sqrt{2}}{\cos(\mp\sqrt{5/2})},\pm\frac{\sqrt{2}}{\cos(\pm1/\sqrt{10})})$, and for the denominator, $s = -1$, we find $\mathbf{k} = (0,\pm\sqrt{2}\pi)$, $(\pm\sqrt{2}\pi,0)$, $(-\frac{\pi}{2\sqrt{2}},-\frac{3\pi}{2\sqrt{2}})$, $(\frac{3\pi}{2\sqrt{2}},\frac{\pi}{2\sqrt{2}})$, $(\pm\frac{\sqrt{2}}{\cos(\mp\sqrt{5/2})},\pm\frac{\sqrt{2}}{\cos(\mp1/\sqrt{10})})$. Note that these solutions can easily be generalized for different values of the parameters. While some of the zeros are common for the nominator and denominator, we generically find that they also have distinct zeros as is also the case in the example given.

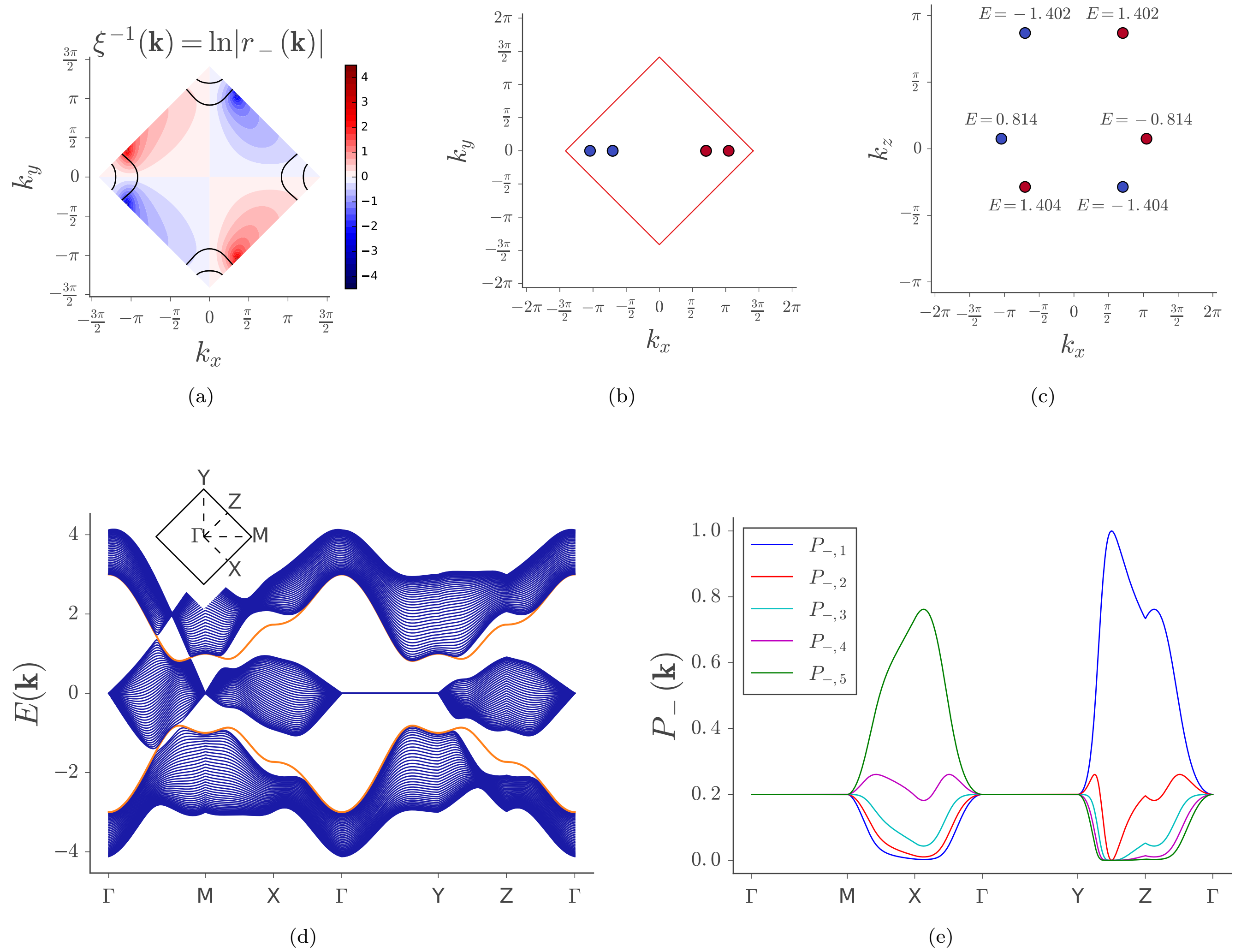

(a) (b) (c)

(d) (e)

FIG. 8. Solutions to the checkerboard model with nonzero Chern number with $t'/t = t_2/t = t_\perp/t = V/t = 1$. In (a), we show the inverse localization length $\xi^{-1}(\mathbf{k}) = \ln|r_-(\mathbf{k})|$ given in Eq. (34). The black line is the energy contour of $E_-(\mathbf{k})$ at the chemical potential $\mu/t = -0.9$. We see that the boundary state switches surfaces four times and is thus a Fermi arc. In (b) and (c), the location of the Weyl nodes in the three-dimensional Brillouin zone is shown from the top view in the k_z direction in (b) and a two-dimensional cut at $k_y = 0$ in (c). Red and blue correspond to positive and negative Berry charge, respectively. The energies corresponding to the Weyl nodes are included as insets in (c). The energy spectrum along a path in the Brillouin zone, indicated in the inset, is shown in (d) with $N = 40$ and the energy given in units of t. The orange bands correspond to the Fermi arc solution and one observes Weyl points at the locations and energies indicated in (b) and (c). The weight of the wave function associated with the lower orange band on each A lattice is shown in (e) and is in perfect agreement with (a) and (d).

to the total number of checkerboard layers as given in Eq. (20). The surface switching along the line Γ-M in the Brillouin zone pins the presence of Weyl nodes to occur along these lines as shown in Figs. 8(b)–8(d). Figures 8(b) and 8(c) show the location of the Weyl nodes in the three-dimensional Brillouin zone from a top view in the k_z direction and a two-dimensional cut at $k_y = 0$, respectively, where red dots correspond to positive and blue dots to negative Berry charge. These nodes were found numerically by scanning the energy spectrum of the fully periodic lattice model over the entire Brillouin zone for energy gaps smaller than $E/t < 0.1$ and a subsequent computation of the Berry charge of a small sphere around these points. The numerical search for the Weyl points is greatly simplified by the fact that they are only allowed to occur at energies corresponding to the single-layer eigenvalues (the Fermi arcs traverse the Weyl points), and that they can occur only along the lines of diverging $r(\mathbf{k})$ as shown in Fig. 8(d). We see that the orange bands, which correspond to $E_\pm(\mathbf{k})$ and are thus associated with the Fermi arcs, cross the bulk gaps exactly at the same momentum and energy values as found for the three-dimensional periodic model in Figs. 8(b) and 8(c). In Fig. 9, we show plots for the Berry curvature for different N, which show that the value of the Berry curvature diverges along the line in the surface Brillouin zone where the Weyl nodes sit. The surface switching of the boundary state along the line Γ-Y in the Brillouin zone takes place also in the absence of Weyl nodes and comes about due to the complete attachment of the boundary-state energy bands to the bulk yielding its corresponding wave function completely delocalized by which surface switching is facilitated. The energy band at $E/t = 0$

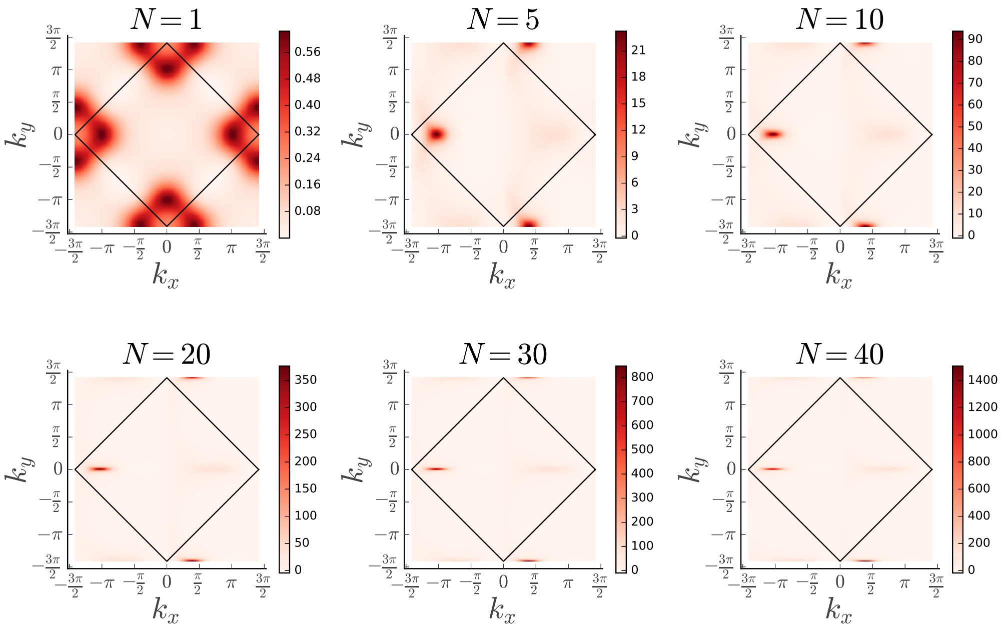

FIG. 9. Berry curvature associated with $\Psi_-(\mathbf{k})$ for the checkerboard model with $t'/t = t_2/t = t_\perp/t = V/t = 1$ for a different number of layers $N = 1,5,10,20,30,40$. The black line indicates the Brillouin zone. We see that the Berry curvature has maxima at those points in the Brillouin zone corresponding to the location of the Weyl points.

along Γ-Y is highly degenerate and corresponds to the energy solutions of the intermediate B (green) sites. That the states belonging to these sites have zero energy along the line $k_x = 0$ can be understood by realizing that hopping from the A lattices to the intermediate B lattices only take place in the x direction. The boundary state switching surfaces four times is also confirmed by the plot of the weight of the wave function of this state on each individual checkerboard layer shown in Fig. 8(e). We see that the surface state localizes to the top and bottom layer in complete accordance with Fig. 8(a). Upon varying the value of the staggering potential with upper bound $|V/t| \leqslant 2$ such that the checkerboard lattices remain in the nonzero Chern number regime, we find that the number, location in the Brillouin zone and energy value of the Weyl nodes change. However, they always remain on the $k_y = 0$ line. As we increase the interlayer coupling, we find numerically that only two Weyl nodes remain, which are pinned in the three-dimensional Brillouin zone slightly below $k_z = 0$ at the points M and $-M$ in the k_xk_y-plane with energies going to $E/t \approx 1$ and -1, respectively.

It is tempting to assume that the Weyl nodes and Fermi arcs disappear when the Chern number carried by the individual checkerboard lattices goes to zero. However, if the Hamiltonian of the checkerboard lattice in the trivial phase is fine-tuned to remain close to the topological phase transition, we find that a Weyl-semimetal phase is still supported by the three-dimensional lattice as shown in Fig. 10 for $V/t = 2.1$. Figures 10(a) and 10(e) shows that the surface state still switches surfaces four times, albeit with a weaker localization to the surfaces as before. Again, the surface switching along the line Γ-M is facilitated by the presence of Weyl nodes, whose location and energy values are shown in Figs. 10(b) and 10(c) and they correspond to what we observe in the energy spectrum shown in Fig. 10(d). Similarly, the surface switching along the line Γ-Y is due to the attachment of the surface state energy to the bulk bands. Upon increasing V/t, such that the Hamiltonian on the checkerboard lattice moves further away from the topological phase transition, we find that the Weyl nodes disappear completely when $V/t \gtrsim 2.55$.

Lastly, we briefly mention two more cases. In the first, the A lattice is in the Chern-insulator phase but the energy spectrum of the three-dimensional model does not support a Weyl phase as shown in Fig. 11(a), which is due to the weak interplanar coupling. In Fig. 11(b), we have plotted the inverse localization length and one can indeed see that there is a Fermi arc, which carries a Chern number. In the second case, we present an example where the A lattice is in the trivial topological phase, there are no Weyl points in the three-dimensional lattice as shown in Fig. 11(c), but there are still Fermi arcs as shown in Fig. 11(d). These Fermi arcs carry a zero Chern number and are thus not topologically protected.

D. Three dimensions, second example: Weyl semimetals and layered Chern insulators in pyrochlore iridate slabs

A pyrochlore lattice is built from alternating kagome (A) and triangular (B) layers, where successive kagome lattices are shifted relative to each other as shown in Fig. 12(a). The lattice structure implies that conditions (i)–(iv) are fulfilled hence our general expression for the surface states applies.

In this section, we use the formalism introduced in Sec. II to show that pyrochlore slabs very generically support Fermi-arc-like surface states, regardless of the presence of Weyl points in the bulk. The novel scenario of Fermi-arc-like surface states in the absence of Weyl points is particularly pertinent for recent experiments.

A special case of the pyrochlore model where the spin-orbit coupling was restricted to only the kagome layers

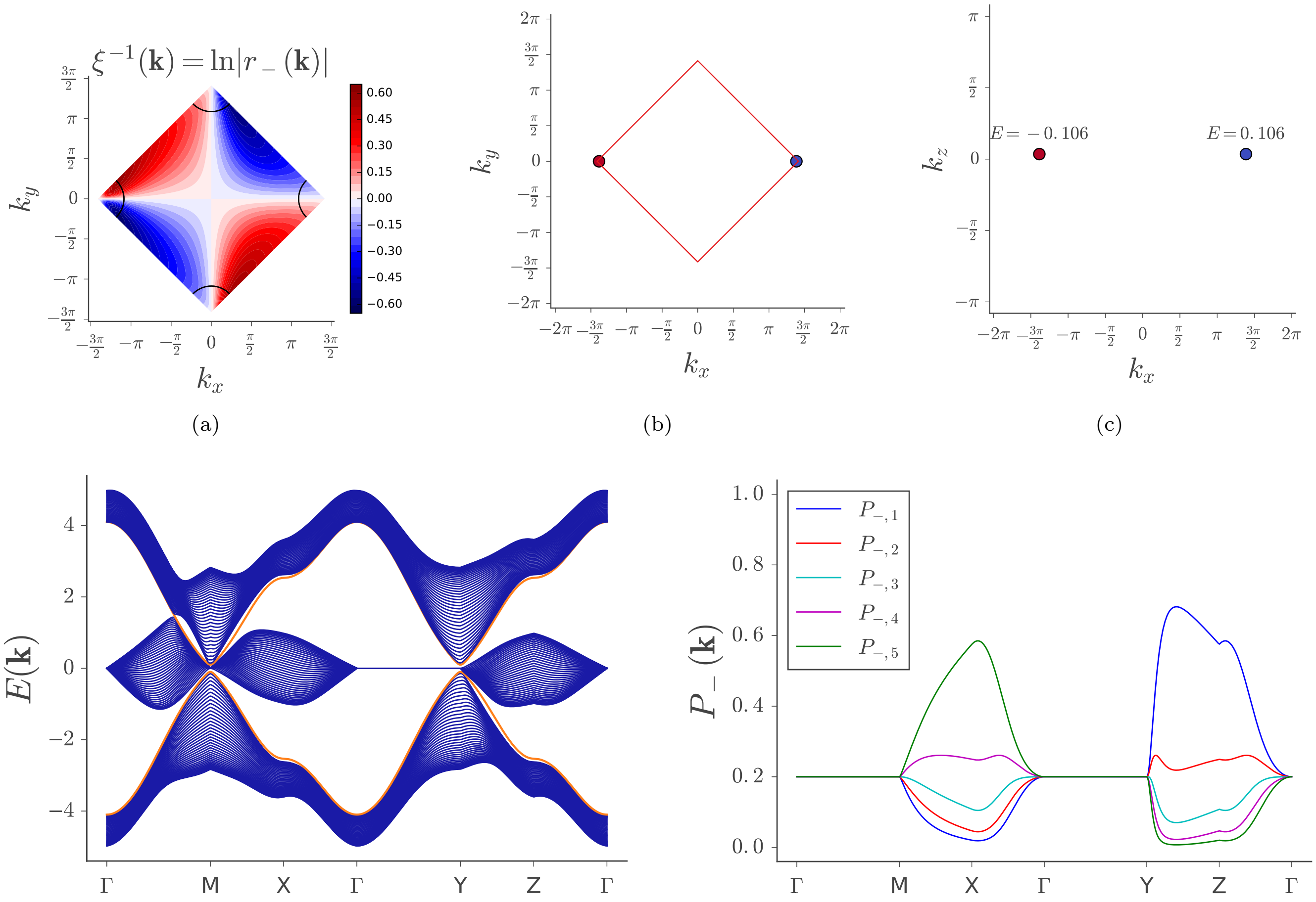

(a) (b) (c)

(d) (e)

FIG. 10. Solutions to the checkerboard model with zero-Chern number with $t'/t = t_2/t = t_\perp/t = 1$ and $V/t = 2.1$. In (a), we show the inverse localization length $\xi^{-1}(\mathbf{k}) = \ln|r_-(\mathbf{k})|$, where the black line is the energy contour of $E_-(\mathbf{k})$ at the chemical potential $\mu/t = -0.9$. The location of the Weyl nodes is shown in (b) and (c) with red and blue corresponding to positive and negative Berry charge, respectively. The energy spectrum along a path in the Brillouin zone, shown as an inset in Fig. 8(d), is shown in (d) with $N = 40$ and the energy given in units of t. The weight of the wave function associated with the lower orange band on each A lattice is shown in (e).

has been discussed extensively by two of the authors in Refs. [52,53]. Here we consider more realistic models of pyrochlore lattices making direct contact to real materials and experiments, namely $Eu_2Ir_2O_7$ [68] and $Nd_2Ir_2O_7$ [69] for which pertinent slabs have recently been grown and for potential future experiments on yet to be grown slabs of $Pr_2Ir_2O_7$. The model includes spin degree of freedom and has two parameters: the nearest-neighbor-hopping strength t and the spin-orbit-coupling parameter t_{SOC}. It is directly based on the model in Ref. [74], up to a rotation of the [111] direction in the z direction to describe the layered structure as in the models presented earlier. In contrast to the models discussed earlier, we do not assume a spin polarization in a globally fixed direction but we make use of the internal spin ordering of pyrochlore materials. This procedure is justified by the observation that different materials featuring the pyrochlore lattice structure realize phases with fixed but different spin configurations at low temperatures [75,76]. In the bulk, the pyrochlore lattice can be seen as a collection of corner sharing tetrahedra, where the lattice sites are located at the corners. In all these spin-ordered phases, the preferred orientation of a spin in the pyrochlore lattice is to point either towards or away from the center of the tetrahedron. A spin configuration with n spins pointing inwards is called n-in-(four-n)-out, which is equivalent to the (four-n)-in-n-out configuration. The configuration four-in-zero-out is often called the "all-in-all-out" configuration as for any tetrahedron either all spins are pointing outwards or all spins are pointing inwards [68,77]. In order to obtain a tight-binding model with a fixed spin configuration, we apply a different spin rotation on each site to transform the Hamiltonian to the all-in-all-out spin basis as shown in Fig. 12(b), and finally we project the Hamiltonian to the subspace of the spin configuration of interest. The Hamiltonians for the different spin configurations are listed in the Appendix.

Based on geometric considerations and intuition developed in the models before, we expect localized states for any spin configuration, as the local constraint involves three unit cells in the upper layer. Furthermore, the three-in-one-out and two-in-two-out configurations have topological nontrivial bands in the single-layer case, and hence fulfill condition (v). Applying Eq. (8) to the Hamiltonians given in Eq. (A2) reveals that

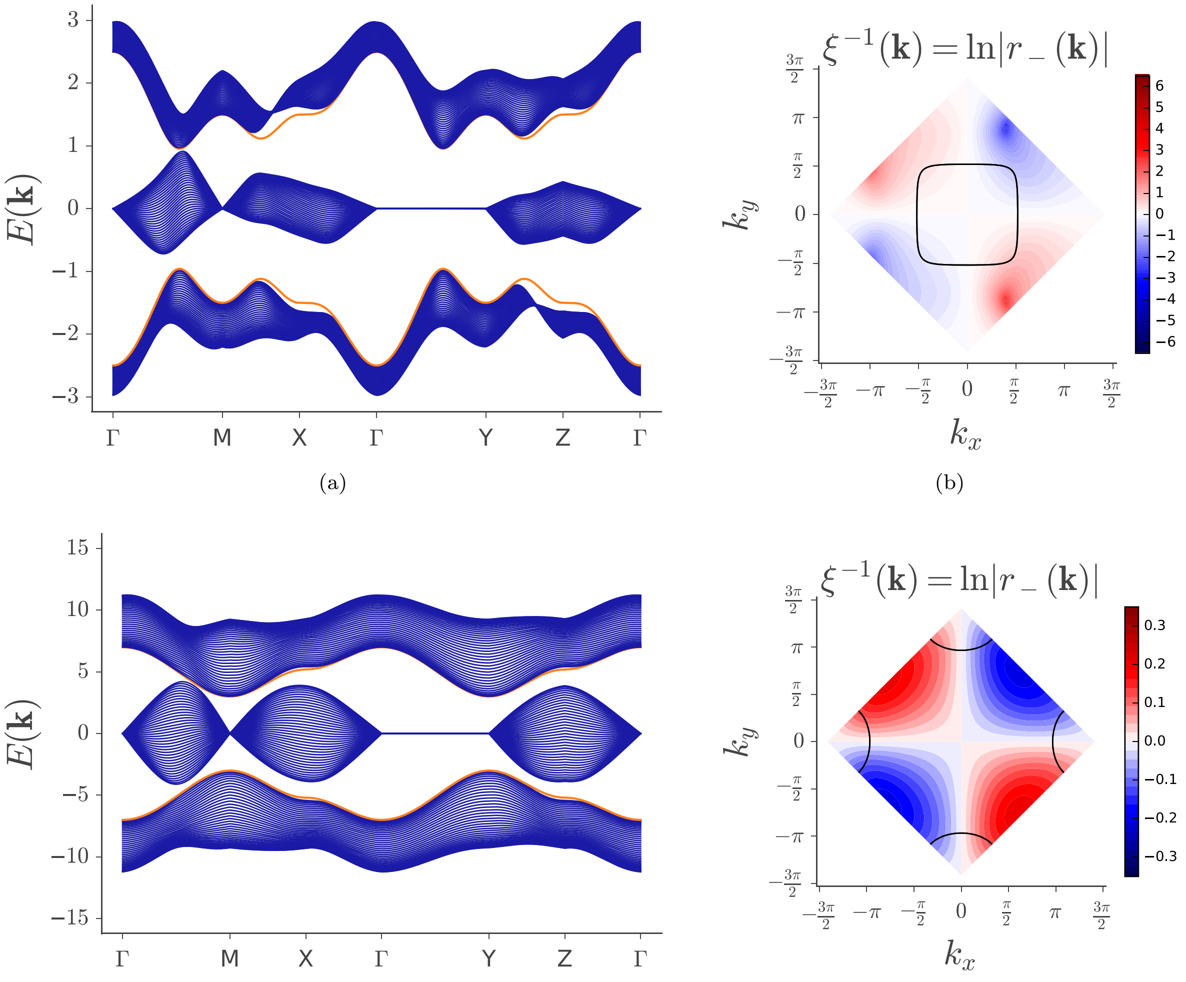

(a) (b)

(c) (d)

FIG. 11. (a) and (b) Solutions to the checkerboard model with nonzero Chern number with $t'/t = t_2/t = 1$ and $V/t = 0.5$ and $t_\perp/t = 0.57$. In (a), we show the energy spectrum with $N = 40$ and the energy given in units of t along a certain path in the Brillouin zone. Even though, the A lattice carries a Chern number, there are no Weyl points in the system. In (b), we show the inverse localization length $\xi^{-1}(\mathbf{k}) = \ln|r_-(\mathbf{k})|$, where the black line is the solution to $E_-(\mathbf{k})$ at the chemical potential $\mu/t = -1.6$. (c) and (d) Solutions with zero-Chern number with $t'/t = t_2/t = 1$ and $V/t = 5$ and $t_\perp/t = 3.1$. (c) The energy spectrum with $N = 40$ and the energy given in units of t. There are no Weyl points. (d) The inverse localization length with an equal-energy line at $\mu/t = -4$.

all of these models indeed have nontrivial surface states. The results for $r(\mathbf{k})$ are shown in Figs. 13(a)–13(c). While in the all-in-all-out configuration the surface state might be “hidden” by the bulk bands, in the two other configurations we find Fermi arcs when choosing the Fermi level in the bulk gap. The two-in-two-out configuration possesses Fermi arcs even without having Weyl points in the bulk.

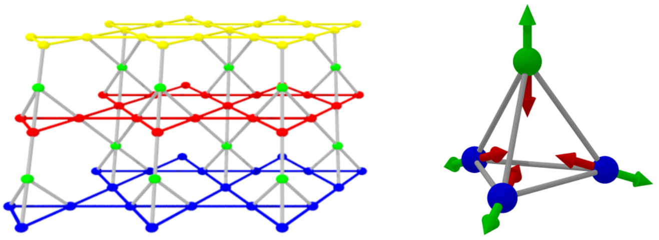

(a) (b)

FIG. 12. (a) The pyrochlore model featuring kagome lattices stacked on top of each other with a triangular lattice (green) in between. The kagome layers are shifted relative to each other and repeat every third layer. (b) The preferred spin directions pointing towards (red) or away from (green) the center.

In the all-in-all-out configuration, the model’s two parameters t and t_{SOC} only occur in the linear combination $t + \sqrt{2}t_{\mathrm{SOC}}$ after the spin transformation, hence we are left with a single effective parameter in this case. By diagonalizing the (3×3) A-lattice Hamiltonian $\mathcal{H}_{\mathbf{k},\mathbf{4-0}}$, we find a completely flat band, which is topologically trivial. Note, however, that this spin configuration cannot be physically realized in a single layer, because it would lead to a large magnetization, and should be viewed only in combination with the fourth spin on the intermediate B layers. In Fig. 14, a graphical representation of the full wave functions of a slab with two A lattices and one intermediate B lattice in the all-in-all-out configurations is shown. One easily recognizes the three bands that are given by our construction as they have zero weight (shown in black) on the intermediate B site with index 4.

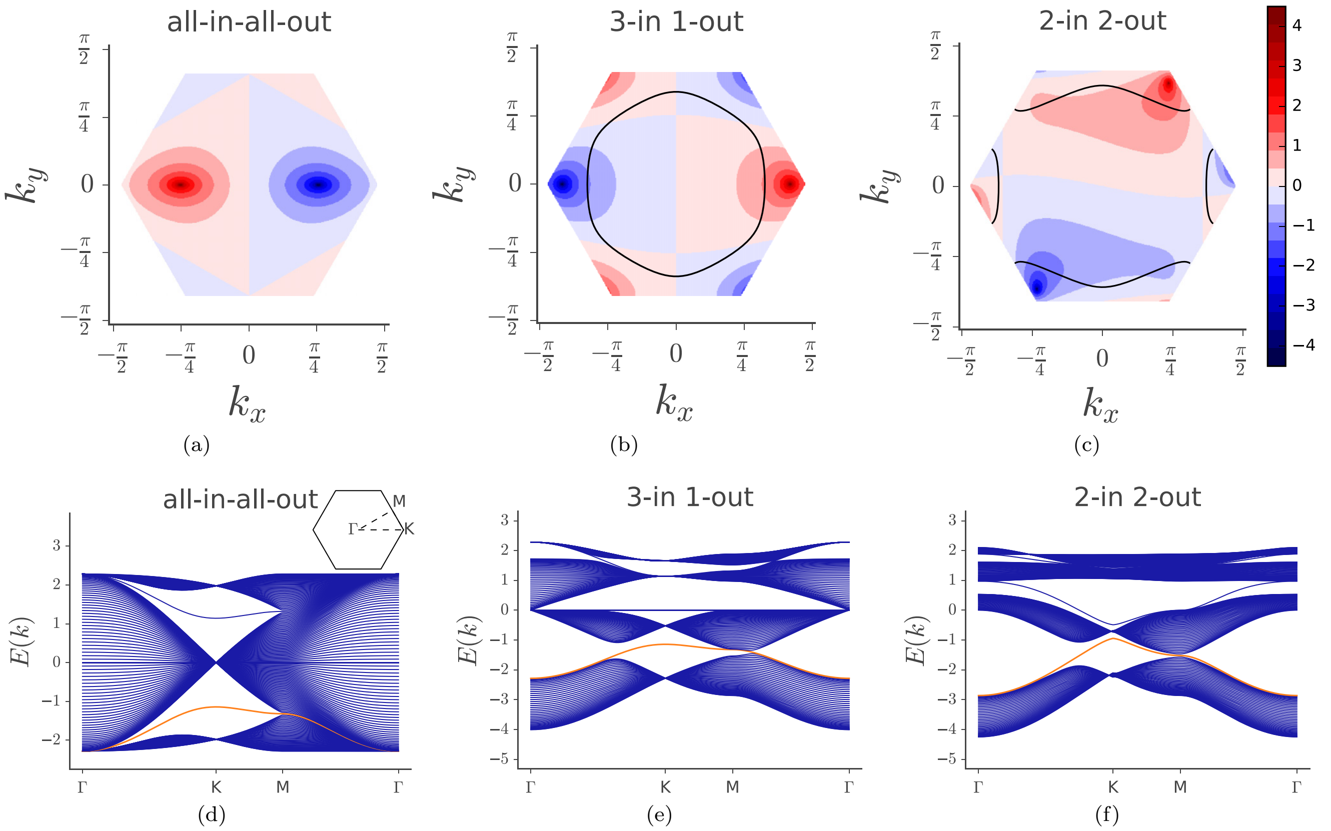

(a) (b) (c)

(d) (e) (f)

FIG. 13. (a)–(c) The inverse localization length $\xi^{-1}(\mathbf{k}) = \ln|r_1(\mathbf{k})|$ for the lowest surface states in the pyrochlore model shown for different spin configurations indicated in (d)–(f), respectively, with hopping parameters $t_{\mathrm{SOC}}/t = 0.1$. The black line in (b) and (c) is the energy contour at $\mu/t = -1.4$. (d)–(f) The energy spectra for different spin configurations with $N = 40$ and $t_{\mathrm{SOC}}/t = 0.1$. Energy is given in units of t.

The three-in-one-out configuration is not uniquely defined in a finite slab, as the surface normals represent a special direction in the model. For the sake of brevity, we restricted the discussion to the most natural choice of the three-in-one-out configurations, where we take the single "out"-spin to be on the intermediate site [green in Fig. 12(a)]. Hence the kagome layers of the all-in-all-out and the three-in-one-out configurations have the same A-lattice Hamiltonian $\mathcal{H}_{\mathbf{k}}$. In contrast to the existence of the surface states in all spin configurations, only the three-in-one-out model harbors Weyl points in the bulk, and does so only for small values of t_{SOC}/t in accordance with Ref. [70], as is shown in Figs. 13(d)–13(f). In Fig. 15, the Berry curvature is shown for this model for a different number of A lattices. One indeed sees a divergence of the Berry curvature along those lines in the Brillouin zone where the Weyl points appear.

E. Three dimensions, final example: trivial states on layered honeycomb lattices

In this section, we study tight-binding models inspired by KHgX (X = As, Sb, Bi) whose underlying lattice structure is a three-dimensional analog of the two-dimensional models in Figs. 3(b) and 3(c). The lattice is formed by stacked honeycomb lattices, which are connected via triangular lattice layers. In Fig. 16(a), we show the A lattice of this model, which has five sites in the unit cell. Figure 16(b) features the honeycomb model with one and a half A lattices.

The surface states of KHgX are known to be intriguing featuring novel so-called hourglass fermions [78]. However, the surface that we study is not expected to support these states,

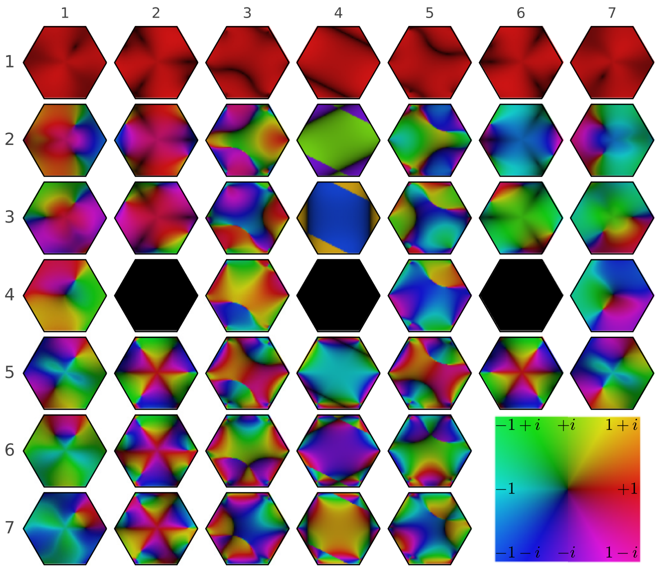

FIG. 14. The wave-function components for a two layer slab of the all-in-all-out model. The columns correspond to the different eigenstates and the rows correspond to the sites, the wave-function values are shown throughout the BZ using the domain coloring method shown in the right bottom corner.

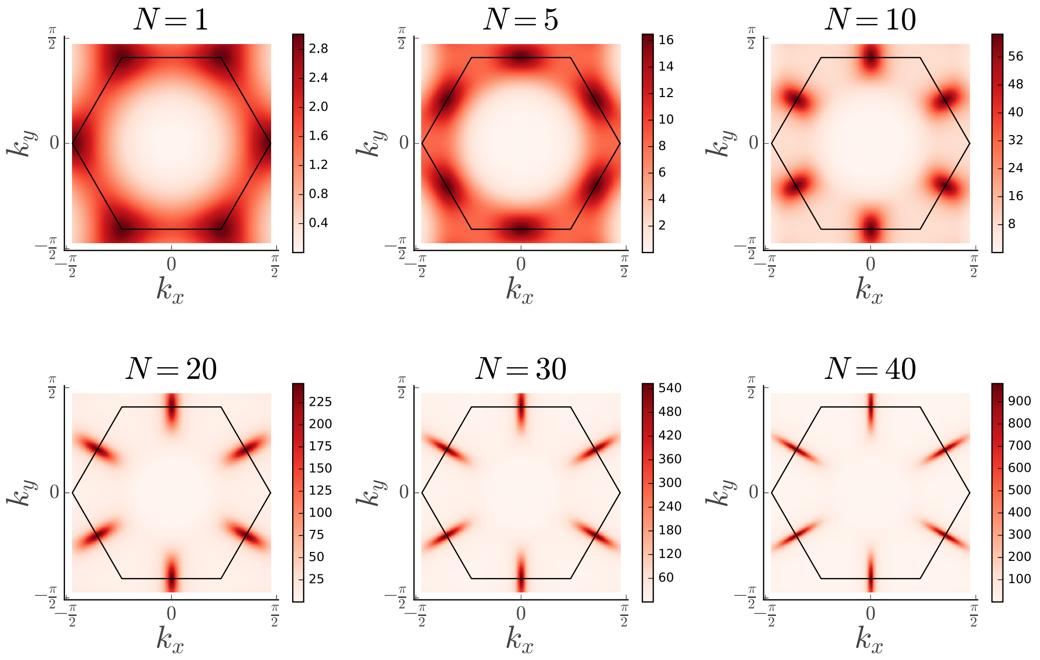

FIG. 15. Berry curvature associated with $\Psi_1(\mathbf{k})$ for the pyrochlore model with hopping parameters $t_{\mathrm{SOC}}/t = 0.1$ in the three-in-one-out configuration.

which we will here corroborate by showing that our exact solution inevitably leads to trivial states delocalized over the full sample. While the actual KHgX materials are time-reversal symmetric we here treat "half" of the model as this turns out to be sufficient for understanding the absence of surface states. Our argument proceeds in a very similar fashion as for the analogous two-dimensional lattices [Figs. 3(b) and 3(c)] that defy surface states.

To describe the honeycomb layers, we use Haldane's model [6], such that the Hamiltonian $\mathcal{H}_{\mathbf{k}}^{\text{honey}}$ and energy for the odd-numbered honeycomb layers are given in Eqs. (32) and (33), respectively, with

$$d_0(\mathbf{k}) = t_2 \cos\phi \sum_{i=1}^{3} \cos(\mathbf{k}\cdot\boldsymbol{\delta}_i'), \quad d_x(\mathbf{k}) - i d_y(\mathbf{k}) = t\,\gamma_{\mathbf{k}},$$

$$d_z(\mathbf{k}) = V - t_2 \sin\phi \sum_{i=1}^{3} \sin(\mathbf{k}\cdot\boldsymbol{\delta}_i'), \tag{38}$$

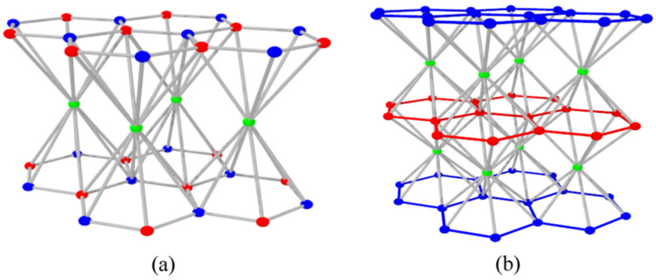

FIG. 16. (a) The A lattice of the honeycomb model featuring honeycomb lattices (red and blue sites) stacked on top of each other with a triangular lattice (green) in between. Note the sublattice exchange in the alternating honeycomb lattices. (b) The honeycomb model where one A lattice is composed of one blue and red honeycomb lattice and the green triangular lattice in between.

where t (t_2) is the (next-)nearest-neighbor hopping amplitude, ϕ is the phase picked up in a next-nearest-neighbor hopping, which we from now on set as $\phi = \pi/2$, V is the staggering potential, $\gamma_{\mathbf{k}} \equiv \sum_{i=1}^{3} \exp(i\mathbf{k}\cdot\boldsymbol{\delta}_i)$ and $\boldsymbol{\delta}_i$ ($\boldsymbol{\delta}_i'$) are the (next-)nearest-neighbor vectors specified in a footnote below.[3] The Chern number at half-filling in a single layer is $C = 1$ for $t/t_2 = 1$ and $|V/t_2| \lesssim 1.75$ and zero otherwise. The Hamiltonian for the even-numbered honeycomb layers is simply given by $\mathcal{H}_{-\mathbf{k}}^{\text{honey}}$, such that the Hamiltonian for the A lattice $\mathcal{H}_{\mathbf{k}}$ reads

$$\mathcal{H}_{\mathbf{k}} = \left(\begin{array}{ccccc} \multicolumn{2}{c}{\mathcal{H}_{\mathbf{k}}^{\text{honey}}} & \begin{array}{c} t_\perp\gamma_{-\mathbf{k}} \\ t_\perp\gamma_{\mathbf{k}} \end{array} & \multicolumn{2}{c}{0} \\ t_\perp\gamma_{\mathbf{k}} & t_\perp\gamma_{-\mathbf{k}} & 0 & t_\perp\gamma_{-\mathbf{k}} & t_\perp\gamma_{\mathbf{k}} \\ \multicolumn{2}{c}{0} & \begin{array}{c} t_\perp\gamma_{\mathbf{k}} \\ t_\perp\gamma_{-\mathbf{k}} \end{array} & \multicolumn{2}{c}{\mathcal{H}_{-\mathbf{k}}^{\text{honey}}} \end{array}\right),$$

where we used that $\gamma_{\mathbf{k}}^{*} = \gamma_{-\mathbf{k}}$. The Hamiltonian for N A lattices is given in Eqs. (2) and (3) with $h_{\mathbf{k}} = 0$, $t_{\perp,s,\alpha} = t_\perp \in \mathbb{R}\,\forall\, s,\alpha$, and $f_{A,4}(\mathbf{k}) = f_{B,2}(\mathbf{k}) = t_\perp\gamma_{\mathbf{k}}$ and $f_{A,5}(\mathbf{k}) = f_{B,1}(\mathbf{k}) = t_\perp\gamma_{-\mathbf{k}}$.

We first discuss the case where the staggering potential is zero, i.e., $V = 0$, such that $\mathcal{H}_{-\mathbf{k}}^{\text{honey}} = \sigma_x \mathcal{H}_{\mathbf{k}}^{\text{honey}} \sigma_x$. As in the analogous two-dimensional examples we notice that the A lattice itself exists out of two sub-A lattices and one sub-intermediate B lattice. Solving the Schrödinger equation for these $n_{\text{sub}} = 2$ solutions yields

---

[3] The nearest-neighbor vectors read $\boldsymbol{\delta}_1 = (1,\sqrt{3})/2$, $\boldsymbol{\delta}_2 = (1,-\sqrt{3})/2$, and $\boldsymbol{\delta}_3 = -(1,0)$. The next-nearest-neighbor vectors are $\boldsymbol{\delta}_1' = (3,\sqrt{3})/2$, $\boldsymbol{\delta}_2' = (-3,\sqrt{3})/2$, and $\boldsymbol{\delta}_3' = (0,-\sqrt{3})$, where the complete set of next-nearest-neighbor vectors is given by $\{\pm\boldsymbol{\delta}_i'\}$.

$$|\Phi_\pm(\mathbf{k})\rangle \doteq \tilde{\mathcal{N}}_\pm(\mathbf{k}) \begin{pmatrix} \phi_{\pm,1}(\mathbf{k}) \\ \phi_{\pm,2}(\mathbf{k}) \\ 0 \\ s_\pm(\mathbf{k})\phi_{\pm,2}(\mathbf{k}) \\ s_\pm(\mathbf{k})\phi_{\pm,1}(\mathbf{k}) \end{pmatrix},$$

where we have absorbed the sublattice exchange into the wave function, $\tilde{\mathcal{N}}_\pm(\mathbf{k})$ is the normalization factor, and we see immediately that $s_\pm(\mathbf{k}) = -1$. This leads to

$$r_\pm(\mathbf{k}) = -s_\pm(\mathbf{k}) \frac{\gamma_{-\mathbf{k}}\, \phi_{\pm,2}(\mathbf{k}) + \gamma_{\mathbf{k}}\, \phi_{\pm,1}(\mathbf{k})}{\gamma_{\mathbf{k}}\, \phi_{\pm,1}(\mathbf{k}) + \gamma_{-\mathbf{k}}\, \phi_{\pm,2}(\mathbf{k})} = 1.$$

The other three solutions have the solution $\Phi_i(\mathbf{k}) = \bigoplus_{s=1}^{5} \phi_{i,s}(\mathbf{k})$ with $i = 1,2,3$ and the energy E_i, and we again find $|r_i(k_x)| = 1, \forall i$.

When $V \neq 0$, we no longer find two solutions whose wave function has zero weight on the subintermediate B site. This is simply the case because the Hamiltonian on the even-numbered honeycomb layers $\mathcal{H}^{\text{honey}}_{-\mathbf{k}}$ has wave-function solutions who can only be related to the wave-function solutions of the Hamiltonian $\mathcal{H}^{\text{honey}}_{\mathbf{k}}$ via $\mathbf{k} \to -\mathbf{k}$ such that a solution $|\Phi_\pm(\mathbf{k})\rangle$ cannot be defined in terms of the wave-function solutions of $\mathcal{H}^{\text{honey}}_{\mathbf{k}}$ alone. However, we still find solutions of the form Eq. (5) with $|r_i(k_x)| = 1, \forall i$ with $i = 1,2,3,4,5$ indicating that this system remains trivial.

The energy spectrum for this Hamiltonian along a path in the two-dimensional Brillouin zone is shown in Fig. 17. There are touching points, which are not Weyl points as there is no state crossing the bulk gap. When each individual honeycomb layer is a Chern insulator, the Chern number of the full system equals the Chern number of one of the honeycomb layers, i.e., there is no enhancement of the band Chern number as we generically observe in models where $r(\mathbf{k})$ behaves nontrivially. Finally, we note that taking two time-reversed copies of our model yields a time-reversal symmetric model, which makes contact to the arguments put forward in Ref. [78] where no specific lattice Hamiltonian is investigated but instead symmetry arguments are used to study possible boundary states on several surfaces. Our findings are corroborating the conclusion of Ref. [78] that there are no nontrivial surface states on the (001) surface of the KHgX materials class.

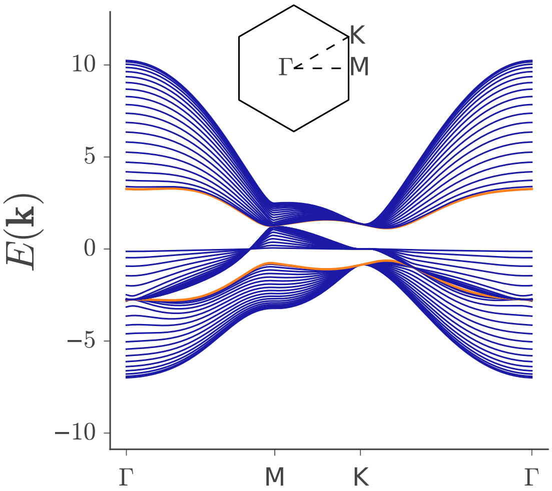

FIG. 17. Plot of the energy spectrum of the honeycomb model with $N = 20$ A lattice layers and the energy given in units of t, with $t_2/t = t_\perp/t = 1$ and $V/t = 0.5$. The Brillouin zone is shown as an inset in the figure. The orange bands correspond to the exactly-solvable states. The total Chern number is one.

IV. DISCUSSION

In this work, we have presented exact solutions for the surface states of a variety of topological and nontopological phases on geometrically frustrated lattices. Rather being based on fine-tuning or numerical approximations, our solutions are remarkably general. All we need to assume is the appropriate frustrated lattice structure—which is frequently represented in real materials—in combination with local coupling between neighboring layers and translation symmetry. It should be emphasized that the exact solutions are stable; they do *not* represent fragile states on the verge of being topological but are rather representatives that can be obtained arbitrarily deep into the various topological phases we discuss. For instance, while the exact solvability depends on having a local hopping coupling the different A layers only via hopping to the intermediate B layers, the various (topological) phases are stable to the inclusion of such terms. Considering the pyrochlore iridates including $Eu_2Ir_2O_7$ and $Nd_2Ir_2O_7$ as particularly prominent examples, quantitatively more accurate descriptions have next-nearest-neighbor hopping terms of the order $t_2/t \approx 0.08$–0.2 [19,79]. This is, albeit certainly large enough to be quantitatively important, likely small enough such that the intriguing phenomena, present in our large class of solvable models, such as Fermi arcs despite the absence of Weyl nodes, may be realized these materials.

Given the far reaching success of harnessing the properties of frustrated systems through the microscopic understanding of their ubiquitous flat bands in terms of localized modes, we hope that our work will spur a development in which this large body of knowledge will be exploited in order to deepen our understanding also of topological phases of matter. We have here initiated such a program by analytically calculating a number of properties that have previously been accessible by numerical simulation and in fine-tuned models. Building on this, aspects of quantum transport, stability to disorder and interactions provide obvious new avenues.

Our investigation has thus far highlighted several generic facts. This includes the role of lattice geometry for topological phases that are not intrinsically symmetry protected; although Chern insulators and Weyl semimetals rely on breaking symmetries, in contrast to phases being protected thereby, we have shown that they cannot be realized with strictly local (nearest neighbor) constraints on lattices that satisfy conditions (i)–(iii) but fail to satisfy condition (iv), while they are readily realized once also condition (iv) is satisfied. We provided explicit examples of lattices—including two-dimensional lattices akin to kagome lattices but with different stacking properties as well as a three-dimensional system corresponding to the (100) grown surface of the KHgX materials class—whose structure prohibits the formation of topological phases. In glaring contrast, spin-orbit-coupled particles on the kagome and pyrochlore lattices are ideally suited for realizing topological phases and, even more generally, they support novel surface states.

In fact, we have here corroborated the recent observation [52] that there is no one-to-one dichotomy between surface Fermi arcs and the existence of bulk Weyl nodes; while the Fermi arclike surface bands are always partially attached to bulk bands, these surface bands exist also in the absence of Weyl nodes in the bulk. The Fermi arcs occurring without Weyl nodes are similar to those associated with type-II Weyl excitations in that they are generally blurred in parts of the surface Brillouin zone due the finite density of states in the bulk. While this is a feature that distinguishes them from the surface states corresponding to type-I Weyl systems, our exact solutions, which remain identical tuning from weak to strong interlayer coupling, highlight that both the surface eigenstates and dispersion are in principle completely unrelated to the existence of bulk Weyl nodes. These observations have direct bearing for engineered as well as naturally existing materials. Notably, single-crystal slabs of the pyrochlore iridates $Eu_2Ir_2O_7$ [68] and $Nd_2Ir_2O_7$ [69], grown precisely in the (111) direction that we consider have been recently synthesized. The possibilities of experimental probing are further extended by growing the pertinent pyrochlore slabs with variable chemical composition and doping [80]. Beyond being of great interest on their own, the study of the pyrochlores on the slab geometry may lead to a better understanding of the rich variety of phenomena associated with bulk pyrochlore iridates [74,81–86].

Our work also opens up questions of fundamental nature that call for further disquisition. Saliently, we have observed that the solvable eigenstates generically carry a Chern number being equal to the sum of the Chern numbers of the pertinent bands in all layers. This happens immediately for arbitrarily weak interlayer coupling as the eigenstates of the different layers hybridize and amounts to a "topological selection rule" whose implications and generality we have only touched upon here.

Finally, we note that the anatomy of the surface states we have provided, dissecting them into tinker toylike constituents, may serve as a guide when engineering artificial materials. In the context of designing devices and quantum simulators, either in optical, cold atom systems or in the solid state, the fact that the exact solution holds at any finite size is a particularly attractive feature.

ACKNOWLEDGMENTS

We acknowledge discussions with Claudio Castelnovo, Nigel Cooper, Sian Dutton, Roderich Moessner, and Masafumi Udagawa. This work is supported by Deutsche Forschungsgemeinschaft (DFG)'s Emmy Noether program (BE 5233/1-1), the Helmholtz VI "New States of Matter and Their Excitations," the Swedish research council (VR) and the Wallenberg Academy Fellows program of the Knut and Alice Wallenberg Foundation.

APPENDIX: PYROCHLORE HAMILTONIANS

The following Hamiltonians for the pyrochlore model correspond to the different spin configurations, where the specific configurations are given as subscripts and the blocks of the Hamiltonian matrix are given as defined in Eq. (2):

$$k_1 = \sqrt{2}k_x, \quad k_2 = \frac{k_x + \sqrt{3}k_y}{\sqrt{2}}, \quad k_3 = \frac{k_x - \sqrt{3}k_y}{\sqrt{2}}, \quad k_a = \frac{k_x}{\sqrt{2}} - \frac{k_y}{\sqrt{6}}, \quad k_b = \frac{k_x}{\sqrt{2}} + \frac{k_y}{\sqrt{6}}, \quad k_c = \frac{\sqrt{2}k_y}{\sqrt{3}}, \tag{A1}$$

$$\begin{aligned}
\mathcal{H}_{\mathbf{k},\mathbf{4-0}} = \mathcal{H}_{\mathbf{k},\mathbf{3-1}} &= -\frac{\sqrt{2}t + 2t_{\mathrm{SOC}}}{\sqrt{3}} \begin{pmatrix} 0 & \sqrt{2}\cos(k_1) & (1+i)\cos(k_3) \\ \sqrt{2}\cos(k_1) & 0 & (1-i)\cos(k_2) \\ (1-i)\cos(k_3) & (1+i)\cos(k_2) & 0 \end{pmatrix} + m, \\
\mathcal{H}_{\mathbf{k},\mathbf{2-2}} &= -\frac{\sqrt{2}t + 2t_{\mathrm{SOC}}}{\sqrt{3}} \begin{pmatrix} 0 & \sqrt{2}\cos(k_1) & 0 \\ \sqrt{2}\cos(k_1) & 0 & 0 \\ 0 & 0 & 0 \end{pmatrix} \\
&\quad + \frac{1}{3}(\sqrt{2}t - t_{\mathrm{SOC}}) \begin{pmatrix} 0 & 0 & (-3i+\sqrt{3})\cos(k_3) \\ 0 & 0 & (3 - i\sqrt{3})\cos(k_2) \\ (3i+\sqrt{3})\cos(k_3) & (3+i\sqrt{3})\cos(k_2) & 0 \end{pmatrix} + m, \\
\mathcal{H}^{A}_{\perp,4-0}(\mathbf{k}) &= -\frac{\sqrt{2}t + 2t_{\mathrm{SOC}}}{2\sqrt{3}} \left((1-i)e^{-ik_a} \;\; (1+i)e^{+ik_b} \;\; \sqrt{2}e^{-ik_c}\right)^T, \\
\mathcal{H}^{A}_{\perp,3-1}(\mathbf{k}) &= -\frac{\sqrt{2}t - t_{\mathrm{SOC}}}{6} \left((3-\sqrt{3}i)e^{-ik_a} \;\; (\sqrt{3}-3i)e^{+ik_b} \;\; \sqrt{6}(1-i)\sqrt{2}e^{-ik_c}\right)^T, \\
\mathcal{H}^{A}_{\perp,2-2}(\mathbf{k}) &= -\frac{\sqrt{2}t - t_{\mathrm{SOC}}}{6} \left((3-\sqrt{3}i)e^{-ik_a} \;\; (\sqrt{3}-3i)e^{+ik_b} \;\; \frac{2\sqrt{3}(t + 2t_{\mathrm{SOC}})}{\sqrt{2}t - t_{\mathrm{SOC}}}e^{-ik_c}\right)^T, \\
\mathcal{H}^{B}_{\perp}(\mathbf{k}) &= \mathcal{H}^{A}_{\perp}(\mathbf{k} \to -\mathbf{k}).
\end{aligned} \tag{A2}$$

[1] K. von Klitzing, G. Dorda, and M. Pepper, New Method for High-Accuracy Determination of the Fine-Structure Constant Based on Quantized Hall Resistance, Phys. Rev. Lett. **45**, 494 (1980).

[2] M. Z. Hasan and C. L. Kane, Colloquium: Topological insulators, Rev. Mod. Phys. **82**, 3045 (2010).

[3] X.-L. Oi and S.-C. Zhang, Topological insulators and superconductors, Rev. Mod. Phys. **83**, 1057 (2011).

[4] P. Hosur and X. Qi, Recent developments in transport phenomena in Weyl semimetals, C. R. Phys. **14**, 857 (2013).

[5] C. Nayak, S. H. Simon, A. Stern, M. Freedman, and S. Das Sarma, Non-Abelian anyons and topological quantum computation, Rev. Mod. Phys. **80**, 1083 (2008).

[6] F. D. M. Haldane, Model for a Quantum Hall Effect without Landau Levels: Condensed-Matter Realization of the "Parity Anomaly", Phys. Rev. Lett. **61**, 2015 (1988).

[7] D. J. Thouless, M. Kohmoto, M. P. Nightingale, and M. den Nijs, Quantized Hall Conductance in a Two-Dimensional Periodic Potential, Phys. Rev. Lett. **49**, 405 (1982).

[8] D. R. Hofstadter, Energy levels and wave functions of Bloch electrons in rational and irrational magnetic fields, Phys. Rev. B **14**, 2239 (1976).

[9] C.-Z. Chang, J. Zhang, X. Feng, J. Shen, Z. Zhang, M. Guo, K. Li, Y. Ou, P. Wei, L.-L. Wang, Z.-Q. Ji, Y. Feng, S. Ji, X. Chen, J. Jia, X. Dai, Z. Fang, S.-C. Zhang, K. He, Y. Wang, L. Lu, X.-C. Ma, and Q.- K Xue, Experimental observation of the quantum anomalous Hall effect in a magnetic topological insulator, Science **340**, 167 (2013).

[10] G. Jotzu, M. Messer, R. Desbuquois, M. Lebrat, T. Uehlinger, D. Greif, and T. Esslinger, Experimental realization of the topological Haldane model with ultracold fermions, Nature (London) **515**, 237 (2014).

[11] C. L. Kane and E. J. Mele, Quantum Spin Hall Effect in Graphene, Phys. Rev. Lett. **95**, 226801 (2005).

[12] C. L. Kane and E. J. Mele, Z_2 Topological Order and the Quantum Spin Hall Effect, Phys. Rev. Lett. **95**, 146802 (2005).

[13] B.-Q. Lv, H.-M. Weng, B.-B. Fu, X.-P. Wang, H. Miao, J. Ma, P. Richard, X.-C. Huang, L.-X. Zhao, G.-F. Chen, Z. Fang, X. Dai, T. Qian, and H. Ding, Experimental Discovery of Weyl Semimetal TaAs, Phys. Rev. X **5**, 031013 (2015).

[14] S.-Y. Xu, I. Belopolski, N. Alidoust, M. Neupane, G. Bian, C. Zhang, R. Sankar, G. Chang, Z. Yuan, C.-C. Lee, S.-M. Huang, H. Zheng, J. Ma, D. S. Sanchez, B. K. Wang, A. Bansil, F. Chou, P. P. Shibayev, H. Lin, S. Jia, and M. Z. Hasan, Discovery of a Weyl fermion semimetal and topological Fermi arcs, Science **349**, 613 (2015).

[15] L. Lu, Z. Wang, D. Ye, L. Ran, L. Fu, J. D. Joannopoulos, and M. Soljačić, Experimental observation of Weyl points, Science **349**, 622 (2015).

[16] M. Z. Hasan, S.-Y. Xu, I. Belopolski, and S.-M. Huang, Discovery of Weyl Fermion semimetals and topological Fermi arc states, Annu. Rev. Condens. Matter Phys. **8**, 289 (2017).

[17] S. Murakami, Phase transition between the quantum spin Hall and insulator phases in 3D: Emergence of a topological gapless phase, New J. Phys. **9**, 356 (2007).

[18] G. E. Volovik, *The Universe in a Helium Droplet* (Clarendon Press, Oxford, 2003).

[19] X. Wan, A. M. Turner, A. Vishwanath, and S. Y. Savrasov, Topological semimetal and Fermi-arc surface states in the electronic structure of pyrochlore iridates, Phys. Rev. B **83**, 205101 (2011).

[20] A. A. Burkov and L. Balents, Weyl Semimetal in a Topological Insulator Multilayer, Phys. Rev. Lett. **107**, 127205 (2011).

[21] Z. K. Liu1, B. Zhou, Y. Zhang, Z. J. Wang, H. M. Weng, D. Prabhakaran, S.-K. Mo, Z. X. Shen, Z. Fang, X. Dai, Z. Hussain, and Y. L. Chen, Discovery of a three-dimensional topological dirac semimetal, Na_3Bi, Science **343**, 864 (2014).

[22] Z. K. Liu, J. Jiang, B. Zhou, Z. J. Wang, Y. Zhang, H. M. Weng, D. Prabhakaran, S-K. Mo, H. Peng, P. Dudin, T. Kim, M. Hoesch, Z. Fang, X. Dai, Z. X. Shen, D. L. Feng, Z. Hussain, and Y. L. Chen, A stable three-dimensional topological Dirac semimetal Cd_3As_2, Nat. Mater. **13**, 677 (2014).

[23] A. Y. Kitaev, Unpaired Majorana fermions in quantum wires, Phys.-Usp. **44**, 131 (2001).

[24] I. Affleck, T. Kennedy, E. H. Lieb, and H. Tasaki, Rigorous Results on Valence-Bond Ground States in Antiferromagnets, Phys. Rev. Lett. **59**, 799 (1987).

[25] C.-X. Liu, X.-L. Qi, and S.-C. Zhang, Half quantum spin Hall effect on the surface of weak topological insulators, Physica E **44**, 906 (2012).

[26] S. Mao, Y. Kuramoto, K.-I. Imura, and A. Yamakage, Analytic Theory of Edge Modes in Topological Insulators, J. Phys. Soc. Jpn. **79**, 124709 (2010).

[27] S.-Q. Shen, W.-Y. Shan, and H.-Z. Lu, Topological insulator and the Dirac equation, SPIN **1**, 33 (2011).

[28] M. König, H. Buhmann, L. W. Molenkamp, T. Hughes, C.-X. Liu, X.-L. Qi, and S.-C. Zhang, The quantum spin Hall effect: Theory and experiment, J. Phys. Soc. Jpn. **77**, 031007 (2008).

[29] R. S. K. Mong and V. Shivamoggi, Edge states and the bulk-boundary correspondence in Dirac Hamiltonians, Phys. Rev. B **83**, 125109 (2011).

[30] B. Zhou, H.-Z. Lu, R.-L. Chu, S.-Q. Shen, and Q. Niu, Finite Size Effects on Helical Edge States in a Quantum Spin-Hall System, Phys. Rev. Lett. **101**, 246807 (2008).

[31] T. Ojanen, Helical Fermi arcs and surface states in time-reversal invariant Weyl semimetals, Phys. Rev. B **87**, 245112 (2013).

[32] Y. Hatsugai, Chern Number and Edge States in the Integer Quantum Hall Effect, Phys. Rev. Lett. **71**, 3697 (1993).

[33] D. H. Lee and J. D. Joannopoulos, Simple scheme for surface-band calculations. I, Phys. Rev. B **23**, 4988 (1981).

[34] V. Dwivedi and V. Chua, Of bulk and boundaries: Generalized transfer matrices for tight-binding models, Phys. Rev. B **93**, 134304 (2016).

[35] L. Balents, Spin liquids in frustrated magnets, Nature (London) **464**, 199 (2010).

[36] D. L. Bergman, C. Wu, and L. Balents, Band touching from real-space topology in frustrated hopping models, Phys. Rev. B **78**, 125104 (2008).

[37] A. Mielke, Ferromagnetic ground states for the Hubbard model on line graphs, J. Phys. A **24**, L73 (1991); Ferromagnetism in the Hubbard model on line graphs and further considerations, **24**, 3311 (1991); Exact ground states for the Hubbard model on the Kagome lattice, **25**, 4335 (1992).

[38] J. Schulenburg, A. Honecker, J. Schnack, J. Richter, and H.-J. Schmidt, Macroscopic Magnetization Jumps Due to Independent Magnons in Frustrated Quantum Spin Lattices, Phys. Rev. Lett. **88**, 167207 (2002).

[39] J. Schnack, H.-J. Schmidt, J. Richter, and J. Schulenburg, Independent magnon states on magnetic polytopes, Eur. Phys. J. B **24**, 475 (2001).

[40] C. Zeng and V. Elser, Numerical studies of antiferromagnetism on a Kagomé net, Phys. Rev. B **42**, 8436 (1990).

[41] H. Asakawa and M. Suzuki, Possibility of a sublattice order of the kagomé antiferromagnet, Physica A **205**, 687 (1994).

[42] O. Derzhko, J. Richter, and M. Maksymenko, Strongly correlated flat-band systems: The route from Heisenberg spins to Hubbard electrons, Int. J. Mod. Phys. B **29**, 1530007 (2015).

[43] Z. Gulácsi, A. Kampf, and D. Vollhardt, Route to Ferromagnetism in Organic Polymers, Phys. Rev. Lett. **105**, 266403 (2010).

[44] H. Tasaki, Ferromagnetism in the Hubbard Models with Degenerate Single-Electron Ground States, Phys. Rev. Lett. **69**, 1608 (1992).

[45] A. Mielke and H. Tasaki, Ferromagnetism in the Hubbard model, Commun. Math. Phys. **158**, 341 (1993).

[46] S. Flach, D. Leykam, J. D. Bodyfelt, P. Matthies, and A. S. Desyatnikov, Erratum: Detangling flat bands into Fano lattices, Europhys. Lett. **106**, 19901 (2014).

[47] J. D. Bodyfelt, D. Leykam, C. Danieli, X. Yu, and S. Flach, Flatbands under Correlated Perturbations, Phys. Rev. Lett. **113**, 236403 (2014).

[48] S. D. Huber and E. Altman, Bose condensation in flat bands, Phys. Rev. B **82**, 184502 (2010).

[49] N. Goldman, D. F. Urban, and D. Bercioux, Topological phases for fermionic cold atoms on the Lieb lattice, Phys. Rev. A **83**, 063601 (2011).

[50] F. Baboux, L. Ge, T. Jacqmin, M. Biondi, E. Galopin, A. Lemaitre, L. Le Gratiet, I. Sagnes, S. Schmidt, H. E. Türeci, A. Amo, and J. Bloch, Bosonic Condensation and Disorder-Induced Localization in a Flat Band, Phys. Rev. Lett. **116**, 066402 (2016).

[51] S. Mukherjee, A. Spracklen, D. Choudhury, N. Goldman, P. Öhberg, E. Andersson, and R. R. Thomson, Observation of a Localized Flat-Band State in a Photonic Lieb Lattice, Phys. Rev. Lett. **114**, 245504 (2015).

[52] E. J. Bergholtz, Z. Liu, M. Trescher, R. Moessner, and M. Udagawa, Topology and Interactions in a Frustrated Slab: Tuning from Weyl Semimetals to $\mathscr{C} > 1$ Fractional Chern Insulators, Phys. Rev. Lett. **114**, 016806 (2015).

[53] M. Trescher and E. J. Bergholtz, Flat bands with higher Chern number in pyrochlore slabs, Phys. Rev. B **86**, 241111(R) (2012).

[54] Z. Liu, E. J. Bergholtz, H. Fan, and A. M. Läuchli, Fractional Chern Insulators in Topological Flat Bands with Higher Chern Number, Phys. Rev. Lett. **109**, 186805 (2012).

[55] A. Sterdyniak, C. Repellin, B. A. Bernevig, and N. Regnault, Series of Abelian and non-Abelian states in $C > 1$ fractional Chern insulators, Phys. Rev. B **87**, 205137 (2013).

[56] M. Trescher, B. Sbierski, P. W. Brouwer, and E. J. Bergholtz, Quantum transport in Dirac materials: Signatures of tilted and anisotropic Dirac and Weyl cones, Phys. Rev. B **91**, 115135 (2015).

[57] A. A. Sulayanov, D. Gresch, Z. Wang, Q. Wu, M. Troyer, X. Dai, and B. A. Bernevig, Type-II Weyl semimetals, Nature (London) **527**, 495 (2015).

[58] S.-Y. Xu, N. Alidoust, G. Chang, H. Lu, B. Singh, I. Belopolski, D. Sanchez, X. Zhang, G. Bian, H. Zheng, M.-A. Husanu, Y. Bian, S.-M. Huang, C.-H. Hsu, T.-R. Chang, H.-T. Jeng, A. Bansil, V. N. Strocov, H. Lin, S. Jia, and M. Z. Hasan, Discovery of Lorentz-violating Weyl fermion semimetal state in LaAlGe materials, arXiv:1603.07318v3.

[59] K. Deng, G. Wan, P. Deng, K. Zhang, S. Ding, E. Wang, M. Yan, H. Huang, H. Zhang, Z. Xu, J. Denlinger, A. Fedorov, H. Yang, W. Duan, H. Yao, Y. Wu, S. Fan, H. Zhang, X. Chen, and S. Zhou, Experimental observation of topological Fermi arcs in type-II Weyl semimetal MoTe$_2$, Nat. Phys. **12**, 1105 (2016).

[60] L. Huang, T. M. McCormick, M. Ochi, Z. Zhao, M.-T. Suzuki, R. Arita, Y. Wu, D. Mou, H. Cao, J. Yan, N. Trivedi, and A. Kaminski, Spectroscopic evidence for a type II Weyl semimetallic state in MoTe$_2$, Nat. Mater. **15**, 1155 (2016).

[61] A. Liang, J. Huang, S. Nie, Y. Ding, Q. Gao, C. Hu, S. He, Y. Zhang, C. Wang, B. Shen, J. Liu, P. Ai, L. Yu, X. Sun, W. Zhao, S. Lv, D. Liu, C. Li, Y. Zhang, Y. Hu, Y. Xu, L. Zhao, G. Liu, Z. Mao, X. Jia, F. Zhang, S. Zhang, F. Yang, Z. Wang, Q. Peng, H. Weng, X. Dai, Z. Fang, Z. Xu, C. Chen, and X. J. Zhou, Electronic evidence for type II Weyl semimetal state in MoTe$_2$, arXiv:1604.01706v1.

[62] N. Xu, Z. J. Wang, A. P. Weber, A. Magrez, P. Bugnon, H. Berger, C. E. Matt, J. Z. Ma, B. B. Fu, B. Q. Lv, N. C. Plumb, M. Radovic, E. Pomjakushina, K. Conder, T. Qian, J. H. Dil, J. Mesot, H. Ding, and M. Shi, Discovery of Weyl semimetal state violating Lorentz invariance in MoTe$_2$, arXiv:1604.02116v1.

[63] N. Xu, Z. J. Wang, A. P. Weber, A. Magrez, P. Bugnon, H. Berger, C. E. Matt, J. Z. Ma, B. B. Fu, B. Q. Lv, N. C. Plumb, M. Radovic, E. Pomjakushina, K. Conder, T. Qian, J. H. Dil, J. Mesot, H. Ding, and M. Shi, Observation of Fermi arc and its connection with bulk states in the candidate type-II Weyl semimetal WTe$_2$, Phys. Rev. B **94**, 241119(R) (2016).

[64] Y. Wu, D. Mou, N. H. Jo, K. Sun, L. Huang, S. L. Bud'ko, P. C. Canfield, and A. Kaminski, Observation of Fermi arcs in the type-II Weyl semimetal candidate WTe$_2$, Phys. Rev. B **94**, 121113(R) (2016).

[65] I. Belopolski, S.-Y. Xu, Y. Ishida, X. Pan, P. Yu, D. S. Sanchez, H. Zheng, M. Neupane, N. Alidoust, G. Chang, T.-R. Chang, Y. Wu, G. Bian, S.-M. Huang, C.-C. Lee, D. Mou, L. Huang, Y. Song, B. Wang, G. Wang, Y.-W. Yeh, N. Yao, J. E. Rault, P. Le Fe‘vre, F. Bertran, H.-T. Jeng, T. Kondo, A. Kaminski, H. Lin, Z. Liu, F. Song, S. Shin, and M. Z. Hasan, Fermi arc electronic structure and Chern numbers in the type-II Weyl semimetal candidate Mo$_x$W$_{1-x}$Te$_2$, Phys. Rev. B **94**, 085127 (2016).

[66] F. Y. Bruno, A. Tamai, Q. S. Wu, I. Cucchi, C. Barreteau, A. de la Torre, S. McKeown Walker, S. Riccò, Z. Wang, T. K. Kim, M. Hoesch, M. Shi, N. C. Plumb, E. Giannini, A. A. Soluyanov, and F. Baumberger, Observation of large topologically trivial Fermi arcs in the candidate type-II Weyl semimetal WTe$_2$, Phys. Rev. B **94**, 121112(R) (2016).

[67] N. Xu, G. Autes, C. E. Matt, B. Q. Lv, M. Y. Yao, F. Bisti, V. N. Strocov, D. Gawryluk, E. Pomjakushina, K. Conder, N. C. Plumb, M. Radovic, T. Qian, O. V. Yazyev, J. Mesot, H. Ding, and M. Shi, Distinct Evolutions of Weyl Fermion Quasiparticles and Fermi Arcs with Bulk band Topology in Weyl Semimetals, Phys. Rev. Lett. **118**, 106406 (2017).

[68] T. C. Fujita, Y. Kozuka, M. Uchida, A. Tsukazaki, T. Arima, and M. Kawasaki, Odd-parity magnetoresistance in pyrochlore iridate thin films with broken time-reversal symmetry, Sci. Rep. **5**, 9711 (2015).

[69] J. C. Gallagher, B. D. Esser, R. Morrow, S. R. Dunsiger, R. E. A. Williams, P. M. Woodward, D. W. McComb, and F. Y. Yang,

Epitaxial growth of iridate pyrochlore $Nd_2Ir_2O_7$ films, Sci. Rep. **6**, 22282 (2016).

[70] P. Goswami, B. Roy, and S. D. Sarma, Competing orders and topology in the global phase diagram of pyrochlore iridates, Phys. Rev. B **95**, 085120 (2017).

[71] C. H. Redder and G. S. Uhrig, Topologically nontrivial Hofstadter bands on the kagome lattice, Phys. Rev. A **93**, 033654 (2016).

[72] G.-B. Jo, J. Guzman, C. K. Thomas, P. Hosur, A. Vishwanath, and D. M. Stamper-Kurn, Ultracold Atoms in a Tunable Optical Kagome Lattice, Phys. Rev. Lett. **108**, 045305 (2012).

[73] H. Zhang, X. Chen, Z. Ma, and Y. Zhou, Kagome lattices for ultracold atoms induced by additional lightfields, J. Phys. B **49**, 115301 (2016).

[74] Y. Yamaji and M. Imada, Metallic Interface Emerging at Magnetic Domain Wall of Antiferromagnetic Insulator: Fate of Extinct Weyl Electrons, Phys. Rev. X **4**, 021035 (2014).

[75] Y. Onose, Y. Taguchi, T. Ito, and Y. Tokura, Specific-heat study of the spin-structural change in pyrochlore $Nd_2Mo_2O_7$, Phys. Rev. B **70**, 060401 (2004).

[76] S. T. Bramwell, M. J. Harris, B. C. den Hertog, M. J. P. Gingras, J. S. Gardner, D. F. McMorrow, A. R. Wildes, A. L. Cornelius, J. D. M. Champion, R. G. Melko, and T. Fennell, Spin Correlations in $Ho_2Ti_2O_7$: A Dipolar Spin Ice System, Phys. Rev. Lett. **87**, 047205 (2001).

[77] T. Arima, Time-reversal symmetry breaking and consequent physical responses induced by all-in-all-out type magnetic order on the pyrochlore lattice, J. Phys. Soc. Jpn. **82**, 013705 (2013).

[78] Z. Wang, A. Alexandradinata, R. J. Cava, and B. A. Bernevig, Hourglass fermions, Nature (London) **532**, 189 (2016).

[79] W. Witczak-Krempa, A. Go, and Y. B. Kim, Pyrochlore electrons under pressure, heat, and field: Shedding light on the iridates, Phys. Rev. B **87**, 155101 (2013).

[80] W. Yang, Y. Xie, W. Zhu, K. Park, A. Chen, Y. Losovyj, Z. Li, H. Liu, M. Starr, J. A. Acosta, C. Tao, N. Li, Q. Jia, J. J. Heremans, and S. Zhang, Epitaxial thin films of pyrochlore iridate $Bi_{2+x}Ir_{2-y}O_{7-\delta}$: structure, defects and transport properties, arXiv:1608.08608.

[81] D. Yanagishima and Y. Maeno, Metal-nonmetal changeover in pyrochlore iridates, J. Phys. Soc. Jpn. **70**, 2880 (2001).

[82] K. Matsuhira, M. Wakeshima, Y. Hinatsu, and S. Takagi, Metal-insulator transitions in pyrochlore oxides $Ln_2Ir_2O_7$, J. Phys. Soc. Jpn. **80**, 094701 (2011).

[83] K. Tomiyasu, K. Matsuhira, K. Iwasa, M. Watahiki, S. Takagi, M. Wakeshima, Y. Hinatsu, M. Yokoyama, K. Ohoyama, and K. Yamada, Emergence of magnetic long-range order in frustrated pyrochlore $Nd_2Ir_2O_7$ with metal-insulator transition, J. Phys. Soc. Jpn. **81**, 034709 (2012).

[84] K. Ueda, J. Fujioka, Y. Takahashi, T. Suzuki, S. Ishiwata, Y. Taguchi, and Y. Tokura, Variation of Charge Dynamics in the Course of Metal-Insulator Transition for Pyrochlore-Type $Nd_2Ir_2O_7$, Phys. Rev. Lett. **109**, 136402 (2012).

[85] J. J. Ishikawa, E. C. T. O'Farrell, and S. Nakatsuji, Continuous transition between antiferromagnetic insulator and paramagnetic metal in the pyrochlore iridate $Eu_2Ir_2O_7$, Phys. Rev. B **85**, 245109 (2012).

[86] K. Matsuhira, M. Tokunaga, M. Wakeshima, Y. Hinatsu, and S. Takagi, Giant magnetoresistance effect in the metal-insulator transition of pyrochlore oxide $Nd_2Ir_2O_7$, J. Phys. Soc. Jpn. **82**, 023706 (2013).